2014

Statistical modeling of interfractional tissue deformation and its application in radiation therapy planning

Douglas J. Vile
Virginia Commonwealth University

Statistical modeling of interfractional tissue deformation and its application in radiation therapy planning

A dissertation submitted in partial fulfillment of the requirements for the degree of Doctor of Philosophy at Virginia Commonwealth University.

by
Douglas J. Vile
Bachelor of Science,
Salisbury University, May 2008

Director: Jeffrey F. Williamson, Ph.D.
Professor, Medical Physics
Department of Radiation Oncology

Virginia Commonwealth University
Richmond, Virginia
May 2015

Acknowledgements

I would like to thank my advisor, Dr. Jeffrey Williamson, for his guidance throughout the course of this research. From him, I learned to be a skeptic, to question authority, and to become a true scientist. Without his guidance, especially early on in my graduate career, this dissertation would not be possible.

I would also like to thank the members of my committee; Drs. Jeffrey Siebers, Martin Murphy, and Gary Christensen. I am also grateful to the NKI for providing the patient database on which the work in this thesis is based, to Dr. Elisabeth Weiss for contouring all of the structures, and to Dr. Chet Ford for many of the DVFs used in this work. I would like to thank the NIH for their financial support (P01CA116602). I am thankful for everybody at VCU who provided me guidance and support over the years, especially Ford Sleeman, Nitai Mukhopadhyay, Geoffrey Hugo, Mirek Fatyga, Joshua Evans, Andrew Sampson, Dandan Zheng, and Jun Lu.

Finally, I would like to thank my family. Thank you to my parents for their unending love and support. They always believed in me, even when I did not (nor gave them reason to). Thank you to my brother, Brad, who has never hesitated to offer me a laugh, encouragement, or a couch to crash on. Lastly, I would like to thank my wife, to whom this thesis is dedicated. She has been my one-person support group throughout my time here at VCU. Six years later, she is still the best part of my life.

For Julie, my rock. I could not have done this without him.

Table of Contents

List of Tables

List of Figures

List of Abbreviations

AP	Anterior/posterior
ART	Adaptive radiation therapy
bNED	Biochemical non-evidence of disease
CBCT	Cone-beam computed tomography
CDF	Cumulative distribution function
COM	Center of mass
COP	Coverage optimized planning
CRT	Conformal radiation therapy
CT	Computed tomography
CTV	Clinical target volume
DIR	Deformable image registration
DRR	Digitally reconstructed radiograph
DVF	Displacement vector field
DVH	Dose volume histogram
EBRT	External beam radiation therapy
gEUD	Generalized equivalent uniform dose
GTV	Gross tumor volume
ICRU	International Commission of Radiation Units and Measurement
IGART	Image guided adaptive radiation therapy
IGRT	Image guided radiation therapy
IMRT	Intensity modulated radiation therapy
KDE	Kernel density estimation
LR	Left/right
NCCN	National Comprehensive Cancer Network
NKI	Netherlands Cancer Institute
OAR	Organ at risk

PCA	Principal component analysis
PDF	Probability density function
PRV	Planning organ at risk volume
PSA	Prostate specific antigen
PTP	Probabilistic treatment planning
PTV	Planning target volume
QA	Quality assurance
RCF	Research computing framework
SI	Superior/inferior
SICLE	Small deformation, inverse consistent, linear elastic
TPS	Treatment planning system
VCT	Virtual clinical trial
VCU	Virginia Commonwealth University

Abstract

STATISTICAL MODELING OF INTERFRACTIONAL TISSUE DEFORMATION AND ITS APPLICATION IN RADIATION THERAPY PLANNING

By Douglas J. Vile, B.S.

A dissertation submitted in partial fulfillment of the requirements for the degree of Doctor of Philosophy at Virginia Commonwealth University.

Virginia Commonwealth University, 2015

Major Director: Jeffrey F. Williamson, Ph.D.
Professor, Medical Physics
Department of Radiation Oncology

In radiation therapy, interfraction organ motion introduces a level of geometric uncertainty into the planning process. Plans, which are typically based upon a single instance of anatomy, must be robust against daily anatomical variations. For this problem, a model of the magnitude, direction, and likelihood of deformation is useful. In this thesis, principal component analysis (PCA) is used to statistically model the 3D organ motion for 19 prostate cancer patients, each with 8-13 fractional computed tomography (CT) images. Deformable image registration and the resultant displacement vector fields (DVFs) are used to quantify the interfraction systematic and random motion. By applying the PCA technique to the random DVFs, principal modes of random tissue deformation were determined for each patient, and a method for sampling synthetic random DVFs was developed.

The PCA model was then extended to describe the principal modes of systematic and random organ motion for the population of patients. A leave-one-out study tested both the systematic and random motion model's ability to represent PCA training set DVFs. The random and systematic DVF PCA models allowed the reconstruction of these data with absolute mean errors between 0.5-0.9 mm and 1-2 mm, respectively. To the best of the author's knowledge, this study is the first successful effort to build a fully 3D statistical PCA model of systematic tissue deformation in a population of patients.

By sampling synthetic systematic and random errors, organ occupancy maps were created for bony and prostate-centroid patient setup processes. By thresholding these maps, PCA-based planning target volume (PTV) was created and tested against conventional margin recipes (van Herk for bony alignment and 5 mm fixed [3 mm posterior] margin for centroid alignment) in a virtual clinical trial for low-risk prostate cancer. Deformably accumulated delivered dose served as a surrogate for clinical outcome. For the bony landmark setup subtrial, the PCA PTV significantly ($p<0.05$) reduced D_{30}, D_{20}, and D_5 to bladder and D_{50} to rectum, while increasing rectal D_{20} and D_5. For the centroid-aligned setup, the PCA PTV significantly reduced all bladder DVH metrics and trended to lower rectal toxicity metrics. All PTVs covered the prostate with the prescription dose.

1. Introduction

The goal of fractionated definitive radiotherapy is to deliver a sufficient dose to kill all cancerous tumor cells while minimizing the risk of toxicity to the surrounding healthy tissue. Both cancerous and healthy tissues exhibit day-to-day variations in organ position, shape, and volume. These changes in 3D anatomy (referred to collectively as organ motion in this thesis) can be classified as either intra- or interfraction motions. Intrafraction motion is the change in anatomy over the course of a single daily treatment. Interfraction motion is the change in anatomy from day to day. The latter issue will be the focus of this thesis.

Anatomical motion and deformation introduces geometric uncertainty into the radiation therapy planning process. Conventional planning involves acquiring a 3D computed tomography (CT) image of the patient to plan a radiation treatment. This CT image only captures a "snapshot" of the patient, or how the anatomy looks at a particular moment in time. Plans based on these snapshots have the potential to be suboptimal for treatment as any organ motion that occurs subsequent to treatment planning can result in target miss and/or healthy tissue overdose.

Ideally, online planning would be used for all radiation therapy treatments. Online planning involves imaging the patient in the treatment position prior to each fraction. While the patient is waiting, the relevant anatomy would be contoured and a plan of the day developed and delivered based on this current anatomical instance. Assuming the patient remained stationary during this process, online adaptive radiation

therapy would eliminate any errors introduced by interfraction motion. Although intrafraction motion would not be accounted for, online adaptive radiation therapy would be extremely useful in sites where interfraction motion dominates organ motion, such as the prostate and cervix.[1-3] This could also be helpful in sites such as head and neck, where there exists a temporal dependence of interfraction motion due to patient weight loss and tumor regression.[4-7] In prostate radiation therapy, Ghilezan[8] showed that idealized daily online planning provided, on average, a 13% increase in the therapeutic ratio. Therapeutic ratio is the ratio of tumor control to radiation-induced normal tissue toxicity. Ghilezan defined therapeutic ratio as the maximum generalized equivalent uniform dose (gEUD) to the prostate without exceeding specified organ at risk (OAR) toxicity quantified in terms of gEUD. For prostate treatment, the dose-limiting organ was found to be the rectum. Additionally, the individual benefit in therapeutic ratio varied widely (SD=9.7%) from patient to patient. Still, approximately one-third of the patients in the Ghilezan study benefited from online adaptive planning, with therapeutic ratio increases of at least 15%.[8]

However, such idealized online planning has a number of drawbacks, including the amount of time needed to create the daily plan. The patient must be imaged, the target and avoidance structures delineated, and an optimized plan created, all with the patient remaining in the treatment position. This lengthy process can lead to unacceptable patient discomfort and may seriously hinder patient throughput in the clinic. For these reasons, online planning is currently impractical for daily patient care. While improvements are being made to hasten the online planning process,[9-11] alternative methods for accounting for anatomical uncertainty must be utilized.

Recent advances in in-room imaging systems, such as cone beam CT (CBCT) and CT-on-rails, have improved target localization in radiation therapy.[12,13] Imaging immediately before and during treatment is becoming routine and reduces patient setup errors. These images are used to rigidly align the patient's treatment anatomy with his or her planning anatomy by means of couch shifts and can be based on bony anatomy, soft tissue landmarks, or implanted markers within the tumor. While such deterministic corrections can improve the therapeutic ratio, they cannot account for all sources of anatomical uncertainty.[14] One common deterministic correction currently practiced is online setup to radio opaque fiducial markers implanted directly into the prostate. However, not all impacts of organ motion and tissue deformation can be fully accounted for using translational and rotational alignment, e.g., deformations of the CTV and changes in shape and relative position of OARs. These residual uncertainties must be accounted for by other means. Generally, this is accomplished by creating an initial treatment plan that is designed to be robust against daily variations in the patient's anatomy.

To create such a plan, some form of probabilistic treatment planning (PTP) is usually used. PTP is the process of maximizing the likelihood that treatment objectives are met in situations of anatomical uncertainty. A simple and nearly universally used PTP approach is the use of a margin. The International Commission of Radiation Units and Measurement (ICRU) Report 50 has defined several concepts relevant to margins,[15] the first of which is gross tumor volume (GTV). The GTV is the extent of malignancy that can be determined through physical examination, imaging, or a combination of the two. The CTV is the GTV plus any presumed microscopic extension

of the disease. In addition to the GTV, the treatment plan must include the CTV, as the CTV is presumed to contain malignant cells. In practice, this is determined by measuring the GTV and expanding the volume with a margin or to adjacent anatomical boundaries that delimit the potential spread of subclinical disease. The final volume is the ICRU 50 defined planning target volume (PTV). The PTV is a geometrical concept that is used to account for possible geometric uncertainties, including patient setup errors, beam setup errors, and organ movement and deformation. The PTV is generally taken as an expansion of the CTV using some margin that is determined to ensure adequate coverage of the CTV, in the event of anatomical motion.

The use of a margin to create the PTV represents a tradeoff between target coverage and normal tissue toxicity. The expansion must be large enough so the PTV encompasses the expected range of daily anatomic presentations. A larger margin will ensure the plan is more robust against tumor miss, but it may subject larger volumes of the OARs to unnecessarily large doses, thereby reducing the therapeutic ratio. Different strategies have been proposed to estimate the optimal margin, using knowledge of the underlying organ motion to create a PTV that encompasses a large percentage of possible daily anatomies. These margin calculations are statistical in nature, meant to ensure a high probability of target coverage. For this reason, this thesis considers margin-based planning to be the simplest of PTP techniques. Several of these strategies will be discussed later in this chapter.

More advanced PTP methods directly incorporate probabilistic criteria into the planning process. Unlike traditional objective functions, which optimize on dose criteria for both the PTV and OARs, PTP optimizes on the likelihood of these criteria being met

in the presence of organ motion. All PTP methods require a statistical organ motion model. A PTP method is only as good as its underlying assumption of the magnitude, direction, and likelihood of different daily anatomical configurations. The goal of this thesis is to develop a 3D statistical model that includes both OARs and CTVs.

Modeling—specifically, statistical modeling of the patient's anatomical changes—is the most effective strategy for accounting for those errors for which deterministic correction is not technically feasible or cost effective. A model of anatomical motion, as the term is used in this thesis, is a statistical measure of the probability of a given anatomical instance over the course of radiation therapy. Here, an anatomical instance is represented by a voxel-by-voxel mapping between the planning anatomy and the daily treatment anatomy. This mapping is characterized by a displacement vector field (DVF), a general measure of organ motion. A model gives the probability of all possible deformed states, as described by DVFs and can provide valuable information to the planning process when the treatment-day anatomy cannot be easily known. This information can be directly incorporated into the planning process.

Statistical motion models can be used for any treatment site where there is organ motion. Hereafter, "organ motion" will refer to any displacement or deformation between the patient's treatment day anatomy and his or her planning anatomy. The work presented in this thesis is mainly focused on the development of a new model and its potential clinical applications. The focus is on the anatomy critical to the treatment of low-risk prostate cancer, specifically, the prostate, bladder, and the rectum. This three-organ system in the male pelvis was chosen for several reasons. These organs move relative to bony anatomy, their movement is correlated with bladder and rectal filling,[16,17]

and the intrafraction motion is smaller in relation to the interfraction motion. Britton *et al.* reported the mean interfractional motion of an implanted fiducial to be 1.76, 3.14, and 3.78 mm in the left-right, superior-inferior, and anterior-posterior directions, respectively. This compares to the measured intrafraction motion of 0.45, 1.08, and 1.45 mm.[2] Su *et al.* separated the inter- and intrafractional motion into its systematic and random components. Their results are shown in Table 1.[1]

Table 1: Comparison of the inter- and intrafraction motion of the prostate as measured by Su *et al*.[1]

		LR	SI	AP
Interfraction	Systematic Error (mm)	2.3	3.4	4.7
	Random Error (mm)	3.7	2.7	3.5
Intrafraction	Systematic Error (mm)	0.3	0.5	0.6
	Random Error (mm)	0.7	1.4	1.9

Abbreviations: LR=left/right. SI=superior/inferior. AP=anterior/posterior.

Additionally, the treatment target (the whole prostate) has a stable (±10%) volume over the treatment course.[17] This reduces the possibility of any time trend in the anatomy over the course of treatment, removing an unnecessary extra layer of complexity to any modeling attempt.

This work is intended to show the clinical benefit of incorporating statistical motion modeling of the prostate, bladder, and rectum into the treatment planning process. This could be extended to high-risk prostate cancer patients by including seminal vesicles and pelvic lymph nodes in the model. Results from this work could also directly benefit intermediate and high-risk prostate cancer patients, as a prostate-

only boost is a very common part of their treatment. This work could also be adapted for use in focal radiation therapy. The model could be used to identify the daily locations of subregions of the prostate containing a higher concentration of malignant cells. This region could then be boosted to a higher dose, with the model being used to ensure coverage. This model could also be extended to different treatment sites, such as head and neck, and pancreas.

1.1. External beam radiation therapy of prostate cancer

Currently, there are a number of treatment options for patients diagnosed with prostate cancer. Some of the most common include watchful waiting, radical prostatectomy, low dose rate brachytherapy (permanent seed implant), and external beam radiation therapy (EBRT), or some combination thereof. The choice and effectiveness of these options are highly dependent on the tumor's T-stage and biological aggressiveness (conventionally measured by Gleason score and pretreatment prostate-specific antigen [PSA] level). Broadly, the National Comprehensive Cancer Network (NCCN) classifies prostate cancer into low, intermediate, and high risk.[18] In both low and intermediate risk prostate cancer, the disease must be clinically staged as prostate-confined. A tumor falls into the high-risk category if it invades adjacent structures such as the seminal vesicles and pelvic lymph nodes. However, very high Gleason score (>7) or pretreatment PSA with clinical evidence of spread outside the prostate can also qualify the patient for high-risk status.

As this thesis is focused on low-risk prostate cancer, discussion will be limited to the current interventions and their outcomes in this context. Currently, radical prostatectomy, brachytherapy, and EBRT all have very favorable control rates. Ten-

year follow-ups after 3D conformal radiation therapy (CRT) EBRT showed a 93% rate of freedom from biochemical failure (bNED).[19] Memorial Sloan Kettering has shown that by using intensity-modulated radiation therapy (IMRT) to deliver a highly conformal escalated dose (86.4 Gy), seven-year bNED rates for low-risk prostate cancer were as high as 99%.[20] A separate study showed comparable results between 3D CRT EBRT and radical prostatectomy.[21] Seven- and 10-year studies for brachytherapy have shown a 95% and 94.1% biochemical relapse-free survival, respectively.[22,23]

While each modality exhibits excellent control rates, each option has drawbacks and associated side effects. Not all patients are candidates for radical prostatectomy or brachytherapy, as both procedures are invasive. Both procedures are also dependent on the skill of the surgeon. EBRT is noninvasive and less dependent on physician skill. All procedures are associated with varying degrees of short- and long-term difficulties in urinary and sexual function.[24-26]

For EBRT, one study of 151 patients treated to 78 Gy reported grade 2 or higher bladder toxicities of 10% and grade 2 or higher rectal toxicities of 26%.[27] Arguably, EBRT has the largest potential to improve toxicity rates by limiting the dose to surrounding OARs. In a literature review, Staffurth reported that by using the more conformal approach of IMRT instead of 3D CRT, grade ≥2 gastrointestinal toxicities were reduced to from 20% in 3D CRT to 6% using IMRT.[28] In the same review, it was noted that there were no significant differences in genitourinary toxicity between 3D CRT (median incidence of 18%) and IMRT (median incidence of 21%). This suggests that there is still a need for more optimal treatment that can help spare the bladder.

Combining highly conformal dose delivery with better knowledge of the target location has the potential to further reduce toxicity. Anatomical uncertainty requires the plan to target a larger volume, increasing the bladder and rectum volumes that receive the full prescription dose. One hypothesis of this thesis is that a completely 3D statistical model of this three-organ system to accommodate targeting uncertainty due to residual organ motion not controlled by a daily deterministic IGRT correction will reduce OAR doses needed without comprising target coverage.

1.2. Previous work on statistical management of anatomical uncertainty

In this thesis, targeting error is defined as the linear difference between corresponding anatomical locations in the patient's planning anatomy at the time of simulation and the patient's anatomy at the time of treatment. This error arises from various sources, including setup errors, organ displacement, and organ/soft tissue deformation. Setup errors are any errors introduced by suboptimal patient positioning in the treatment room. Patient positioning can be done in several ways. Traditionally, patients have been positioned on the treatment table by aligning skin tattoos with in-room lasers in conjunction with initial and weekly port films or x-rays. With the widespread use of in-room imaging, further target alignment has become quite common. To align on bony landmarks, x-ray projections or CBCT are used to image the patient, and the bones are then used to reposition the patient to match the planning image. This is fairly straightforward as the skeletal structure of the patient does not greatly change from day to day. In prostate cancer, is also common to align on radio opaque fiducial markers implanted directly into the prostate. In-room x-rays are then

taken to align the patient based on these intraprostatic markers. This technique not only attempts to partly correct for setup errors, but also organ displacements.

Translational corrections are made to account for both setup errors (errors due to setup alone) and organ motion. Both tattoo and bony alignment assume that the patient's soft tissue is fixed in relation to the skin and bones. This is not the case, as differences have been found between tattoo (with weekly portal image verification) and bony alignment setups.[29] There have also been reported differences between bony and marker based setup.[30-32] Fiducial marker setup has the advantage of aligning to a point within the target (prostate) that is to be treated, correcting for more organ motion than a bony-aligned setup. Marker-based setup has some associated uncertainty: Changes in inter-marker distances on the order of 1.5 mm due to prostate deformation and seed migration have been reported.[33,34] Studies have shown differences in the prostate surface of over 1 mm even after post marker alignment.[35,36] A fiducial alignment also does not account for motion in the volumes surrounding the prostate,[37] such as the OARs. Nearly all online setup techniques use a translation-only strategy, ignoring rotations and deformation. None of these methods can fully account for daily organ motion. Therefore, strategies to account for the residual error must be incorporated into the planning.

In prostate cancer, the most common approach for managing residual anatomical uncertainty is the use of a PTV margin. Since the introduction of PTVs, different formulas for their associated margins have been proposed. For prostate treatment, the two most well-known formulas are those constructed by Stroom[38] and van Herk.[39] Both divide the targeting error they are accounting for into systematic and random

components. Systematic error is the displacement relating the patient's planning anatomy to the patient's mean anatomy. Random error is the daily residual displacement around the systematic error. Each type of error has a different effect on the delivered dose distribution. Random errors are less worrisome when compared to systematic, as they create a blurring of the dose distribution and tend to "wash out" over the course of many fractions.[40] Systematic errors are more serious, as they manifest as shifts in the cumulative dose distribution.[41] Both Stroom and van Herk formulas are based on statistical models and are designed to meet certain CTV coverage criteria over the course of treatment.

Both formulas are designed to use the statistical motion characteristics of a population of similar patients. The population statistics used in their organ motion modeling were the standard deviation of the systematic error distribution, Σ, and that of the random error distribution, σ. In order to calculate these population statistics, Stroom and van Herk assumed any targeting error can be described by one systematic error and one random error. Also assumed is that the prostate is a rigid body that can only translate, ignoring deformation.

Both formulas were built to probabilistically ensure dose coverage. Stroom designed his margin to ensure at least 95% of the prescribed dose is delivered to an average of 99% of the CTV for a prostate, cervix, and lung clinical plan. To accomplish this, target coverage probability is computed using the inputs Σ and σ. This calculation is then coupled with an actual 3D CRT dose distribution (for prostate, the 3 field box technique is used) to meet the stated criteria. This method includes translational and rotational errors. The van Herk method was aimed at providing a minimum of 95% of

the prescribed dose to the entire CTV for 90% of patients. To account for systematic errors, this method uses purely coverage-based criteria, ignoring the dose distribution. The dose distribution is taken into account for random errors, where a conformal dose distribution with a 3.2 mm beam penumbra is assumed in the commonly used formulation. This method includes translational errors only.

Both formulas take into account setup error as well as rigid tumor motion. For example, in the prostate, a bony-aligned setup would include the systematic and random errors of the alignment as well as the systematic and random errors of the prostate's movement in relation to the bony anatomy. As alignment to intraprostatic fiducial markers becomes more popular, these formulas lose value. The systematic and random errors become zero as the markers are assumed to move rigidly with the rest of the prostate. In these instances, there is still a need for a margin to account for the deformations and rotations of the prostate.

Alternative methods have been reported that account for the residual anatomical uncertainty after deterministic corrections. Such methods incorporate the use of image-guided adaptive radiation therapy (IGART). IGART uses data from patient images to adapt the original treatment plan based on anatomical characteristics of the specific individual. A well-documented clinical variation of IGART is Beaumont-style adaptive radiation therapy (ART), hereafter referred to as "Beaumont ART." This method, developed by Yan *et al.*, estimates the patient-specific systematic error and random error distribution, σ, based on a limited number of fractions, k, usually taken to be 5 days.[42,43] In their method, CT simulations are taken during the first k days of treatment, with the CTV contoured on all images. The images are then aligned on bony anatomy,

and a convex hull is created from the union of these contours. This structure is referred to as the $\mathrm{PTV}_o(k)$, and compensates for internal target motion. During the same time, in-room projections are taken directly prior to treatment and compared to digitally reconstructed radiographs (DRRs) to find the rigid shifts of bony anatomy. From these projections, systematic and random error distributions are determined as the average and standard deviation of the shifts, respectively, using a Kalman prediction method to estimate the true values from the measurements. The setup position is then modified to account for the systematic error, while a margin is added to $\mathrm{PTV}_o(k)$ to compensate for the random errors. The $\mathrm{PTV}_o(k)$ plus the margin is referred to as the clinical PTV, or cl-PTV. The patient is then replanned and treated based on the derived cl-PTV. Beaumont ART has been shown to give a maximum dose reduction of 2% or less to the CTV for at least 80% of patients in IMRT cases.[42] This means that dose coverage to the CTV is not compromised by planning using the cl-PTV derived from a small subset of measurements taken in the first week of treatment.

Beaumont ART uses the relatively simple idea of a convex hull in order to model the possible prostate deformations specific to an individual patient. This method takes into account some of the possible deformations of the prostate, but fails to account for the surrounding organs at risk, such as the bladder and rectum. In addition, Beaumont ART gives no guidance on how to plan and treat the patient during the data accumulation period. It also relies on estimating a PTV from a limited dataset. Due to the small statistical sample size (5 days of images), additional estimation of the residual anatomical uncertainty is needed. Beaumont ART provides little information on how the prostate deforms and no information on the deformations of any OARs. A completely

3D statistical model of the male pelvis would provide such information. Incorporating knowledge of OAR motion, target coverage, and critical structure avoidance could improve the therapeutic ratio.

1.3. Deformable image registration (DIR)

The most complete, currently available characterization of organ motion between two anatomic states of a given patient is deformable image registration (DIR). DIR computes the transformation that maps points in a source image to their corresponding voxels in the target image. The resultant DVF quantifies the net displacement of a tissue subvolume during the time interval between acquisitions of the two images. As multiple images are acquired over the course of treatment, each new image can be registered to a common image. This produces multiple measurements of the patient's interfraction motion. With enough samples, these DVFs can be used to look for possible patterns in tissue motion over the entire 3D volume contained in the images.

Fundamentally, DIR is an optimization problem. The underlying objective function that drives the registration ultimately determines the resultant transformation. DIR generally tries to determine the transformation that minimizes the intensity differences between the two input images, but often includes other criteria to ensure a realistic correspondence between the two images. Such criteria include regularization, which can ensure a smooth and realistic image. In the end, any useful data derived from deformable image registration are only as reliable as the DIR algorithm's ability to characterize the underlying anatomical motion.

1.4. Principal components analysis (PCA)

Extracting useful information from a collection of DVFs is a difficult task. Each DVF is a data structure that can store 3D displacements of millions of voxels. The data associated with these voxels are often highly correlated, however. The trajectory of a given voxel over the course of treatment is likely to be similar to its neighboring voxels. This correlation can be exploited using principal component analysis (PCA) in an attempt to reduce the high dimensionality of the problem. PCA is the eigendecomposition of the covariance matrix of the data. Each element of the covariance matrix represents the covariance between two voxels, a measure of how these variables change together. PCA is the eigendecomposition of this matrix, the mathematical equivalent of a coordinate system transformation. The output is a basis set of orthogonal eigenmodes. The first eigenmode, or most principal component, is the basis vector on which one can project the greatest amount of variance in the data. The second-most principal component is the orthogonal vector that can account for the most amount of residual variance in the data, and so on. Each eigenmode has a corresponding eigenvalue. The eigenvalues are measures of how much variance in the data is represented by its associated eigenmode. Eigenmodes that represent little variance (generally all those totaling <10%) in the original data can then be discarded, further reducing the dimensionality. These eigenmodes are assumed to represent small and unlikely modes of motion or possible noise in the data.

The resultant eigenmodes are a basis set for the PCA input data, meaning the input data can be represented as a linear combination of these eigenmodes multiplied by some scaling coefficient. As the eigenmodes are orthogonal, the distributions of their

associated scaling coefficients are linearly independent from one another. For the input data, the distribution of these coefficients is related to a normal distribution with a standard deviation equal to the eigenvalue associated with the eigenmode. In the context of anatomical motion, the principal components are DVF-like structures that represent the most likely independent patterns of motion in our dataset. Assuming the initial dataset adequately represents the patient's underlying physical motion, PCA also has the ability to represent future deformations in the patient that are not included in the initial training set. This process is as simple as finding the corresponding scaling coefficients for each eigenmode. These coefficients are calculated as the dot product of the eigenmode and the original data.

In this work, the potential value in PCA lies with its ability to break down male pelvic motion into the underlying dominant modes of motion. PCA also computes the likelihood of a given deformation as the likelihood of selecting the associated scaling coefficients. These measures of the magnitude, direction, and probability of motion can be directly incorporated into the planning process. Larger margins can be implemented in areas with high likelihood of large target deformation or displacement, and greater efforts can be made to spare areas more likely to be occupied by deformed instances of OARs. This knowledge could be used to optimize outcomes for individual patients and for the patient population as a whole.

Previously, PCA characterizations of organ motion and anatomical changes have been used to analyze and help diagnose diseases ranging from scoliosis to Alzheimer's.[44,45] Less work has been done to explore the motion of the pelvic anatomy in the treatment of prostate cancer. One work of note is the detailed statistical analysis

done by Sohn.[46] In this work, PCA was used to statistically model the surface deformations of the three-organ system of the prostate, bladder, and rectum. For four separate patients, the organ shapes were deformably registered to the average organ system shape, and the principal eigenmodes of deformation were calculated, related to the major geometrical modes of variation. The authors found that a patient's organ shapes could be reconstructed to within 1.3–2.0 mm using four principal modes. Their results are of limited value to IGART applications, as they represent only surfaces of the three organs mentioned. The rest of the anatomy (both inside and outside of the three organs) was not modeled in their study. In addition, their analysis was patient-specific, and they found no correlation between modes between patients. Patient-specific models have been proposed in other sites, most notably lung.[47,48] In such models of the prostate, numerous images are needed over the course of two or three weeks to fully characterize the patient specific motion. Any intervention in treatment could only be done after this initial data collection period.

This data collection problem is addressed by Budiarto *et al*.[49] Although only dealing with the shape of the prostate and seminal vesicles, a PCA technique was outlined to incorporate population data into the analysis. Since systematic organ motion error is unique for each patient's treatment, population data is necessary in order to model the distribution of systematic errors across a group of patients. Using 18 patients, each with four DVFs, to build their training dataset, Budiarto *et al*. were able to reconstruct the deformations of three patients not included in the training set, with the prostate and seminal vesicle boundary displacements accurate to within 1.5 mm using 15 eigenmodes. Budiarto *et al*.'s study was limited to modeling the surfaces of the

prostate and seminal vesicles. Ideally, a description of the anatomy as a whole is desirable. This is especially important in prostate cancer, as the bladder and rectum have greater magnitudes of deformation than the prostate. In the follow-up paper, this population model was used to investigate the dosimetric effect of random errors.[50] For a single prostate case, they calculated the mean and standard deviation of the dose to the prostate and seminal vesicles in the presence of random deformation errors. This work was very limited in clinical usefulness, however. They admittedly ignored any systematic deformation errors and their effect on the dose. Additionally, their analysis used a single beam and incorporated only the single most dominant mode of motion (representing only 34.7% of the whole spectrum energy). Their method for calculating the mean and standard deviation of the dose was quite computationally expensive, possibly limiting its direct use in the plan optimization process.

A population model for the entire 3D pelvic anatomy, and not just one with limited organ shapes, would be of great benefit. The model could be incorporated into the radiation therapy treatment planning process in a number of ways. For example, if the model predicted a large probability of organ motion in a certain direction but very little in another, the model could be used to create anisotropic margins that better spared normal tissue and ensured greater coverage of the prostate. Anatomical motion statistics could also be incorporated into PTP. This process would use the population model of the anatomical uncertainty to create a plan that maximizes the probability of realizing tumor coverage and other treatment goals. The model would be based on population data and would require no extra information of a patient other than his planning CT.

The potential danger of a population model is that it might not benefit every patient. By definition, the goal of a population model in this context is to describe the anatomical motion for most patients; however, patients with abnormal organ motion may have their tumors underdosed while patients with little organ motion may have the normal surrounding tissue unnecessarily overdosed. This may be resolved in an adaptive strategy, using a patient-specific model, to replan the patient treatment as more individual data (e.g., daily CBCT images) are gathered.

1.5. Novel research contributions and acknowledgements

The general goal of this thesis is to develop a process for statistically modeling 3D systematic and random tissue deformation that could, in principle, be applied to any treatment site. The independent contributions of the writer (Douglas J. Vile) are as follows. I, Douglas, have implemented a working tool for modeling both individual and population organ motion, as characterized using DVFs. This included creating a detailed mathematical description of these models and creating a Matlab-based computer code to implement the models. In this process, I determined a solution to the problem of performing organ specific deformable registrations from one patient to another, as well as developing DVF stitching techniques to be used in this work. These inter-patient registrations were used in solving the problem of transporting patient specific statistics to a reference anatomy. I am responsible for all evaluation of the models developed in this thesis.

With the models in place, I proposed and implemented two virtual clinical trials (VCTs) in order to demonstrate clinical utility. This was done in the context of radiation therapy for low-risk prostate cancer. I also worked with Huijun Xu in order to implement

patient-specific statistical modeling within the probabilistic treatment planning framework of coverage optimized planning.

To my knowledge, this thesis presents the most complete statistical modeling of the pelvic anatomy for patients undergoing definitive radiation therapy for prostate cancer. This work includes the statistical modeling of individual patients as well as for a population of patients, and is the first to report a fully 3D representation of systematic and random error distributions of the pelvic organ motion. A novel method for creating treatment planning margins is developed that is based on the population statistical model.

The work in this thesis is the realization of project first proposed by Drs. Jeffrey Williamson, Martin Murphy, and Ramesh Ramakrishnan in a Program Project Grant application last submitted to the NIH (P01CA116602) in 2006. That application introduced the concept of using PCA to model statistical fluctuations of organ motion through PCA modeling of DVFs describing both random and systematic organ motion. Specifically, this work stems from Project 1 (Deformable Image Registration and Reconstruction), Project 3 (Image-guided IMRT and Brachytherapy for Pelvic Tumors), and Core B (Administration, Biostatistics, and Outcomes Modeling) of that research grant.[51-53] The author of this thesis gratefully acknowledges the guidance and intellectual input received from Drs. Murphy, Christensen, and Williamson during the course of this project. In addition, the author would like to thank Dr. Chet ford, who computed many of the DVFs on which this work is based upon. Much gratitude is expressed to the NKI for providing the CT images used in this thesis, to Dr. Jeffrey Seibers for their processing, and to Dr. Elisabeth Weiss for contouring the images. The

work in this thesis could not have been possible without use of research computing framework (RCF) tools developed at VCU and their authors. This work specifically uses the DVF generator, image and contour warping, and biological dose accumulator tools. The author would also like to thank Ford Sleeman and Dr. Mirek Fatyga for their help using these tools. Finally, the author would like to thank Dr. Nitai Mukhopadhyay of the VCU Department of Biostatistics for his guidance on statistical methods utilized in this work.

1.6. Research aims and organization

Chapter 2 outlines the process through which I built a statistical PCA model using a series of collected images for an individual patient. The dataset and methods used in this entire research are described in depth. Efforts to validate the method are presented, verifying that the PCA model accurately describes the underlying patient anatomy. Potential uses and applications of an individual model are also discussed.

Because little patient-specific data is available at the beginning of treatment, there is not enough statistical power to create a patient-specific model. In Chapter 3, I address this issue by describing the construction of a population model for the male pelvic organ motion. The need for a common coordinate system in which to model the anatomy is presented in detail. Any modeling errors were quantified as an assessment of its potential use. The constructed model was used to calculate and compare Σ and σ between two different patient setups. A bony alignment patient setup and a simulated fiducial marker setup was compared. Organ occupancy diagrams were also calculated and compared for the two setups. This chapter is structured to align with a

manuscript that is to be submitted for publication. This manuscript is included in Appendix B.

With the population model in place for both a bony and simulated fiducial-based patient setup, an example of incorporating it into the treatment planning process is outlined in Chapter 4. This straightforward method involved using the occupancy diagrams created in Chapter 3 to calculate an anisotropic margin for use in the planning process. This planning method was directly compared against current planning techniques using the virtual clinical trial (VCT) framework. The VCT framework allowed for the comparison of two planning techniques on the same patient data. Dose volume histogram (DVH) metrics were used for the comparison of physical dose.

In Chapter 5, I discuss the limitations and the potential future uses of the methods described in this thesis. Topics include the potential adaptive planning process by individualizing the patient treatment as well as extensions of the methodology to other sites. This work is supplemented by two appendices. Appendix A outlines the mathematical formalism of the PCA technique. Appendix B includes the manuscript on the construction and validation of the population model.

2. 3D systematic and random targeting error and statistical modeling of patient-specific anatomical deformations

2.1. Introduction

The anatomy of a single prostate cancer patient is never the same from treatment day to treatment day. The bladder and rectum fill and empty, pressing on the surrounding organs, causing shape deformation and displacement. For the displacement, a simple rigid shift of the patient's treatment position can prove to be a beneficial correction strategy.[54,55] However, no rigid shift will be able to account completely for deformation. Ideally, online replanning would be used to create a plan specifically for that day's anatomy. First, the patient would be set up in the treatment position. An onboard 3D image would be acquired, with contouring of all organs used in the planning process. Finally, a treatment plan would be created for this specific anatomical instance. A prospective virtual study has shown a theoretical increase to the therapeutic ratio of 13%.[8] This would account for interfractional organ displacement and deformation, but not intrafractional motion.

For several reasons, online planning is not practical in reality. The biggest hindrance is the time necessary to image, contour, and replan. Each of these steps usually requires its own specialist to complete. The physicist or therapist is responsible for the imaging, the physician for the contouring, the dosimetrist for the planning, and the physician and physicist for quality assurance (QA) checks. This workflow under the time constraint of the patient on the table is not currently feasible. Current techniques, such as those reported by Wu, involve modifying the workflow of online adaptive

planning. In Wu's method, a CBCT image of the patient in the treatment position is acquired and DIR is performed to map this treatment image to the patient's planning image. The resultant transformation is then used to deform the dose distribution from the original plan; the deformed dose becomes the "goal" of a new plan. Re-optimization is performed in order to determine the fluence map that gives the goal dose. Wu reported the time needed for the optimization process to be 2 minutes.[11] While promising, this process is still quite lengthy, and the poor quality of CBCT images could cause the DIR to give a suboptimal registration. Deterministic corrections are much more practical, such as repositioning the patient to align the treatment isocenter. This strategy still leaves some residual deformation of the organs unaccounted for,[9,10] which was investigated in this study. Thus, there is a need to create an initial plan robust against anatomical uncertainties.

Probabilistic treatment planning (PTP) is the process by which one tries to maximize the probability of specific treatment objectives in the face of a patient's unknown daily anatomy to ensure that the treatment objectives are met for a large percentage of the daily anatomical realizations. These treatment objectives vary greatly in complexity. The simplest objective (and the one most commonly used) is an expansion of the CTV by a margin to create the PTV, which ensures that most anatomical deviations from the planning image will still be confined to this volume. More advanced methods, such as coverage optimized planning first presented by Gordon, incorporate the dose coverage probability in the face of organ motion directly into the optimization process.[56]

While both of these methods are built to withstand unknown day-to-day variations in patient anatomy, both require knowledge of the uncertainty associated with the patient's underlying organ motion. For this reason, there is value in a patient-specific model of anatomical deformations. A 3D statistical motion model of the patient allows these probabilistic methods to create a plan robust against realistic organ motion as opposed to the simplistic translational estimates currently used. The uncertainty in the patient's anatomy can be analyzed, and if there are certain deformations that are more likely, this knowledge can be used to create a plan that is robust even with the anatomical uncertainty.

In this chapter, patient-specific statistical motion models are created using principal components analysis. The PCA technique has been used previously to model the organs of the pelvis, most notably in the work of Sohn.[46] In their work, PCA was used to model the shapes of the prostate, bladder, and rectum. Four eigenmodes were found to be sufficient to describe each of their four patient's daily organ shapes to within 2 mm. While this work laid the framework for individual modeling using PCA, it was limited in its applications. Their PCA models were limited to the organ shapes, ignoring the daily anatomical changes within and outside of the three organs analyzed. In this thesis, PCA will be used to develop models for all of the patient's anatomy using DIR of a series of fan-beam CT images.

2.1.1. Systematic and random errors

In this work, a patient-specific model was created by partitioning daily anatomical differences into systematic and random components. These components are defined and discussed in the context of what is define as "traditional radiotherapy" in this thesis.

In traditional radiotherapy, a patient comes in for a pretreatment CT. This image is then used to create a desirable treatment plan that is to be used for the entirety of the patient's treatment regimen. Thus, this image is called the planning image. This planning image only represents one of the many possible anatomical instances of this patient. In a worst-case scenario, this anatomy can represent an unlikely instance of the patient's possible anatomies, and thus introduce a systematic difference between the dose intended to be delivered and the dose actually delivered. For this treatment methodology, one hopes that the planning image represents the patient's average anatomy. In this work, systematic error was defined as the difference between the patient's planning anatomy and the patient's mean anatomy, averaged over the course of treatment. A simple 1D example of systematic error is shown graphically below in Figure 1.

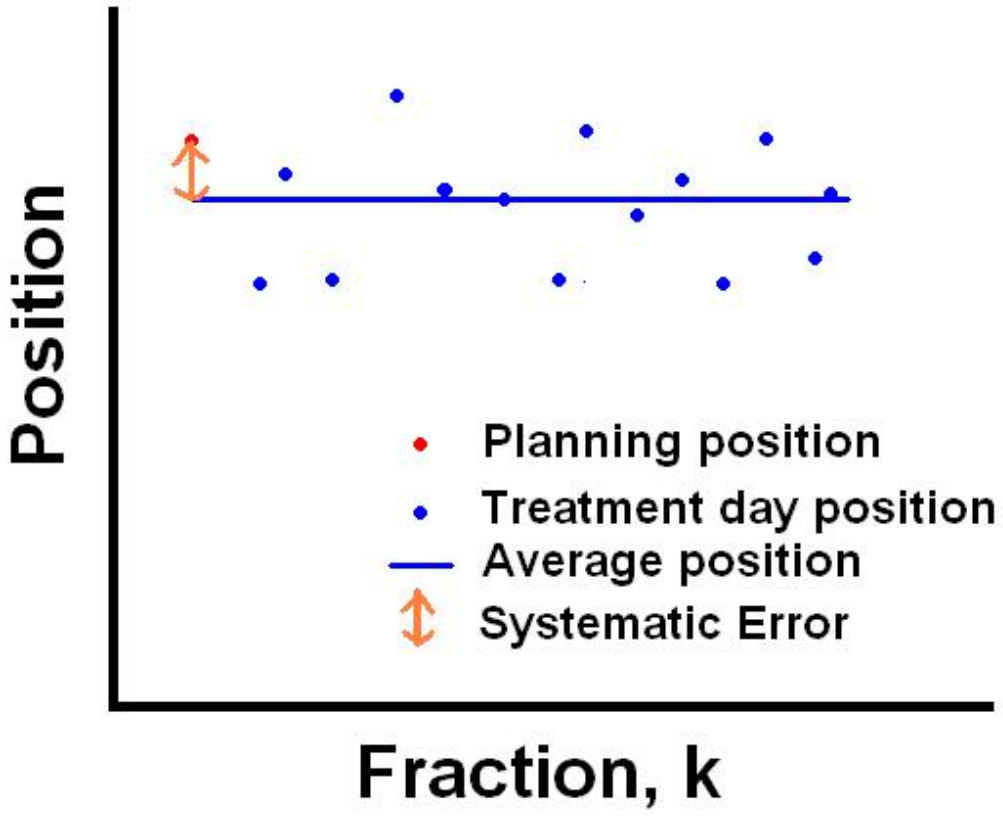

***Figure 1*. 1D example of systematic error. The points represent the patient's treatment isocenter on each day, k. The blue line is the patient's average treatment position over the course of therapy. The orange line is the systematic error, or the difference between the planning isocenter and the mean isocenter position.**

Determining and planning on the patient's mean anatomy does not eliminate anatomical errors by itself. The daily fluctuations between the mean anatomy and the daily anatomy will also alter the delivered dose distribution. These residual differences are known as the patient's random error. The sum of the systematic and random error equal the displacement of the patient's planning anatomy from the patient's anatomy at the time of treatment. Therefore, there is a single, constant systematic error for each patient and a different random component for each treatment day. These errors are defined more rigorously in the following sections.

2.2. Creating the patient-specific model

In this section, the patient dataset used throughout this thesis is outlined, as well as an overview of the deformable image registration (DIR) algorithm used. The concepts of systematic and random error are mathematically defined, and a principal component analysis technique is applied to the data to create a patient-specific 3D statistical model.

2.2.1. Patient dataset

The patient dataset used in this thesis consisted of a set of serial anonymized fan beam CT images, $I_{i,k}(\mathbf{x})$, of the male pelvis for patients undergoing definitive EBRT for prostate cancer. These images were obtained from the Netherlands Cancer Institute (NKI), where $I_{i,k}(\mathbf{x})$ is the image intensity at voxel **x** of the CT of the i^{th} patient acquired at his k^{th} fraction. Each of the $N = 19$ patients ($i = 1, \cdots, N$) had planning (k=0) and $P_i = 8, \cdots, 13$ (median 11) fractional images ($k = 1, \cdots, P_i$) acquired throughout the course of treatment. There were 210 fractional images used in this study. On each of these images, the prostate, bladder, and rectum were contoured by a single experienced radiation oncologist. The images were initially rigidly aligned on bony anatomy. The cutoff for the superior boundary of the rectum was the inferior edge of the iliosacral joints. Patients were instructed to evacuate their bladder and rectum one hour prior to treatment. Afterwards, they were told to drink 250 mL of water. The staging of the patients and other details of treatment are given by Deurloo.[57]

2.2.2. Deformable image registration

To quantify the differences between the anatomy of the day and the planning anatomy, DIR was used. DIR is the process of determining the mapping of each voxel in one image (the fixed image) to its corresponding location in another image (the moving image). These mappings are represented by vectors anchored at the voxel centers of the fixed image. These vectors "point" to the corresponding location in the moving image. For each patient in this dataset, the Eulerian transformation, $\mathbf{h}_{(i,k)\to(i,0)}\left(\mathbf{x}_{i,0}\right)$, was defined as

$$\mathbf{h}_{(i,k)\to(i,0)}\left(\mathbf{x}_{i,0}\right) = \mathbf{x}_{i,0} + \mathbf{u}_{(i,k)\to(i,0)}\left(\mathbf{x}_{i,0}\right) \quad (1)$$

Here, $\mathbf{u}_{(i,k)\to(i,0)}\left(\mathbf{x}_{i,0}\right)$ is the DVF that associated with $\mathbf{h}_{(i,k)\to(i,0)}\left(\mathbf{x}_{i,0}\right)$ and $\mathbf{x}_{i,0}$ is the planning image coordinate system for the patient. The transformation maps the spatial locations, $\mathbf{x}_{i,0}$ in the patient's planning image, $I(\mathbf{x}_{i,0})$, to the corresponding location, $\mathbf{x}_{i,k}$, in his treatment position image, $I(\mathbf{x}_{i,k})$.

In this work, the small deformation, inverse consistent, linear elastic (SICLE) DIR algorithm was used in order to compute the transformation. Details about this algorithm have been published.[58] SICLE calculated the initial set of DVFs used in this work using both grayscale and contour information. SICLE's objective function contains intensity matching, inverse consistency, and regularizing terms. The intensity matching was done by minimizing the sum of squares differences of CT intensities and contour information. Contours were incorporated by converting each one to a binary mask image. The optimization was simultaneously done on these binary mask images as well as on the grayscale CT images. The contours used in these studies were the prostate,

bladder, and rectum. The algorithm simultaneously searches for both forward, $\mathbf{h}_{(i,k)\to(i,0)}\left(\mathbf{x}_{i,0}\right)$, and inverse, $\mathbf{g}_{(i,0)\to(i,\mathrm{k})}\left(\mathbf{x}_{i,\mathrm{k}}\right)$, DVFs relating the two input images and their associated contour masks. The objective function contained terms penalizing inverse inconsistent registrations. Finally, a linear elastic regularizing term was also included in the objective function. The transformation was parameterized using a Fourier basis, with the Fourier basis coefficients representing the transform parameters being actively optimized. The algorithm utilized a multi-resolution approach, first by minimizing the objective function on a course image grid and then by iteratively refining the Fourier coefficients on a finer resolution. The final DVFs spanned the whole image with voxel sizes of approximately 1.8x1.8x0.3 mm.

2.2.3. Construction of the patient-specific PCA model

A patient-specific statistical model gives the magnitude, direction, and likelihood of a given deformation between the patient's anatomy at the time of planning and the anatomy at the time of treatment. As each model described the organ motion for a particular patient, one model was constructed to describe the anatomical motion of each patient, i, in the dataset. To build the models, CT images from different days were deformably registered to their planning image. As each daily image was registered to the same planning image, each DVF shared the domain of the planning image, $\mathbf{x}_{i,0}$. Together, the DVFs represented repeated measurements of how the anatomy in the planning image moved from day to day. From these DVFs, a systematic error DVF could be easily computed for the i^{th} patient as

$$\bar{\mathbf{u}}_i\left(\mathbf{x}_{i,0}\right)=\frac{1}{P_i}\sum_{k=1}^{P_i}\mathbf{u}_{(i,k)\to(i,0)}\left(\mathbf{x}_{i,0}\right) \tag{2}$$

for patient i with P_N fractional images. The random error component for each fraction could then be found as the residual error after correcting for the systematic error

$$\Delta\mathbf{u}_{(i,k)\to(i,0)}\left(\mathbf{x}_{i,0}\right)=\mathbf{u}_{(i,k)\to(i,0)}\left(\mathbf{x}_{i,0}\right)-\overline{\mathbf{u}}_i\left(\mathbf{x}_{i,0}\right) \tag{3}$$

Since the systematic error was constant for the duration of treatment, an individual patient deformation model, hereafter referred to as the individual model, was based solely on random error displacement. This work used principal component analysis to create a patient's individual model. For a more technical description of PCA, please refer to Appendix A. The covariance matrix used as input to the PCA was constructed as follows

$$\mathbf{C}_i=\operatorname{cov}\left(\Delta\mathbf{u}_{(i,k)\to(i,0)}\left(\mathbf{x}_{i,0}\right)\right)=\frac{1}{P_i}\sum_{k=1}^{P_i}\Delta\mathbf{u}_{(i,k)\to(i,0)}\left(\mathbf{x}_{i,0}\right)\cdot\Delta\mathbf{u}_{(i,k)\to(i,0)}\left(\mathbf{x}_{i,0}\right)^T \tag{4}$$

PCA is the eigendecomposition of this covariance matrix, which determines the linearly independent orthonormal eigenvectors, $\mathbf{v}_{i,l}$, and eigenvalues, $\lambda_{i,l}$, that satisfy the following equation

$$\mathbf{C}_i\mathbf{v}_{i,l}=\lambda_{i,l}\mathbf{v}_{i,l} \tag{5}$$

The eigenvalues represented the fraction of the variability in the data corresponding to its associated eigenvector. The eigenvalues were sorted, with the largest one associated with the most principal component, $\mathbf{v}_{i,1}$, the second highest with the second most principal component, $\mathbf{v}_{i,2}$, and so forth. The first L eigenvectors were kept. The principal components formed an orthogonal basis, which could be used to reconstruct the original SICLE DVF

$$\mathbf{u}_{(i,k)\to(i,0)}\left(\mathbf{x}_{i,0}\right)=\sum_{l=1}^{L}c_{i,l}\mathbf{v}_{i,l}+\overline{\mathbf{u}}_i\left(\mathbf{x}_{i,0}\right) \tag{6}$$

where $c_{i,l}$ were scaling coefficients calculated by

$$c_{i,l} = \Delta\mathbf{u}_{(i,k)\to(i,0)}\left(\mathbf{x}_{i,0}\right)\bullet\mathbf{v}_{i,l} \tag{7}$$

2.2.4. Kernel density estimation

The eigenvectors resulting from the PCA were linearly independent of one another. This means that the probability of a given deformation was the same as the probability of randomly sampling the associated set of expansion coefficients to be used in conjunction with equation (24) in Appendix A. Selecting appropriate expansion coefficients maintained the spatial correlation between the voxels while possibly reducing the dimensionality, if certain eigenvectors added little to describing the variance in the data. For these reasons, it was desirable to be able to randomly sample these expansion coefficients from a probability density function (PDF). Following the method of Murphy *et al.*,[59] the calculation of these PDFs was determined using kernel density estimation (KDE), also called Parzen windowing.[60,61] In the end, there was one PDF associated with each eigenvector.

Practically, this was done by creating a histogram of the training coefficients, $c_{i,l}^{k}$, associated with each eigenvector, $l = 1\cdots L_i$. In order to represent 100% of the variance in the daily deformations, $L = P_i - 1$. The training coefficients were the expansion coefficients needed to represent the SICLE generated DVFs as a linear combination of the eigenmodes, $\mathbf{v}_{i,l}$. Each of the daily random errors could be reconstructed using the patient's systematic error, a set of L_i eigenvectors, and their associated expansion coefficients. The coefficients were calculated using equation (25) in Appendix A.

The expansion coefficients were found for each fractional DVF and eigenmode, l, creating a matrix of coefficients for each patient, i.

$$\mathbf{c}_i = \begin{bmatrix} c_{i,1}^1 & \cdots & c_{i,1}^k & \cdots & c_{i,1}^{P_i} \\ \vdots & \ddots & \cdots & \iddots & \vdots \\ c_{i,l}^1 & \cdots & c_{i,l}^k & \cdots & c_{i,l}^{P_i} \\ \vdots & \iddots & \cdots & \ddots & \vdots \\ c_{i,L_i}^1 & \cdots & c_{i,L_i}^k & \cdots & c_{i,L_i}^{P_i} \end{bmatrix} \tag{8}$$

The columns of the coefficient matrix, $\mathbf{c}_i$, represent the coefficients needed to reconstruct the fractional DVFs. The rows represent the coefficients corresponding to a particular eigenmode.

PDFs were calculated for each eigenmode, each using the coefficients in the corresponding row of $\mathbf{c}_i$. In this study, a continuous Gaussian kernel was used for the KDE, which centered a Gaussian around each coefficient for a given eigenmode. The resultant PDF was then constructed as the superposition of these Gaussians. The mathematical formulation is given in Equation (9) for the l^{th} eigenvector

$$p_{i,l}(c) \approx \frac{1}{P_i\sqrt{2\pi b^2}} \sum_{k=1}^{P_i} \exp\left(\frac{-\left(c - c_{i,l}^k\right)^2}{2b^2} \right) \tag{9}$$

where b is a user-adjustable bandwidth parameter. This parameter adjusts the width of the Gaussian kernel used. In this work, the parameter was calculated from a heuristic rule of thumb put forth by Silverman[62]:

$$b = 1.06\left(N^{-1/5}\right) SD_{data} \tag{10}$$

where SD_{data} is the standard deviation of the training coefficients ($c_{i,l}^{1}$ - $c_{i,l}^{P_i}$) associated with a particular eigenmode, l. Using this method, one PDF was generated for each of the L_i principal components.

2.2.5. Sampling coefficients from the KDE-generated PDFs

For patient-specific random error uncertainty, sampling the expansion coefficient PDFs allowed for the creation of "synthetic DVFs," $\mathbf{u}_{(i,\text{syn})\to(i,0)}\left(\mathbf{x}_{i,0}\right)$, by inserting sampled coefficients, $c_{i,l}^{syn}$, into the following equation:

$$\mathbf{u}_{(i,\text{syn})\to(i,0)}\left(\mathbf{x}_{i,0}\right)=\sum_{l=1}^{L_i} c_{i,l}^{syn}\mathbf{v}_{i,l}+\overline{\mathbf{u}}_i\left(\mathbf{x}_{i,0}\right) \tag{11}$$

The synthetic DVFs were statistically consistent with those in the training set, meaning that there should have been no significant difference in the spread of the training set vectors and the corresponding synthetic ones. To sample each PDF, a rejection sampling technique was implemented in this research. The tails of the PDFs were nonzero and extended to infinity. Because of this range, the tails were cut off to improve the sampling efficiency. The cutoff was made to meet the requirement that the function at this point was at least 0.0001 of the maximum value.

2.2.6. Evaluation of the patient-specific PCA model

As an initial evaluation of the patient-specific model, the original SICLE DVFs were reconstructed as linear combinations of eigenmodes and expansion coefficients. More rigorously, the statistical correlation of synthetic DVFs output from the patient-specific PCA model with the training DVFs were confirmed. Specifically, in this section I compare the distribution of voxel vectors in the training set to those synthetically

created. Hypothesis testing was performed to determine any significant difference between the distributions.

2.2.6.1. Evaluation of the patient-specific PCA model's ability to reconstruct training DVFs

PCA allows one to represent the original SICLE DVFs, $\mathbf{u}_{(i,k)\to(i,0)}\left(\mathbf{x}_{i,0}\right)$, as a linear combination of eigenmodes and scalar expansion coefficients. If no eigenmodes are discarded ($L_i = P_i - 1$), the PCA model should reconstruct the training data perfectly using equations (6) and (7). This is the simplest check that the eigenvectors and expansion coefficients are being calculated correctly. Performing this test with all fractional DVFs for all patients, PCA was able to reconstruct each DVF perfectly.

2.2.6.2. Direct evaluation of individual model on voxel vectors

The evaluation above indicates that the individual patient statistical PCA method was correctly calculating the eigenvectors and expansion coefficients. This check, while important, does not test the KDE or PDF sampling of the PDFs. The general flow of the evaluation used to check the entire modeling process is given in Figure 2. In this methodology, 1000 synthetic DVFs were created using equation (11). At this point, the 1000 vector values were extracted from each voxel located within the prostate, bladder, and rectum contours as defined on the planning image. The 11-13 corresponding vector values from these same voxels were then extracted from the original SICLE calculated DVFs. Finally, differences in the distributions of the synthetic and calculated vector values were tested against the null hypothesis ($p<0.05$ criteria used) at each organ occupied voxel. The Wilcoxon rank-sum test was used for the hypothesis testing.

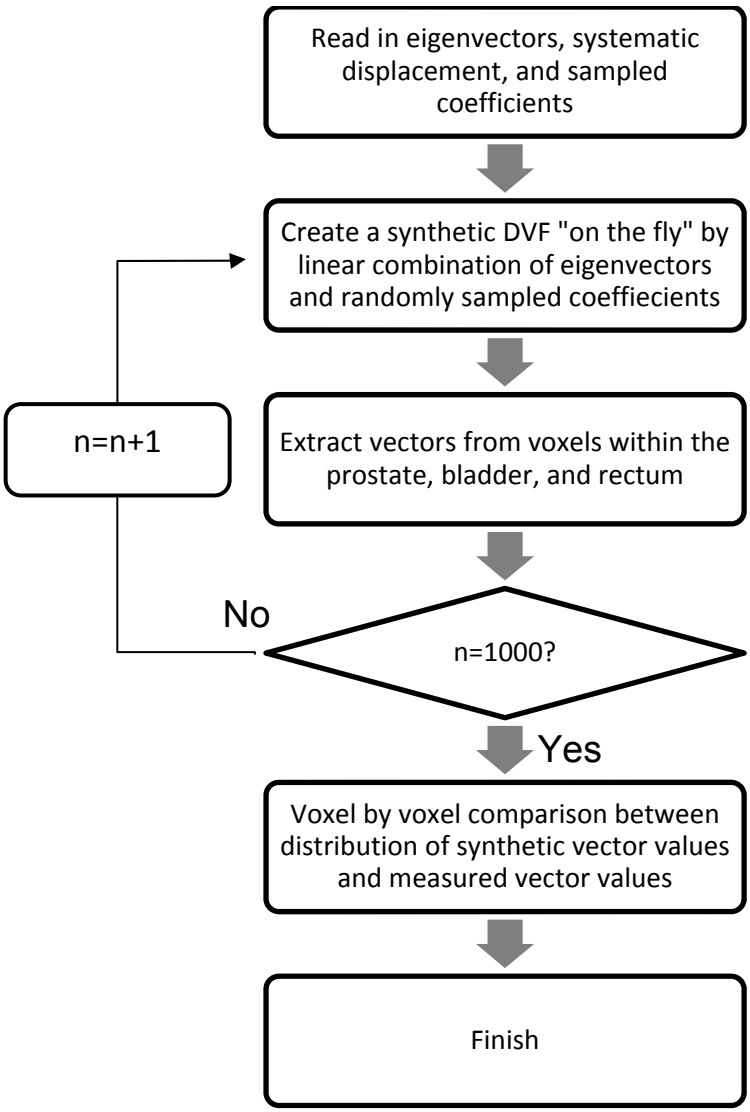

***Figure 2*: Flowchart for the evaluation of the individual PCA model. This flowchart was used for all patients; it extracted the vector values at voxels within the organs of interest (prostate, bladder, and rectum) to be compared with those of those in the SICLE generated DVFs.**

For all patients, there were no significant differences in the vector distributions for any voxels within each patient's planning regions of interest. A histogram of all of the p-values for all voxels in the patient population is given in Figure 3. This result was to be expected, as the PCA model was designed to recreate the distributions of the data

used in the input. Although the PCA model has the ability to create unique synthetic deformations, these deformations are probabilistically tied to the distribution of the underlying measured data.

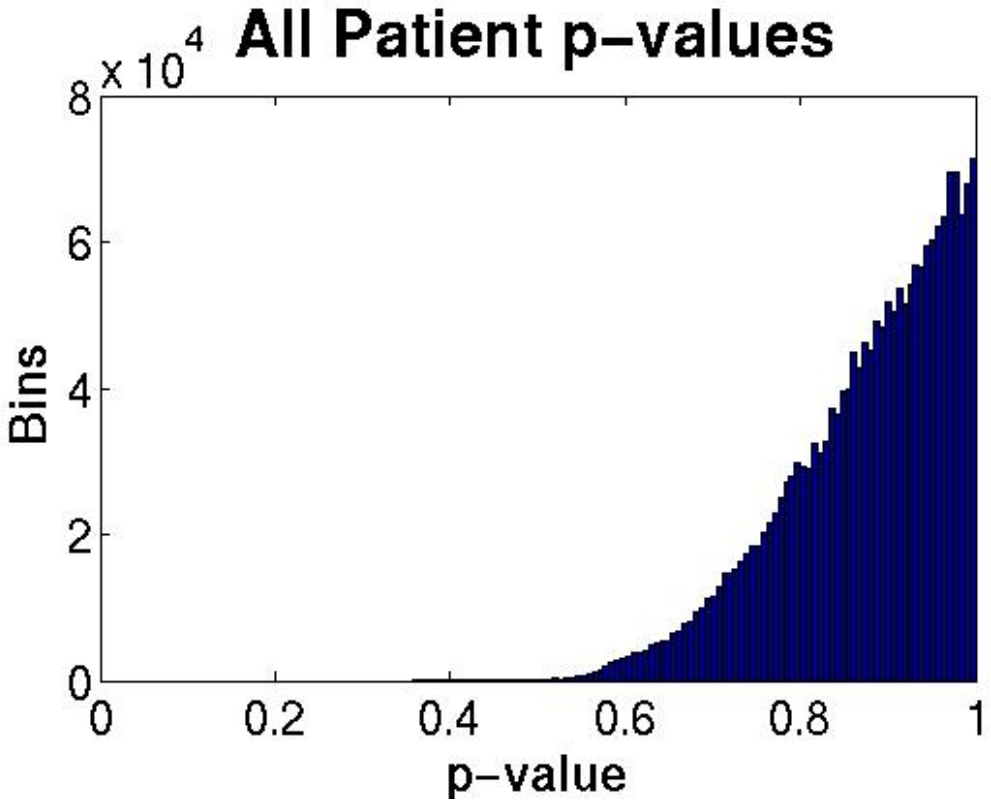

***Figure 3*: Histogram of p-values from hypothesis testing (Wilcoxon rank-sum test) of the synthetic and true voxel vector distributions. No differences were found to be significant, with the minimum p-value equal to 0.36.**

For illustrative purposes, the displacement for a single voxel (located centrally within the prostate) was investigated in one patient. The voxel center (in $\mathbf{x}_{i,0}$) was displaced with the SICLE DVFs, $\mathbf{u}_{(i,k)\to(i,0)}\left(\mathbf{x}_{i,0}\right)$, creating a distribution of points. These points are the locations of that piece of tissue on each training image. The voxel center

in the planning image was similarly displaced with 1000 synthetically sampled DVFs, $\mathbf{u}_{(i,\text{syn})\to(i,0)}\left(\mathbf{x}_{i,0}\right)$, from the individual PCA model, creating its own distribution of locations of this voxel. A 3D scatter plot of the displaced voxel location is shown in Figure 4. Assuming the individual PCA model was correctly implemented, these two distributions should be identical. The distribution means and standard deviations of the two distributions, as well as the p-values, are given in Table 2. The results show no significant differences in the distributions.

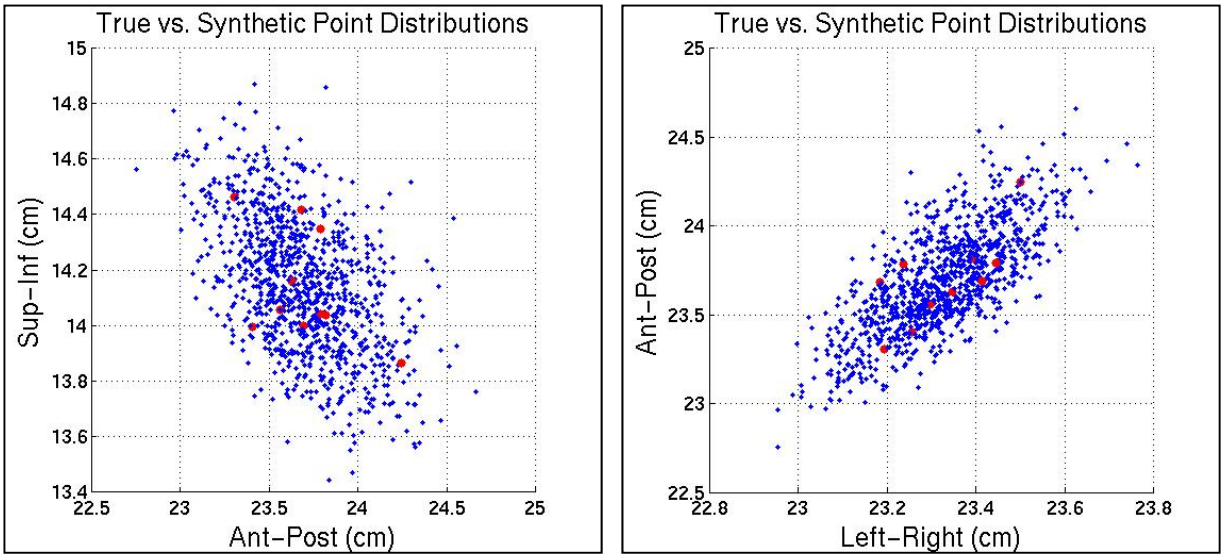

***Figure 4*: 3D distribution of a central prostate point location after being displaced with the training SICLE DVFs (red) and sampled synthetic DVFs (blue). This was done for a single sample patient.**

Table 2: The mean and standard deviations of deformed central prostate location (cm) in the LR (left-right), AP (anterior-posterior), and SI (superior-inferior) directions for the SICLE DVFs (measured data) and the synthetically sampled DVFs (synthetic data). The p-value calculated from a Wilcoxon rank-sum test is also given between the two distributions.

Prostate		LR	AP	SI
Measured Data	Average Position (cm)	23.32	23.69	14.14
	Standard Deviation (cm)	0.11	0.26	0.11
Synthetic Data	Average Position (cm)	23.32	23.69	14.14
	Standard Deviation (cm)	0.12	0.28	0.13
Hypothesis Testing Between Distributions	p-value	0.99	0.97	0.86

These tests demonstrated the individual model's ability to create many synthetic deformations taken from a distribution probabilistically tied to that of the original training DVFs. These results give confidence that the KDE method implemented in this work created meaningful PDFs for sampling coefficients. With these tools in hand, the problem of sampling synthetic deformations probabilistically tied to the training data can be reduced to sampling a set of expansion coefficients from their associated PDFs to be incorporated into equation (11).

However, there are limitations to these tests. The analysis above only checks the ability to create synthetic DVFs consistent with the measured DVFs input into the PCA. This does not test PCA's ability to correctly predict the statistics of tissue deformation for an individual not included in the original training set. Although the model represents the training data, there is no check that the set of training data samples was sufficiently large enough to represent the underlying distribution of organ

motion. Ideally, a study to test this would be designed as follows. First, a PCA model would be created using the methods described above from a set of DVFs mapping a patient's fractional anatomy to his planning anatomy. This model would then be tested on its ability to represent DVFs not included in the PCA training set. The expansion coefficients would be calculated using equation (7), at which point they would be inserted into equation (11) to calculate the PCA model approximation of the non-training set DVFs. How well the model estimates the non-training set DVFs is a measure of how robust the model is in representing the patient's organ motion. This more complete validation was not possible in the current work, as it required larger amounts of data than were available.

2.2.7. Potential applications

2.2.7.1. Virtual clinical trials (VCTs)

The patient-specific PCA model has the potential to be a useful tool when performing VCTs. A VCT is a framework for testing a clinical hypothesis using virtual patient data and theoretical outcome (bio-effective) models instead of actual patients and clinically observed rates of control and toxicities. This is quite useful in radiation therapy. Different planning and delivery techniques can be simulated in a treatment planning system (TPS) on the patient's planning image. The resultant fluence maps can then used to calculate the daily dose deposition, given the patient's different daily anatomies (daily images). DVFs are used to deform the dose to the planning image, where the total dose over the course of treatment can be accumulated on a voxel-by-voxel basis. The resultant dose distributions from the various planning techniques can then be directly compared. This is generally done with a temporal sequence of CT

images simulating the patient's anatomy on a given treatment day. In practice, it is not common to give a patient enough CT scans to simulate an entire fractionation treatment. This is where the PCA model might be of some benefit.

Using a limited number of patient CT images with their resultant DVFs mapped to the planning image, the PCA model can synthetically create an infinite number of unique deformations that are statistically correlated to the input DVFs. There are two main benefits for doing this. First, an entire fractionation scheme of synthetic anatomies can be created using a smaller number of input images. This is done by deforming the planning CT with the inverse of the synthetic DVFs generated with the PCA model. This provides the experimenter with numerous daily anatomies and their exact corresponding DVFs, relating the daily image to the planning image. Using the known DVF, contours can easily and accurately be propagated onto the image of the day. Also, the synthetic DVF can be used to accumulate dose over a fractionated treatment. Using the simulated forward and inverse synthetic DVFs to create the virtual data eliminates any registration errors that would occur by using an imperfect deformable image registration algorithm on "real" daily images. Example synthetic geometries are given in Figure 5.

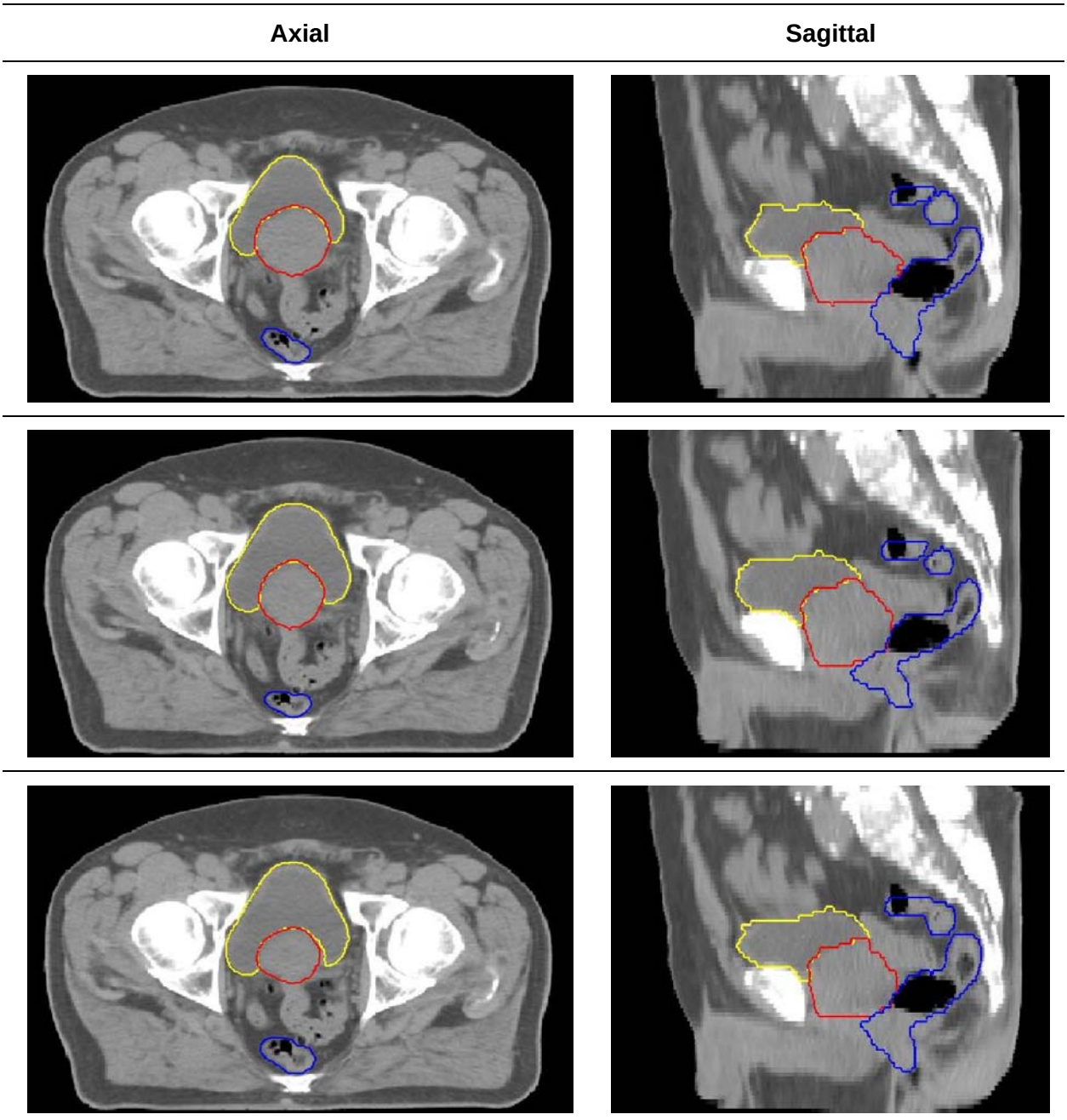

***Figure 5*: Axial and Sagittal views of three different synthetic geometries for a single patient created using the individual PCA model.**

There are some limitations to the PCA model approach to VCTs. The first is that the resultant synthetic DVFs are only as good as the underlying data used as input to the PCA. If there is some component of a patient's anatomical variation that is not

present in the training data, this component will also be absent from any PCA model derivative anatomy. It is therefore important to utilize an adequate number of input DVFs in order to model the full variability of organ motion in that patient. For this reason, it is also important to use the best possible DVFs as input to the PCA. This study used DVFs that were generated using both grayscale matching and manually drawn contour coincidence to drive the registration. The rationale was to use as much *a priori* knowledge as possible to get the most accurate transformation possible describing the deformation.

Another limitation to using the PCA model is the inability to create wildly different anatomies. All synthetic anatomies are created by deforming the patient's planning image with a known DVF. Because of this, only features present in the planning image will be present in the synthetic image. For example, if the planning image had contained a large gas pocket in the rectum, this feature would be present in all synthetic images created by way of the PCA model. The gas pocket may expand or shrink, but it will never go away completely. This is not the reality, as the presence of bowel gas in patients routinely changes day-to-day. This problem could be addressed by deforming the different daily images to the planning image coordinate system, creating a set of planning image-like images. These images would maintain the basic anatomical positions, but with varying amounts of bowel gas.

2.2.7.2. Individual model as input to probabilistic planning

This PCA model potentially holds some value when used in conjunction with PTP. All PTP methods designed to account for interfractional motion need an estimate of the distribution of the potential daily errors. The PTP algorithm can only account for

organ motion described in its underlying measure of the patient's anatomical uncertainty. It is here that the PCA model described above would be of benefit.

One such PTP algorithm in which the individual PCA modeling has been incorporated is in coverage optimized planning (COP), as first proposed by Gordon *et al*.[56] The aim of COP is to build a plan robust to anatomical uncertainty using coverage probability. This creates a plan where there is a high (i.e., >95%) probability that a structure will be covered by certain dosimetric criteria on any given day. COP uses the concept of the dose coverage histogram, which is a cumulative distribution of all possible voxel doses in the presence of geometric uncertainties. COP then optimizes on the dose coverage histogram, choosing a plan with a high probability (i.e. 95%) of delivering a given cumulative dose to the patient over the whole course of treatment. In the initial proof-of-concept paper, a rigid prostate was assumed, with the standard deviation of the distribution of systematic and random errors set to 3 mm. A shift was determined as the sum of two samples taken from the systematic and random normal distributions. These shifts were used to calculate the coverage probability, completely ignoring deformation.

To expand this concept, the work presented in this thesis was coupled with the research being done with COP. Instead of rigidly translating the prostate by an estimated normal distribution, the PCA model was used to create a more realistic patient model for the coverage probability calculation. Thus, fully 3D deformations of the patient's anatomy were taken into account when optimizing the plan. This work, of which the author of this thesis was a coauthor, was led by Xu and is described in a paper published in *Medical Physics*.[63] In this paper, the individual model described

above was used to create the virtual dataset of synthetic anatomies needed to compare COP technique (CP_{COP}) to two other planning techniques. One planning technique created a plan utilizing a fixed, 5 mm uniform margin (FM) and the other utilizing an optimized uniform margin (CP_{OM}). The optimized margin was the uniform margin needed to ensure that the D_{98} was greater than or equal to the prescription dose with 95% coverage probability ($D_{98,95}$). Utilizing the same prostate patient cohort, Xu compared the plans using dose coverage criteria as well as complication-free tumor control probability (P+). In the plans, the prostate prescription dose was 78 Gy, with the seminal vesicles prescription being 66 Gy. The two dose limiting structures were the bladder and the rectum, with an artificial ring structure used for IMRT optimization. The results are summarized below; the reader is referred to the paper for the details of planning and a full analysis of the results.

Of the three plans, CP_{COP} was favored in 7/19 patients, while CP_{OM} was favored in 12/19 patients, with the advantages of each plan being patient specific. The patient-by-patient advantages are given in Table 3, taken from Xu's paper with permission.

Table 3: Patient study ID, the preferred planning technique and the most representative gain with respect to the other two plans in terms of target dose D98,95 for the prostate CTV (CTVprostate) or the seminal vesicles CTV (CTVSV), normal tissue coverage Dv,5 for bladder or rectum, and probability of complication free control P+. ID with */ † / ‡ denotes CPCOP / CPOM / FM plan that fails to achieve target D98,95.

ID	Best Plan	Gain Relative to the Other Plans	
1*	CP_{OM}	CP_{COP} (+0.8% $CTV_{prostate}$ $D_{98,95}$)	FM (+6.5% P+)
2*†‡	CP_{OM}	CP_{COP} (+4.0% $CTV_{prostate}$ $D_{98,95}$)	FM (+1.3% $CTV_{prostate}$ $D_{98,95}$)
3*	CP_{OM}	CP_{COP} (+3.4% $CTV_{prostate}$ $D_{98,95}$)	FM (+2.8% P+)
4*‡	CP_{OM}	CP_{COP} (+7.3% CTV_{SV} $D_{98,95}$)	FM (+1.0% $CTV_{prostate}$ $D_{98,95}$)
5*	CP_{OM}	CP_{COP} (+7.2% CTV_{SV} $D_{98,95}$)	FM (+11.9% P+)
6*	CP_{OM}	CP_{COP} (+1.0% $CTV_{prostate}$ $D_{98,95}$)	FM (+21.5% P+)
7	CP_{COP}	CP_{OM} (-3.2% Rectum, $D_{2,5}$)	FM (+4.2% P+)
8*	CP_{OM}	CP_{COP} (+9.8% CTV_{SV} $D_{98,95}$)	FM (+0.9% P+)
9*†‡	CP_{OM}	CP_{COP} (+7.3% CTV_{SV} $D_{98,95}$)	FM (+5.0% CTV_{SV} $D_{98,95}$)
10*†‡	CP_{COP}	CP_{OM} (+1.2% CTV_{SV} $D_{98,95}$)	FM (+5.5% CTV_{SV} $D_{98,95}$)
11‡	CP_{COP}	CP_{OM} (+5.9% P+)	FM (+1.1% $CTV_{prostate}$ $D_{98,95}$)
12†‡	CP_{COP}	CP_{OM} (+0.8% $CTV_{prostate}$ $D_{98,95}$)	FM (+2.4% $CTV_{prostate}$ $D_{98,95}$)
13	CP_{OM}	CP_{COP} (+2% P+)	FM (+3.1% P+)
14	CP_{OM}	CP_{COP} (-3.1% Rectum, $D_{2,5}$)	FM (+3.3% P+)
15*	CP_{OM}	CP_{COP} (+8.8% $D_{98,95}$)	FM (+22.8% P+)
16‡	CP_{COP}	CP_{OM} (+1.7% P+)	FM (+1.0% $CTV_{prostate}$ $D_{98,95}$)
17*	CP_{OM}	CP_{COP} (+3.9% CTV_{SV} $D_{98,95}$)	FM (+9.5% P+)
18*†‡	CP_{COP}	CP_{OM} (+0.6% $CTV_{prostate}$ $D_{98,95}$)	FM ((+0.8% $CTV_{prostate}$ $D_{98,95}$)
19	CP_{COP}	CP_{OM} (-0.6% Rectum $D_{30,5}$)	FM (+6.4% P+)

Table reprinted from Xu with permission.

2.2.7.3. Individual PCA model as input to adaptive planning

The patient-specific PCA model has potential application to IGART. Without a sufficient number of images, it is impossible to characterize sufficiently the patient's anatomical motion. Thus, it is impossible to utilize this statistical model before that patient starts treatment. However, in-room daily patient imaging (such as CBCT) is now commonly used for patient setup and verification. These images may be collected during the first several, usually 5, treatment fractions. A Beaumont-style ART method

could be implemented by building the patient's individual PCA model offline using these initial 5 daily CTs. The PCA model could then be used to create an adaptive plan to be delivered for future treatments. This could be done once, or continually throughout treatment, as more information about the patient's anatomical motion becomes available.

Future research is needed to test the feasibility of this method for the PCA model. There are several unknowns and complicating factors that would have to be resolved before this is deemed a viable option. First, CBCT images are of substantially worse quality when compared to the fan-beam CT images used in the planning process. This lack of image quality makes the initial registrations difficult. Secondly, the number of images needed to estimate adequately the patient specific organ motion distribution requires investigation. Using too few images could cause the PCA to miss some modes of motion completely. Beaumont ART uses Kalman filtering to account for the residual uncertainty from using a limited number of daily images. A similar method could be implemented for the patient-specific PCA model.

2.3. Conclusion

In this chapter, a methodology was described for creating a patient-specific statistical model of day-to-day random anatomical deformations. Such models were built for all 19 patients in the dataset, and each model was validated by comparing the distribution of the vectors in the initial dataset to synthetically created vectors. These models have potential applications in virtual clinical trials, probabilistic treatment planning, and image guided adaptive radiation therapy.

3. Population PCA modeling of systematic and random tissue displacement errors in prostate cancer

3.1. Introduction

In general, a patient-specific statistical model of anatomical motion is not possible before the start of treatment. Several days' worth of images are required to create a model that can accurately describe the magnitude and likelihood of the patient's organ motion, when conventionally there is only a single planning image taken before treatment. In this scenario, a population statistical model, such as one created using PCA, could prove beneficial. A population model could determine the magnitude and likelihood of systematic and random deformations across a patient population. A population model also has the potential to model residual systematic and random errors that remain after a deterministic correction (i.e. aligning to fiducial markers or organ centroid). Currently, these residual uncertainties remain unaccounted for. This knowledge can be directly incorporated into the planning process by determining the probability of an organ of interest occupying a given volume in the patient's planning image.

PCA has previously been applied to the population modeling problem in the work of Budiarto *et al*.[49] In their paper, they created a population shape model of prostate and seminal vesicle random displacement. With an 18 patient data set used to build the model, they were able to reconstruct the prostate/seminal vesicle shape of three patients not included in their training set to within 1.5 mm. This work only modeled the shape of these two organs, and did not take into account the complex motions of any

surrounding anatomy, including the bladder and rectum. Also, the work of Budiarto ignored any systematic displacements. The work in this thesis expands on this previous work by including both systematic and random displacement population modeling for the three organ system of the prostate, bladder, and rectum.

Population modeling is associated with a new set of challenges when compared to individual modeling. As described earlier, each patient has a single systematic error, which relates the patient's planning anatomy to the patient's mean anatomy. Each patient's systematic error is unique and cannot be computed before treatment. Thus, a population model of systematic tissue displacement must account for the distribution of all possible systematic errors. A similar distribution of random errors can be created across the patient population to form a population model of random tissue displacement. Both systematic and random error distributions should be considered when incorporating such modeling into the patient planning.

A reference coordinate system is needed in the formulation of both systematic and random error population models. Generally, PCA requires numerous measurements of a set of variables. The measurements used in this thesis are the displacement vectors "anchored" at the voxel centers of the reference image. The reference image used in the individual model was the patient's planning image. However, each patient's planning image had a unique coordinate system, which represents a problem when trying to pool systematic and random errors from different patients. In this chapter, I propose a solution to this problem: transporting each patient's individual systematic and random errors to a calculated reference anatomy. This is accomplished through the use of interpatient DIR.

With each patient's individual statistics transported to the reference coordinate system, the concept of Σ and σ (as described previously) can be extended from the traditional 1D formulation to 3D for both bony- and prostate centroid-aligned patient setups. PCA models for both systematic and random organ motion can be created in a similar fashion to the models described in Chapter 2. The detailed creation of these models and their validation is included in a manuscript to be submitted to *Medical Physics*, attached in Appendix B. This chapter summarizes the work reported in this manuscript, referring to the Appendix for the details and specific results.

3.2. Construction of a reference image using interpatient DIR

In order to determine any common modes of systematic or random tissue motion in a population of patients, a common coordinate system is needed. This is achieved by determining the transformation, $\mathbf{h}_{(i,0)\to ref}\left(\mathbf{x}_{ref}\right)$ that maps each patient's planning image, $I\left(\mathbf{x}_{i,0}\right)$, to a reference image, $I_{ref}\left(\mathbf{x}_{ref}\right)$. This registration can be used to transport patient-specific systematic and random errors into the reference coordinate system, $\mathbf{x}_{ref}$. Determining the interpatient transformations is a challenging task, as the anatomies in the two images being registered vary greatly. Straightforward application of SICLE, as described in the previous chapter, failed to converge to a solution. As a result, the prostate, bladder, and rectum were registered separately using contour-only driven registrations.

The construction of $I_{ref}\left(\mathbf{x}_{ref}\right)$ was done by registering each patient's planning image to a preselected patient's planning image using the organ-by-organ registrations. This preselected patient was chosen for its lack of abnormal anatomy (such as minimal

bowel gas, artifacts, average organ sizes) upon visual inspection. The resultant organ-specific DVFs were then averaged to determine the mean organ DVFs. Next, the mean DVFs were used to deform their associated organ in the preselected patient's planning anatomy to the mean organ shape across the patient population. These shapes were then stitched together to form the reference image, $I_{ref}\left(\mathbf{x}_{ref}\right)$, which was limited to the three pelvic organs. At this point, each of the patient's planning images was registered to $I_{ref}\left(\mathbf{x}_{ref}\right)$ on an organ-by-organ basis, giving the transformations $\mathbf{h}^{bladder}_{(i,0)\to ref}\left(\mathbf{x}_{ref}\right)$, $\mathbf{h}^{prostate}_{(i,0)\to ref}\left(\mathbf{x}_{ref}\right)$, and $\mathbf{h}^{rectum}_{(i,0)\to ref}\left(\mathbf{x}_{ref}\right)$, along with their inverses $\mathbf{g}^{bladder}_{(i,0)\to ref}\left(\mathbf{x}_{i,0}\right)$, $\mathbf{g}^{prostate}_{(i,0)\to ref}\left(\mathbf{x}_{i,0}\right)$, and $\mathbf{g}^{rectum}_{(i,0)\to ref}\left(\mathbf{x}_{i,0}\right)$.

3.3. Transporting patient-specific statistics to the reference coordinate system

The patient-specific systematic ($\bar{\mathbf{u}}_i\left(\mathbf{x}_{i,0}\right)$) and random ($\boldsymbol{\Delta}\mathbf{u}_{(i,k)\to(i,0)}\left(\mathbf{x}_{i,0}\right)$) errors were then transported into the reference coordinate system. This was done by treating the systematic and random errors as vector-valued images and deforming them using each of the transformations, $\mathbf{h}^{bladder}_{(i,0)\to ref}\left(\mathbf{x}_{ref}\right)$, $\mathbf{h}^{prostate}_{(i,0)\to ref}\left(\mathbf{x}_{ref}\right)$, and $\mathbf{h}^{rectum}_{(i,0)\to ref}\left(\mathbf{x}_{ref}\right)$. To form a single systematic, $\bar{\mathbf{u}}^{union,ref}_{i}\left(\mathbf{x}_{ref}\right)$, or random, $\boldsymbol{\Delta}\mathbf{u}^{union,ref}_{i,j}\left(\mathbf{x}_{ref}\right)$, error in the reference coordinate system, the resultant organ-specific motion errors were stitched together using equations (5) and (6) in Appendix B. This was done for two different patient setups, a bony-aligned setup and a prostate centroid-aligned setup. Practically, the difference between the two setups was the initial alignment of the patient planning and fractional images.

3.4. Inverse consistency error

The common coordinate system requires individual statistics from each patient to be mapped to the reference image. However, for the model to be of any value, information gained in the reference coordinates must be mapped back to a patient's local coordinate system. Any inverse inconsistency in the interpatient transformations mapping to and from the reference frame will introduce an "inverse consistency error." To quantify this, patient-specific systematic and random errors were mapped to the reference frame, and then immediately back to the patient's local coordinate system and compared with the original. The mean and standard deviations are reported in Appendix B (Figure 2 and Table 1). In each organ for all patients, the mean inverse consistency error is less than 0.2 mm, with over 99%, 98%, and 92% of the voxel-by-voxel inverse consistency errors less than 0.3 mm for the prostate, bladder, and rectum, respectively.

3.5. Quantifying systematic and random error distributions for the population

With each patient's individual statistics successfully transferred to the reference coordinate system, a statistical characterization of patient population was derived. This was done by expanding the concepts of group mean, M, systematic (Σ) and random (σ) error distributions to three dimensions. These concepts were originally used to describe the organ motion and setup error at a single point (prostate centroid), which was taken as a surrogate for the entire prostate. The three-dimensional formulations are given in Appendix B equations (8)-(10). Maps of these values for the two prostate centroid and bony patient setups are given in Appendix B (Figure 3 and Figure 4). The results are as expected, with the bony aligned Σ and σ values being smaller near bony

edges and a centroid-aligned setup showing smaller Σ and σ in the central portion of the prostate.

3.6. Population PCA modeling of systematic and random tissue displacement errors

PCA modeling was performed separately for systematic and random errors, as well for the two different patient setups. The PCA formalism for this scenario is given in Section II.F. of Appendix B and is done in the same manner described in the previous chapter. The two covariance matrices used for the systematic and random errors are of particular importance, given below.

$$\mathbf{C}^{sys} = \frac{1}{N-1}\mathbf{D}^{sys}\left(\mathbf{D}^{sys}\right)^{T} \tag{12}$$

$$\mathbf{C}^{rand} = \frac{1}{\sum_{i=1}^{N} P_i}\mathbf{D}^{rand}\left(\mathbf{D}^{rand}\right)^{T} \tag{13}$$

where $\mathbf{D}^{sys}$ and $\mathbf{D}^{rand}$ are the mean subtracted data matrices of the population of systematic and random errors, respectively. In total, the systematic PCA model is calculated from 19 systematic errors while the random PCA model is created from 210 random errors.

3.7. PCA modeling error

Unlike in the previous chapter, not all eigenvectors were used in the modeling. In both the systematic and random population PCA models, only the eigenvectors needed to represent 95% of the variance were kept. Eleven and 33 eigenmodes were needed for the systematic and random population models, respectively, to represent 95% of the variance in the data. Discarding some eigenmodes introduced error in reconstructing

the original set of systematic and random errors. To quantify this "PCA modeling error," the difference was computed between the original systematic and random errors and those reconstructed using the limited number of eigenvectors. For systematic error, the voxel-by-voxel differences were calculated for each organ, with 96% of all organ voxels having modeling error less than 1 mm. The patient-by-patient results for both systematic and random error are given in Figure 65 of Appendix B.

3.8. Leave-one-out study

The PCA models created in this chapter are only useful if they can accurately describe the systematic and random errors of patients not part of the original training set. To test this, a leave-one-out study was conducted, where 19 different systematic and random error PCA models were created, each one using data from only 18 patients. Each model was then used to reconstruct the systematic and random errors from the "left out" patient. Within each organ, the voxel-by-voxel differences between the reconstructed systematic and random errors were calculated, with the mean and standard deviations of these differences reported. The mean voxel differences were all near zero, but the standard deviations were on the order of several millimeters for some patients, as shown in Appendix B, Figure 76. For the patient population, the mean, absolute mean, and standard deviations of the modeling errors in the leave-one-out study are given in Appendix B, Table 3. The leave-one-out errors were larger for the systematic population PCA model, suggesting a larger dataset may be necessary to describe adequately the systematic anatomical motion in prostate cancer patients.

3.9. Organ occupancy maps

A straightforward and useful application of the population systematic and random PCA models is in the construction of organ occupancy maps, which give the probability of an organ occupying a certain voxel on any given treatment day. To do this, synthetic systematic and random errors must be sampled from their respective PCA models. The sampling was done using the technique outlined in the previous chapter, with KDE used to construct the PDFs for each eigenmode. In this work, the sampled systematic errors were added to the sampled random errors to produced synthetic deformations. These deformations were then used to deform the reference anatomy, representing possible instances of the treatment day anatomies. Each voxel was marked with a 1 if it was within the synthetic anatomy, and marked with a 0 otherwise, creating a binary image. This process was performed 1000 times, with the binary images averaged to yield probability of the organ occupying a given voxel on a given day. This was done for both bony- and centroid-aligned setups, and the results are given in Appendix B, Figure 87. The centroid alignment has greater certainty in prostate localization when compared with bony-aligned setup.

3.10. Discussion

This chapter outlines the creation of fully 3D population models of systematic and random organ motion in prostate cancer patients. Patient-specific data was transported to the reference frame via interpatient DIR. These interpatient registrations were a difficult task; large discrepancies in patient anatomies caused the SICLE algorithm to fail in instances where the whole CT image was used. Alternatively, this work used a method where each organ was registered separately using contour information only.

Although this approach was feasible for the prostate, bladder, and rectum, other pelvic structures of interest such as the pelvic lymph nodes and seminal vesicles were not modeled in this work. Using a contour-only registration also made the modeling dependent on SICLE's regularization (linear-elastic constituitive law). For this reason, it is possible a finite-element DIR algorithm would have been better suited to this work, as it can produced non-diffeomorphic DVFs with support limited to the specified organs.

For the population modeling described in this chapter and its associated appendix, interpatient registrations were used to directly deform systematic and random displacement vector fields to and from the reference coordinate system. This method, as used in this work, only represents an approximation of the true vector transport. As the systematic and random displacement vectors are transported between the reference and patient planning images, the orientation and magnitude of these vectors must change as a function of the transformation from the reference to the new image space. Mapping vectors from the reference to the planning images should have been done using the pushforward, or differential of the interpatient transformation. The pushforward of the transformation $\mathbf{h}_{(i,0)\to ref}$ is denoted by $d\mathbf{h}_{(i,0)\to ref}$ and is a transformation from $\mathbf{R}^3 \to \mathbf{R}^3$. The pushforward is a linear map from the tangent space in the patient's planning image to the tangent space in the reference image, and is computed as the Jacobian of $\mathbf{h}_{(i,0)\to ref}$. In this thesis, the pushforward was ignored. Large differences in the results presented in this thesis due to this omission are not expected to be substantial, as the organ shapes, even between patients, did not vary greatly. In all future work, the pushforward will be utilized to transform the systematic and random vectors.

The population models created in this chapter have several possible clinical applications. One apparent application is their potential use in PTP. The work of Xu[63] simulated random organ motion, but assumed a known patient-specific systematic error for each patient in their implementation of COP. This work could be extended to include simulated systematic error as well, as each patient's systematic error is unknown before treatment.

A more straightforward application of the PCA population models to patient planning is described in the following chapter. This method involves using the organ occupancy maps calculated above to create anisotropic PTVs. The organ occupancy maps can be thresholded to ensure a certain level (for example, 95%) of target coverage. The dosimetric impact of planning on the PCA-based PTVs for bony- and centroid-aligned patients will be the focus of the next chapter.

4. Clinical application of a population statistical model of prostate cancer anatomical motion

4.1. Introduction

The previous chapter centered on the creation and validation of systematic and random tissue deformation PCA statistical models for a population of male pelvic patients. In this chapter, the systematic and random tissue deformation statistical models will be referred to jointly as the "population PCA model." The ultimate value of any such model is its ability to deliver a better radiation therapy plan to the patient. In this context, a better plan is one that is more likely to improve tumor control and/or reduce normal tissue toxicity when compared to the current standard of practice. In this work, physical doses to the CTV and OARs were used as surrogates for these outcomes. There are numerous ways to apply the population PCA model clinically. One of the more intriguing possibilities is to incorporate it into probabilistic planning. Probabilistic planning could theoretically incorporate the geometrical uncertainty as quantified by the PCA model directly into the optimization process. The goal would be to find the optimal plan to best safeguard against dosimetric errors introduced by the deforming anatomy.

In this study, a simpler clinical application of the population PCA model was tested. The model was used to create "smarter" margins around a patient's prostate, as contoured on the planning image. These margins were calculated from the model by

determining the magnitude, direction, and likelihood of a given prostate deformation. These margins have the ability to be anisotropic, meaning that the thickness can vary as a function of location on the prostate. This allows for a more liberal margin in areas where a high magnitude of deformation is likely and a more conservative one in areas where deformation is less likely.

This population PCA model-generated PTV was compared to a pseudo-uniform margin, which is typically used currently in prostate treatments. The comparison was done using the VCT framework. Two plans created from two different PTVs were applied to the daily anatomies of an entire fractionation scheme. The hypothesis was that using anisotropic margins derived from the population PCA model would provide, on average, plans with an improved therapeutic ratio compared to the current standard of treatment. Information from the model regarding the deformations of the bladder and rectum was not used in the planning process.

4.2. Methods and materials

4.2.1. Planning data

The dataset used in this study was synthetically derived from the individual PCA model, as described in Chapter 2. For each of the 19 NKI patients described previously, the DVFs mapping the fractional images to the planning images were used to create an individual PCA model. Forty-three synthetic deformations were sampled from each model, representing unique anatomies for an entire radiation fractionation regimen. The resultant DVFs were then used to deform the patient's planning contours, creating a sequence of 43 synthetic prostate, bladder, and the rectal anatomies.

Together, these 43 synthetic anatomies represented the patient's daily anatomies over a whole therapy course.

4.2.2. VCT subtrials

The VCT in this project had two subtrials, each comparing two arms. The two arms of each subtrial comprised two setup strategies: an online bony-alignment IGRT technique and an online prostate centroid-alignment IGRT technique. The centroid-alignment method is similar to the online procedure presented by Smitsmans, in which the prostate rigid alignment to the planning prostate anatomy is computed from the grayscale values of daily CBCTs.[64,65] For each setup strategy, two arms were compared: a plan using population PCA model-based anisotropic margin and a plan using a current standard planning technique. The first subtrial tested a bony-aligned population PCA model-based PTV ($\mathrm{PTV}_{PCA}^{bone}$) against a PTV created using the van Herk margin recipe (PTV_{vH}). The second subtrial tested a centroid-aligned population PCA model-based PTV ($\mathrm{PTV}_{PCA}^{cent}$) against a PTV ($\mathrm{PTV}_{cl}$) created with the margin used in our clinic at VCU. For each subtrial and arm, an IMRT plan was created using the patient's planning image. The planning image was a real patient (not synthetically derived) image, with physician-drawn contours. Dose invariance was assumed, meaning the dose distribution in the accelerator coordinate system for a given fluence profile does not vary with changes in the patient's anatomy.[66] This assumption greatly speeds up the computation time needed for the VCT, as the dose distribution calculated on the planning image was overlaid on each daily synthetic geometry. This assumption has been shown to introduce dose calculation errors of <2% in IMRT plans.[66] The dose was

then accumulated on the planning image using the known, synthetically sampled DVFs. DVH metrics were calculated for each patient's synthetic treatment course, and these were averaged over all patients.

The second arm for each subtrial will hereafter be referred to as the "traditional plan." The PTV for these plans was taken by using a semi-uniform margin to expand the physician-drawn planning GTV (which is taken to be the prostate only). The margin for these plans was calculated differently for the two subtrials, each described in detail below. The differences between the two are fully described in Appendix B.

4.2.2.2. Bony-aligned traditional plan

For the bony-aligned construction of the traditional PTV, the classic van Herk margin formula was used to construct a margin in the left/right, anterior/posterior, and superior/inferior directions. Using manually drawn prostate contours on each bony-aligned fractional image for each patient, the prostate centroids were computed and recorded. The systematic and random errors (Σ and σ) of the centroid shifts were calculated and used as input to the van Herk formula, given below.

$$\text{Margin} = 2.5\Sigma + 0.7\sigma \tag{14}$$

The values for Σ and σ are given in Table 4, as well as the margin expansion. These were used to create the PTV_{vH} in the bony-aligned subtrial of the VCT.

Table 4: The calculated values for Σ, σ, and the van Herk margin for the NKI dataset used in this study.

	LR (mm)	AP (mm)	SI (mm)
Σ	0.5	2.6	2.0
σ	1.0	2.5	2.4
van Herk Margin	2.1	8.4	6.7

Abbreviations: LR=left/right, AP=anterior/posterior, SI=superior/inferior.

4.2.2.2. Bony-aligned plan based on PCA model

The population PCA models of bony-aligned patients for systematic and random errors were used to sample a synthetic systematic and a random error in a reference coordinate system. To avoid biasing the VCT, the PCA models were created using only data from other patients. For example, only systematic error DVFs from patients 2-19 were used in the model used in the creation of the $\mathrm{PTV}_{PCA}^{bone}$ for the first patient. The sampled systematic and random errors were then added to create a synthetic deformation. This deformation was transported to the patient's local coordinate system using inter-patient DIR. The synthetic deformation, now in the patient's local coordinate system, was used to deform the patient's prostate planning contour. This deformed contour represented a realization of one possible instance of the patient's daily prostate. This process was repeated (456 times in total) in order to create an organ occupancy diagram of the prostate overlaid on the planning image. The $\mathrm{PTV}_{PCA}^{bone}$ was taken to be the volume that encapsulated 95% of all possible deformations. As coverage followed a Bernoulli distribution, 456 samples were calculated; this number corresponded to a 95% confidence interval that the target coverage would be ±2% of the intended threshold. A flowchart of the bony-aligned VCT subtrial is given in Figure *6*.

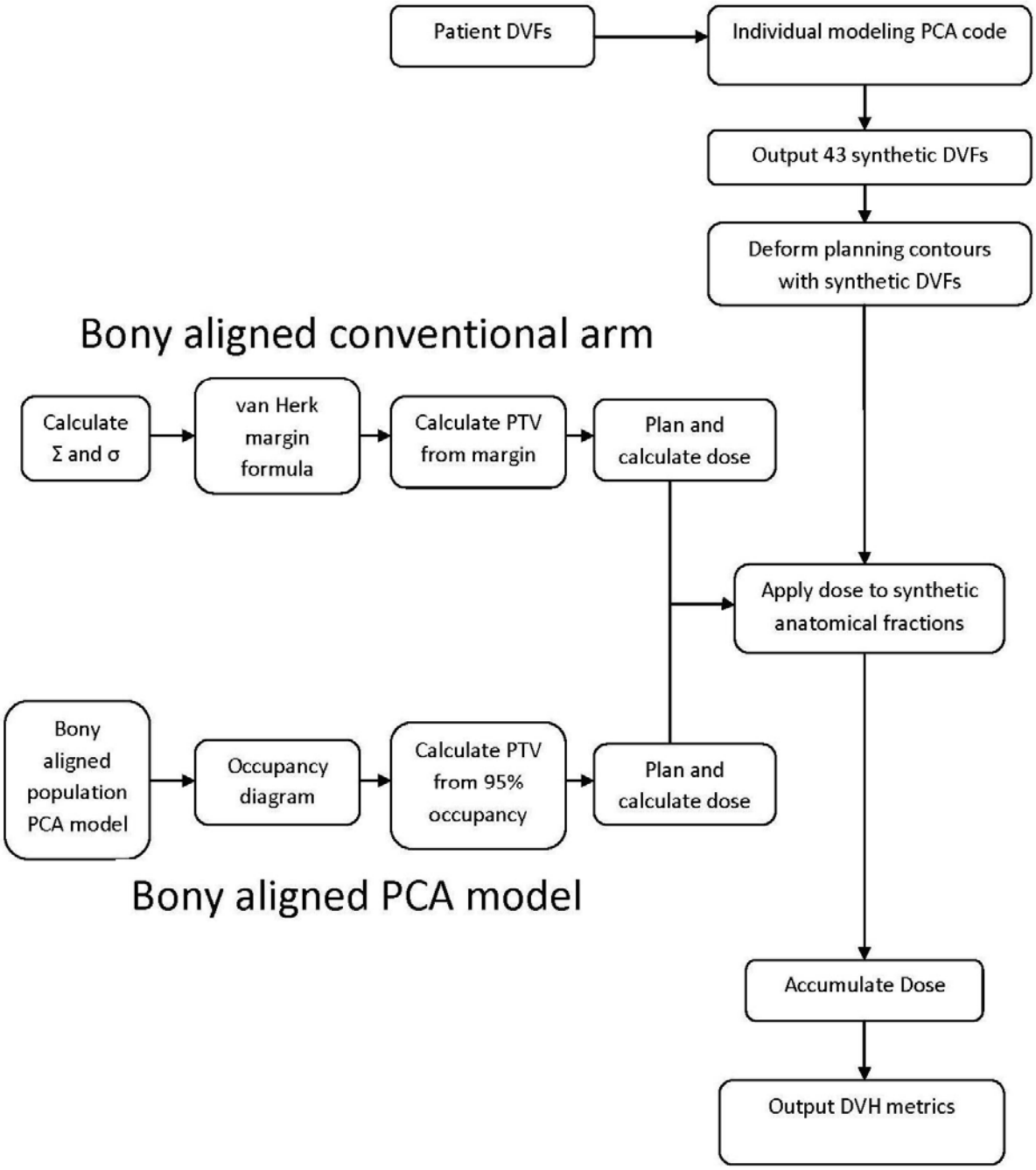

***Figure 6*: Flowchart showing the VCT process for the bony-aligned subtrial.**

4.2.2.3. Centroid-aligned traditional plan

The second subtrial had the patient aligned daily on the prostate centroid. The daily anatomies were created in the same manner as the bony setup, but with the extra step of the aligning the image on the prostate centroid each day. Only translation of the patient was considered.

For the centroid-aligned traditional plan, the PTV_{cl} was chosen to be a clinically popular 5 mm margin expansion in all directions except posteriorly, where a 3 mm expansion was used in an effort to spare the rectum from unnecessary dose. In a study led by Wen, the authors concluded that this margin is a good choice in IMRT plans, as judged by a superior complication-free tumor control probability (P+) when compared to margins of 10 mm/6 mm posteriorly and a 3 mm uniform margin.[67]

4.2.2.4. Centroid-aligned plan based on PCA model

The $\mathrm{PTV}_{PCA}^{cent}$ was determined in a manner very similar to that described in Section 4.2.2.2., with the difference being in how the population PCA model was created. The prostate centroid was used to align each patient's fractional images to his planning image. After this initial alignment, the DVFs associated with these two images, $\mathbf{u}_{(i,k)\to(i,0)}\left(\mathbf{x}_{i,0}\right)$, were calculated. From this point, the patient-specific systematic and random errors were calculated as described in Chapter 2, and the centroid-aligned population PCA model was created using the methods outlined in Chapter 3. A flowchart for the centroid-aligned subtrial is given in Figure 7.

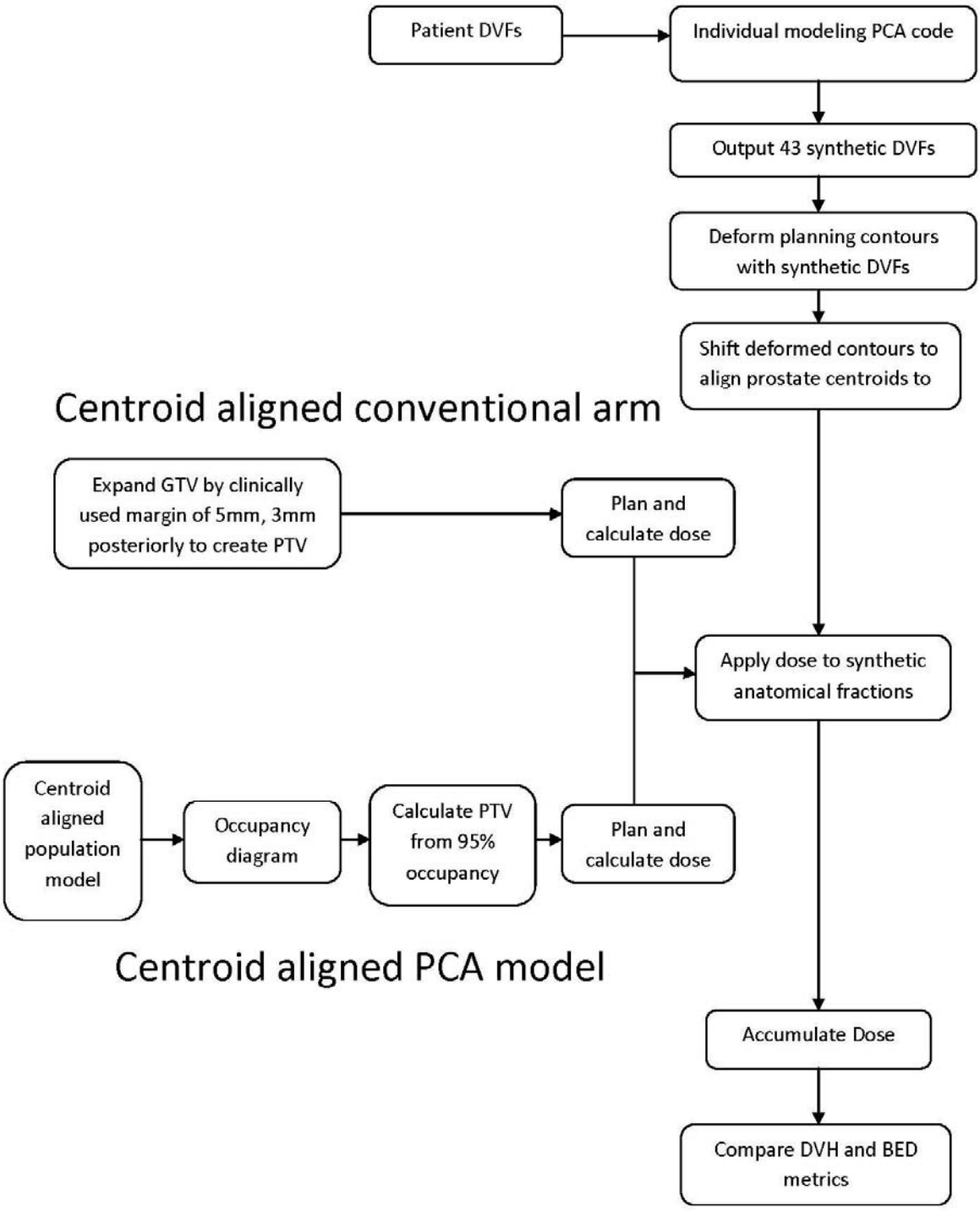

***Figure 7*: Flowchart outlining the VCT process for the centroid-aligned based subtrial.**

4.2.3. Planning setup and objectives

For each trial arm of each subtrial, seven 6 MV beams were used to create an IMRT plan. The beam angles used were 30°, 80°, 130°, 180° (posterior), 230°, 280°, and 330°, with the isocenter set to the PTV centroid in the planning image. The planning objective criteria (Table 5) were identical. Each patient had a prescription dose to the arm-specific PTV of 86 Gy over 43 fractions. This prescription was designed after the dose-escalation planning protocol of Memorial Sloan Kettering.[68,69] OAR dose volume objectives were selected to achieve the minimal dose to the OARs while still providing target coverage. Universal dose objectives are impossible to determine for every patient, as some patients present with more favorable anatomies than do others. In IMRT planning, the optimizer stops once it has met all objectives; however, this may not be the optimal plan, as normal tissue doses may have been able to be lowered beyond the planning objectives. To solve this problem and to guide the optimizer to achieve maximum therapeutic ratio, the bladder and rectum included generalized equivalent uniform dose (gEUD) as well as conventional DVH objectives. gEUD is the dose, which if uniformly delivered, gives the same radiobiological effect as the inhomogeneous dose of interest.[70,71] The equation for gEUD is as follows:

$$gEUD = \left(\sum_j v_j D_j^a \right)^{1/a} \tag{15}$$

where v_j is the volume of the dose volume bin with dose D_j, and a is a tissue dose-response parameter. For healthy tissues, a is a positive number. In this work, an extra planning objective was set for the bladder and rectum, calling for a maximum gEUD = 0 Gy ($a = 4$). This objective can never be achieved while still meeting PTV objectives, but

it is useful in driving down doses to bladder and rectum below their DVH objectives. To ensure that OAR dose reduction was not achieved at the expense of PTV coverage, a very low weight (w=1×10^{-6}) was used for the gEUD objectives. The OARs used in the optimization were those manually contoured on the patient's planning image. All planning and dose calculations were done using Pinnacle treatment planning system (v9.1, Philips Medical Systems). The maximum number of iterations used in the optimization process was set to 50. In addition to the OAR gEUD objectives, the DVH planning objectives in Table 5 were used for plan optimization.

Table 5: Planning objectives for use in IMRT beam optimization.

Organ	Dose Criteria
PTV	D_{97}≥86 [constrain], D_2≤90.7 [80]
Bladder	D_{70}≤19.8 [50], D_{50}≤38.7 [25], D_{30}≤61.9 [25], D_{20}≤69.7 [15], D_{14}≤74 [15], D_9≤79.1 [15], D_2≤89.4 [15] , EUD_{max}=0 [a=4, w=1×10^{-6}]
Rectum	D_{50}≤38.7 [50], D_{30}≤55.5 [25], D_{20}≤69.7 [15], D_5≤74.8 [50], D_2≤82.6 [50], D_{max}=84.3 [50], EUD_{max}=0 [a=4, w=1×10^{-6}]
Femur	D_1≤54.6 [10]
Ring Structure	D_{max}=75.3 [1]

All doses are in Gy, with the objective weights in brackets.

4.2.4. Dose accumulation

Dose accumulation was done using in-house bio-dose accumulator software within the research computing framework (RCF), described by Fatyga *et al*.[72] For each patient, the dose accumulator reads in the sequence of Pinnacle computed dose

distributions (one for each interfraction instance of anatomy), the planning image and its contours, and the corresponding sequence of 43 synthetic DVFs. These DVFs represent the daily anatomies of the patient throughout the whole treatment course. The dose (which is assumed invariant), was then mapped to the planning image by each DVF and accumulated for the prostate, bladder, and rectum, creating a DVH for each of the three organs. The D_{90}, D_{95}, and D_{97} were reported for the prostate, and the D_{50}, D_{30}, D_{20}, and D_5 were reported for the bladder and rectum. The differences in these metrics were compared between the two planning arms. Hypothesis testing was performed in order to assess the significance ($p<0.05$) of the differences between the DVH metrics for each arm. For this purpose, a paired t-test was used.

4.3. Results

4.3.1. $\mathbf{PTV}_{\mathbf{PCA}}^{\mathbf{bone}}$ and $\mathbf{PTV}_{\mathbf{vH}}$ comparison

For every patient, the volume of $\mathrm{PTV}_{PCA}^{bone}$ was smaller than its corresponding PTV_{vH}. Across all patients, there was a mean 15.7% (range 10.3 – 23.2%) reduction in volume size. This reduction in volume is a promising but not definitive indicator of possible OAR tissue sparing, as this metric gives no information on which areas of the PTV were being trimmed. A visualization of the direct comparison between the two PTV expansions versus location is given in Figure 8 for a sample patient. Only one patient is shown, as the magnitudes and patterns are similar between all patients. Here, a colormap representing the PTV margin is overlaid on the manually drawn planning contour of the prostate. In the area adjacent to the bladder (anterior to the prostate), the PCA model yields a margin reduction compared to van Herk of 2-3 mm and smaller

reduction in the left and right directions. However, a substantial (~4 mm) increase in the margin is suggested by the PCA model in the area adjacent to the rectum. The dosimetric effect of this increased margin was investigated.

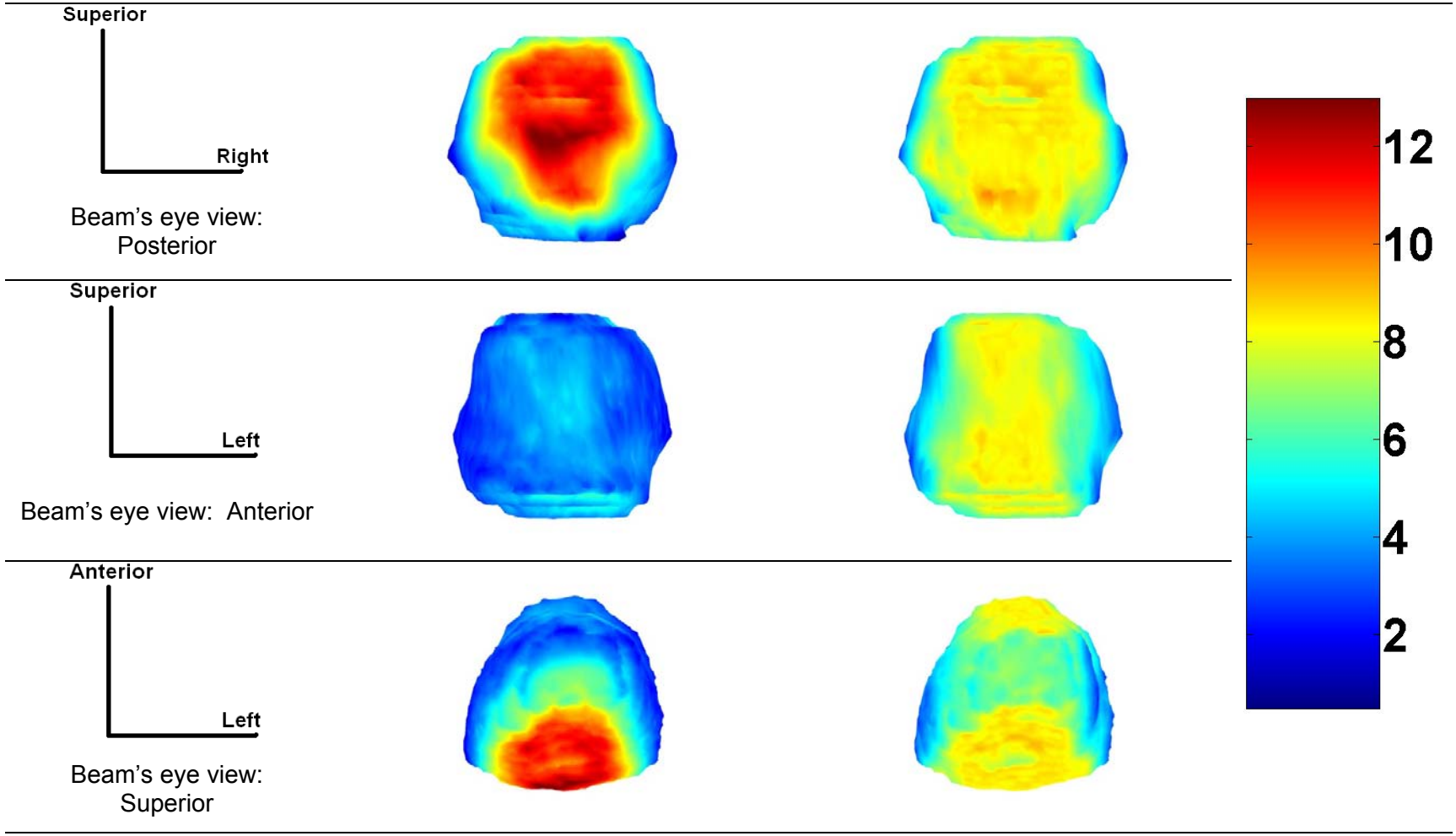

***Figure 8*: Distance to PTV expansion maps for a sample bony-aligned patient for three different orientations from a beam's eye view perspective. The shape is that of the physician-drawn prostate where the color represents the distance to the closest point (distance in mm) for the two different PTV expansions, PTV_{PCA}^{bone} and PTV_{vH}. PTV_{PCA}^{bone} offers smaller margins in all locations except against the rectum (top row), where they can be as large as 13 mm.**

4.3.2. VCT results for bony setup subtrial

The DVHs for three patients are given in Figure 9. These three patients represent three possible outcomes: one in which the PCA plan is superior, one in which the van Herk plan is superior, and one in which they are comparable. In order to determine any possible benefit for the population of the patients, DVH metrics were extracted for each patient. The means and standard deviations are presented in Table 6. The PCA and van Herk plans each delivered the prescription dose of at least 86 Gy to 97% of the prostate. The differences in prostate dose delivery were statistically insignificant, suggesting that the PCA posterior margin was unnecessarily large, while the van Herk margin was too large in all other directions. Across the patient population, the PCA plan delivered significantly less dose to the D_{30} ($p = 7.96 \times 10^{-4}$), D_{20} ($p = 4.78 \times 10^{-5}$), and D_5 ($p = 3.45 \times 10^{-3}$) of the bladder (mean reduction of 1.9, 2.7, and 1.2 Gy, respectively). For the rectum, the relationship was more complicated. The rectal dose differences between the two plans were deemed significant for the D_{50} ($p = 0.0230$), D_{20} ($p = 7.51 \times 10^{-5}$), and D_5 ($p = 8.03 \times 10^{-6}$). On average, the rectum D_{50} for the PCA plan was lower by 1.0 Gy, but this plan provided higher doses to the D_{20} and D_5 (2.6, and 2.3 Gy, respectively). This implies that the PCA plan is less effective in reducing the high doses to small subvolumes of the rectum, yet it may help limit lower doses to larger portions of the rectum. On a patient-by-patient basis, the DVH metrics investigated are plotted for the prostate, bladder, and rectum in Figure 10. For the bony-aligned setup, the “better” plan is not easily determined. Using the PCA plan

represents a tradeoff between lowering the dose to the bladder and giving higher dose to portions of the rectum.

a.)

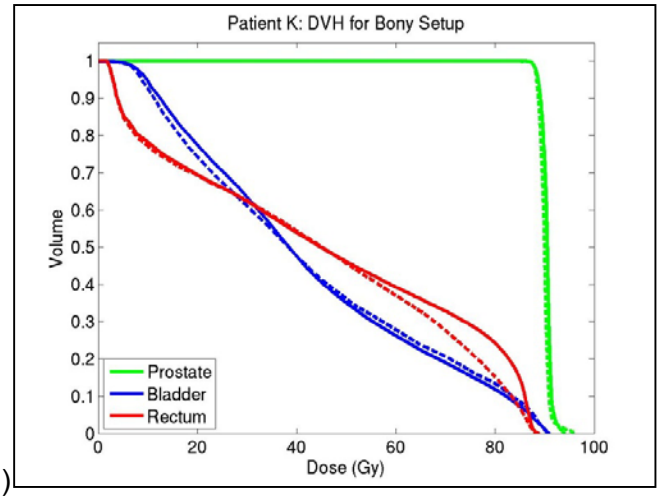

b.)

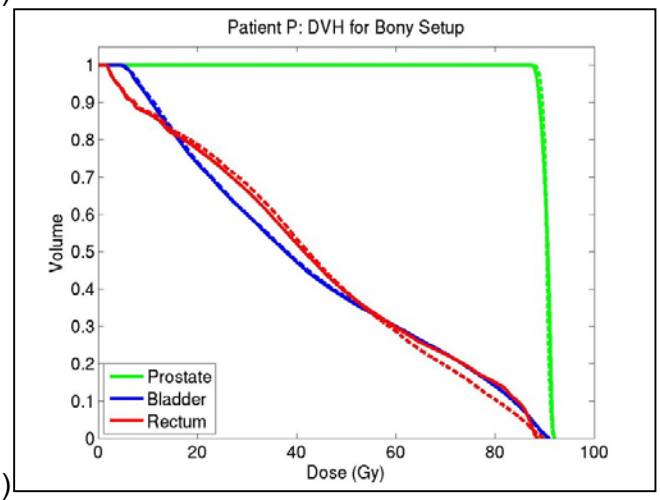

c.)

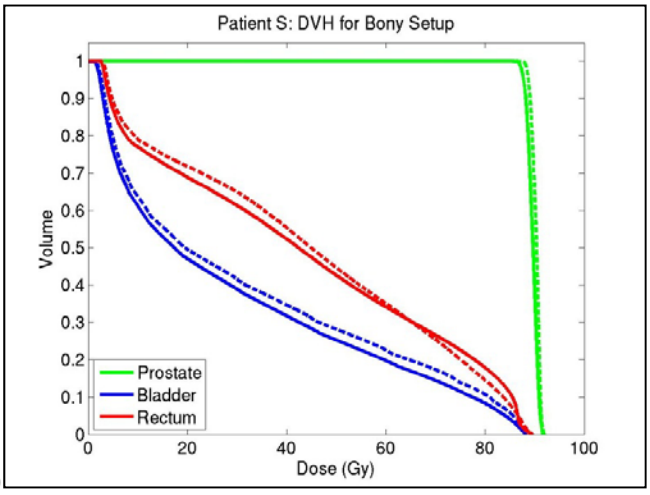

Figure 9: **Example DVHs for three patients in the bony-aligned VCT subtrial. Dashed lines represent plans using PTV_{vH} while solid lines represent plans using $\mathrm{PTV}_{PCA}^{bone}$. Curves are given for the prostate (green), bladder (blue), and the rectum (red). Image a) represents an instance where the van Herk base plan gives a resultant plan that is better than the PCA based plan. Image b) shows a plan where the plans are comparable. Image c) shows an instance where the PCA plan is deemed better.**

Table 6: The mean and standard deviation of selected DVH metrics in the prostate, bladder and rectum over all 19 patients in the bony-aligned setup. The right-hand column gives the difference of the mean doses. A negative difference indicates a mean dose reduction in plans created using $\mathrm{PTV}_{PCA}^{bone}$.

	DVH Metric	Mean PCA Dose (Gy)	Mean Traditional Dose (Gy)	Mean PCA Dose - Traditional Dose (Gy)	p-value
Prostate	D_{97}	86.7±2.1	86.3±2.9	0.4	0.130
	D_{95}	87.4±1.6	87.1±2.3	0.3	0.408
	D_{90}	88.1±1.2	88.0±1.6	0.1	0.532
Bladder	D_{50}	26.7±15.4	27.5±15.9	-0.8	0.0881
	D_{30}	47.9±16.7	49.8±16.9	-1.9	7.96×10^{-4}
	D_{20}	63.1±14.5	65.8±13.4	-2.7	4.78×10^{-5}
	D_5	85.6±3.5	86.8±2.6	-1.2	3.45×10^{-3}
Rectum	D_{50}	36.0±9.2	37.0±8.5	-1.0	0.0230
	D_{30}	56.0±7.4	55.0±7.0	1.0	0.0604
	D_{20}	66.8±8.5	64.2±8.1	2.6	7.51×10^{-5}
	D_5	82.6±4.6	80.3±5.7	2.3	8.03×10^{-6}

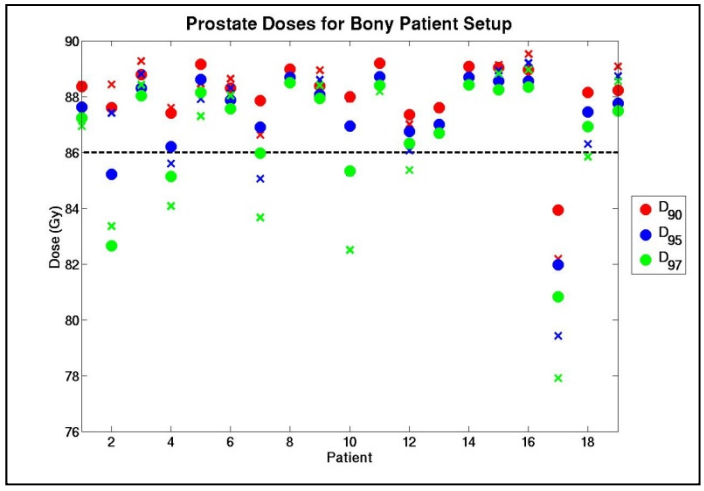

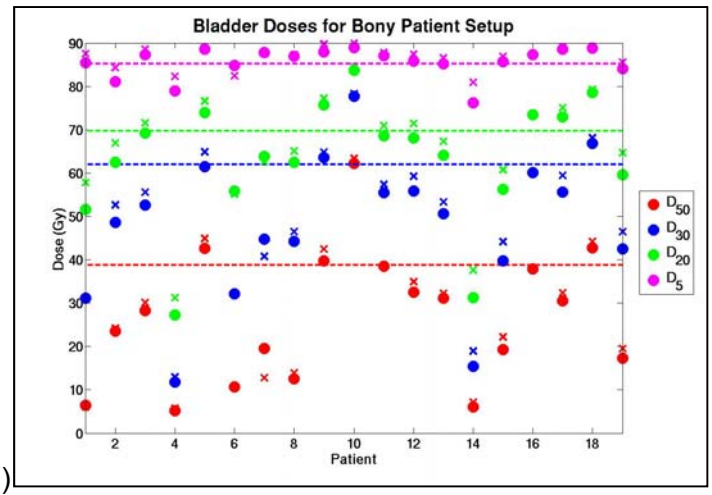

a.)

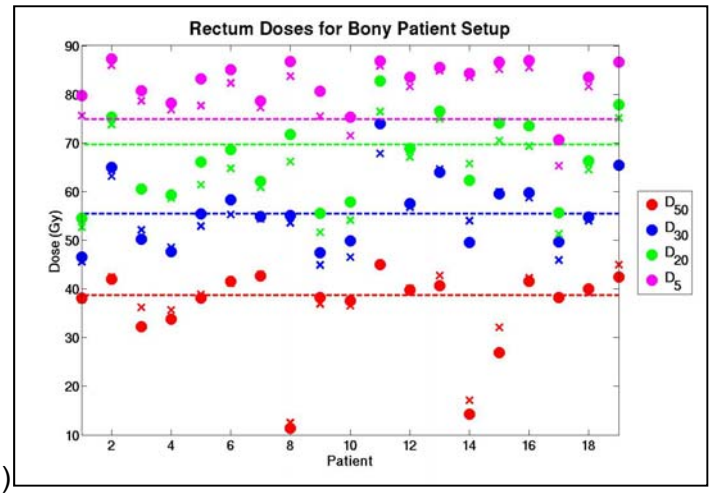

b.)

***Figure 10*: Several DVH metrics for the prostate (top), bladder (middle) and rectum (bottom) for the bony-aligned setup. The PCA based plan doses are the solid dots while the doses from the van Herk based plan are represented with an x. The dashed horizontal lines show the planning criteria used with the associated DVH metric.**

4.3.3. $\mathbf{PTV}_{\mathbf{PCA}}^{\mathbf{cent}}$ and $\mathbf{PTV}_{\mathbf{cl}}$ comparison

Similar to the bony-aligned setup, the volume of $\mathrm{PTV}_{PCA}^{cent}$ was smaller than the PTV_{cl} for every patient. The mean reduction in volume size was 27.1% (range 20.8 – 37.4%). A visualization of the direct comparison between the two PTV expansions versus location is given in Figure 11 for a sample patient. Also similar to the bony setup, the margin to create $\mathrm{PTV}_{PCA}^{cent}$ is smaller than the margin for PTV_{cl} in every direction with the exception of posteriorly (adjacent to the rectum). This effect was not as pronounced, however, in this scenario.

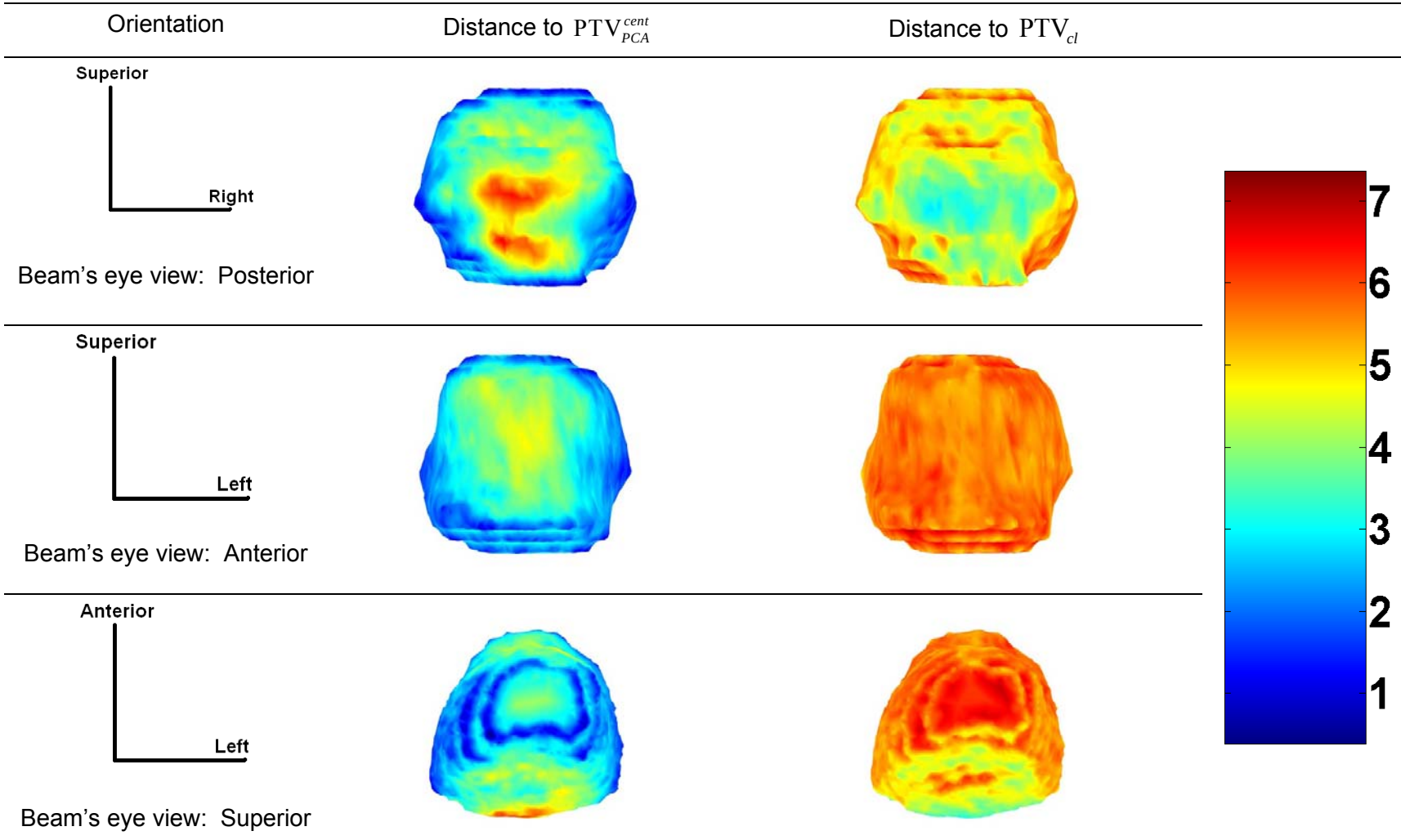

***Figure 11*: Distance to PTV expansion maps for a sample centroid-aligned patient for three different orientations from a beam's eye view perspective. The shape is that of the physician drawn prostate where the color represents the distance to the closest point (distance in mm) for the two different PTV expansions, PTV_{PCA}^{cent} and PTV_{cl}.**

4.3.4. VCT results for centroid-aligned setup subtrial

The DVHs for the same three patients as in the bony-aligned setup are given in Figure 12, this time aligned on the prostate centroid. The population mean and standard deviation of selected DVH metrics are presented in Table 7. Similar to the bony-aligned setup, both centroid-aligned plans delivered, on average, the prescription dose to 97% of the prostate. While both provided acceptable target coverage, the PCA plan significantly reduced the dose on average to both the bladder and the rectum for the DVH metrics investigated; the lone exception was D_5 to the rectum. Here, no significant difference was found between the two plans. The p-values are given in Table 7. On a patient-by-patient basis, the four DVH metrics investigated are plotted for the prostate, bladder, and rectum in Figure 13.

(a.)

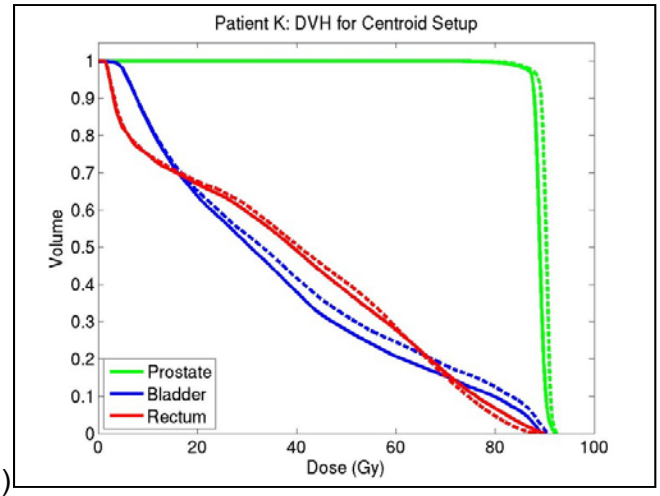

(b.)

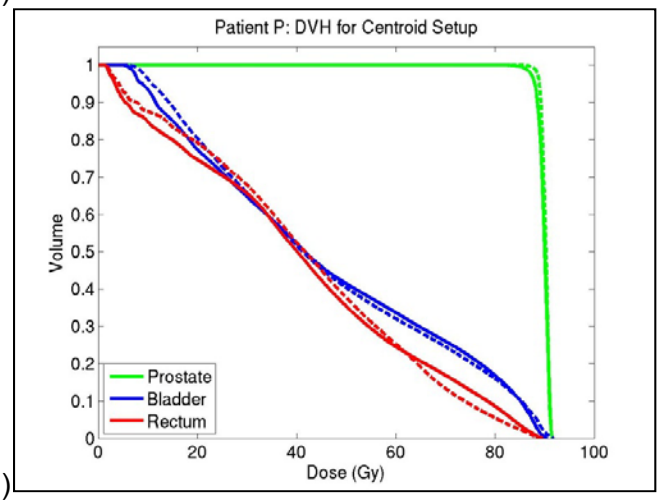

(c.)

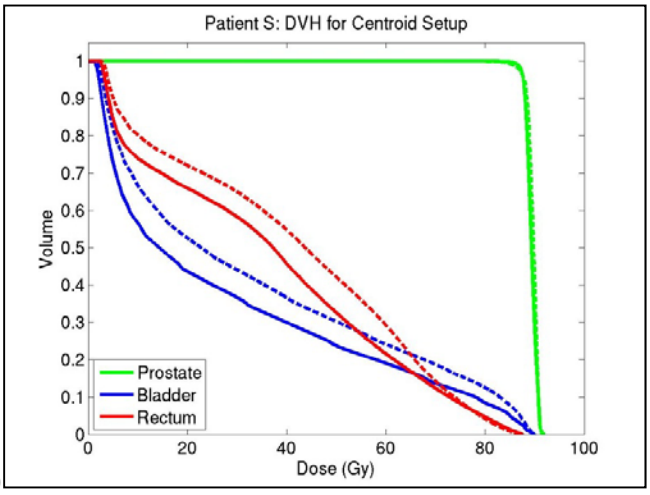

***Figure 12*: Example DVHs for three patients in the centroid-aligned VCT subtrial. Dashed lines represent plans using PTV_{cl} while solid lines represent plans using $\mathrm{PTV}_{PCA}^{cent}$. Curves are given for the prostate (green), bladder (blue), and the rectum (red). Image (a) represents an instance where the PCA based plan provides less dose coverage to the prostate. Image (b) shows a plan where the plans are comparable. Image (c) shows an instance where the PCA plan is deemed better.**

Table 7: The mean and standard deviation of selected DVH metrics in the prostate, bladder, and rectum over all 19 patients in the centroid-aligned setup. The right-hand column gives the difference of the mean doses. A negative difference indicates a mean dose reduction in plans created using $\mathrm{PTV}_{PCA}^{cent}$.

	DVH Metric	Mean PCA Dose (Gy)	Mean Traditional Dose (Gy)	Mean PCA Dose - Traditional Dose (Gy)	p-value
Prostate	D_{97}	87.0±1.1	87.4±1.2	-0.4	0.0956
	D_{95}	87.4±0.9	88.0±0.8	-0.6	0.0323
	D_{90}	88.1±0.7	88.6±0.6	-0.5	0.0117
Bladder	D_{50}	20.7±13.0	24.0±12.8	-3.3	2.93×10^{-3}
	D_{30}	40.0±15.5	45.4±15.0	-5.4	5.81×10^{-4}
	D_{20}	54.8±15.1	61.6±13.5	-6.8	6.22×10^{-5}
	D_5	83.2±5.1	86.1±3.0	-2.9	1.40×10^{-4}
Rectum	D_{50}	34.0±9.7	37.5±8.3	-3.5	8.84×10^{-4}
	D_{30}	50.4±5.8	53.2±4.5	-2.8	1.13×10^{-4}
	D_{20}	59.2±6.2	61.0±4.4	-1.8	3.90×10^{-3}
	D_5	78.0±3.7	77.9±2.8	0.1	0.710

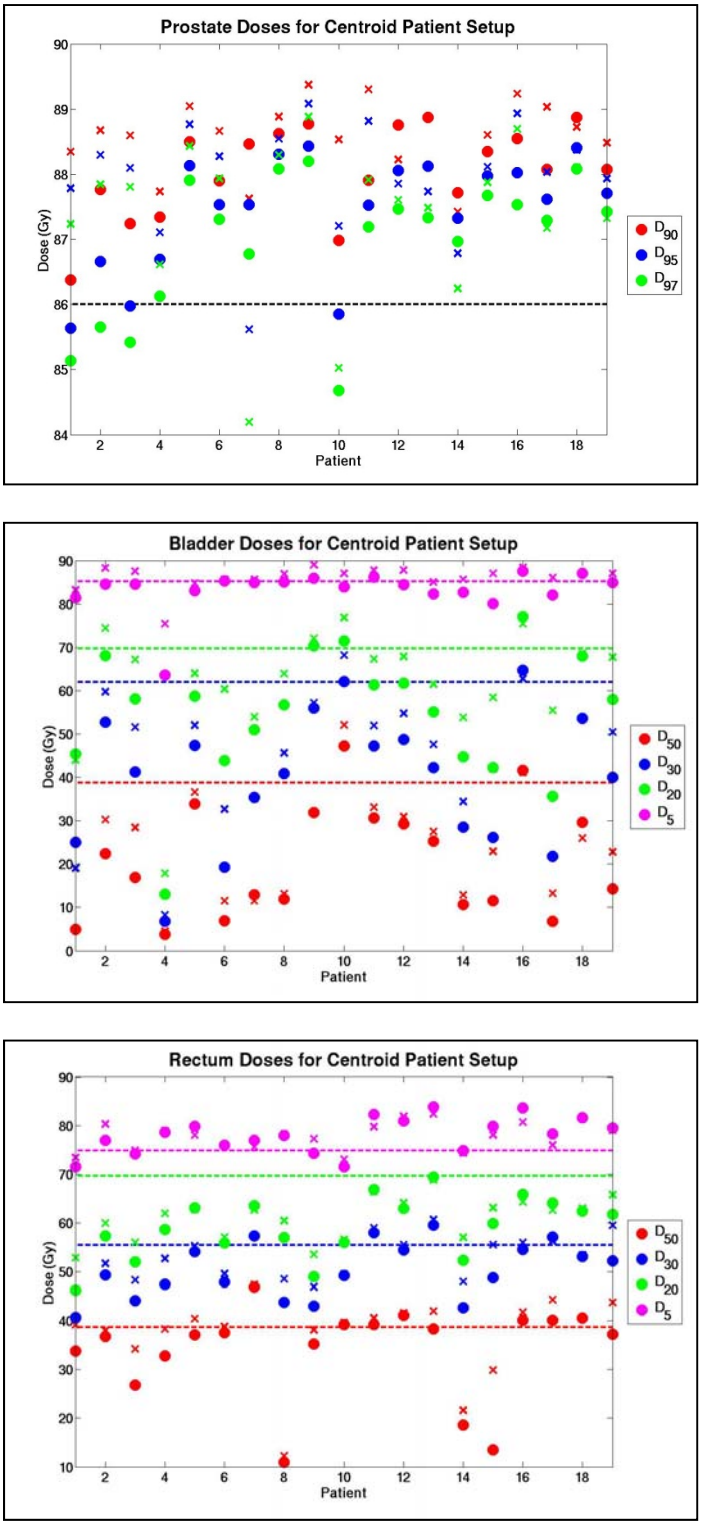

Figure 13: **DVH metrics for the prostate (top), bladder (middle) and rectum (bottom) for the centroid-aligned patient setup. The PCA based plan doses are the solid dots while the doses from the 3/5mm plan are represented with an x. The dashed horizontal lines show the planning criteria used with the associated DVH metric.**

4.4. Discussion

Results from the centroid-aligned VCT subtrial show that the PCA margin plan provides adequate prostate dose coverage while reducing the dose to the bladder and rectum for most (>75%) of the patients when compared to the plan based on the 5/3 mm margin. Importantly, applying the population PCA model to create a patient's PTV provides a systematic and reasoned method to determine margins for prostate contour-aligned patients. While the formulas of Stroom and van Herk provide this function for bony-aligned setup, their formulas cannot be applied to the centroid-aligned case. In clinical practice, the margins currently used for this patient population are created somewhat arbitrarily and vary widely between clinics. The method described in this thesis could potentially standardize the practice for margin creation across clinics.

While the results of the VCT were promising for the PCA-based plan in centroid-aligned patients, they were less so for patients aligned to bony anatomy. The $\mathrm{PTV}_{PCA}^{bone}$ was a smaller volume than PTV_{vH}, yet the PCA-based plan offered a modest but significant dose reduction for the bladder, while raising the dose to parts of the rectum. In the bony-aligned trial, the PCA based plan resulted in a higher D_5 in the rectum for all patients. This result is unsurprising, as the PCA model of bony-aligned patients requires a large (up to 13 mm) margin at the prostate/rectum interface, compared to the 8.4 mm margin computed from the van Herk formula. This difference in margin size did not compromise the CTV coverage, suggesting that the 95% coverage goal of the PCA margin is too strict. Future work will investigate the dosimetric effect of the more modest coverage goals of 90% and 80%. Another possible explanation for the posterior margin difference is that the van Herk formula indicates one margin for the posterior and

anterior directions. The PCA model shows the prostate having larger and more varying shifts posteriorly. An example of this variability at the rectum is shown in Figure 14. The pubic symphysis is anterior to the prostate, limiting the amount of motion allowed in that direction. The lack a motion in the anterior direction may reduce the formula-suggested margin in both the anterior and posterior directions. This would also explain why the PCA margin is smaller than the van Herk margin in the anterior direction.

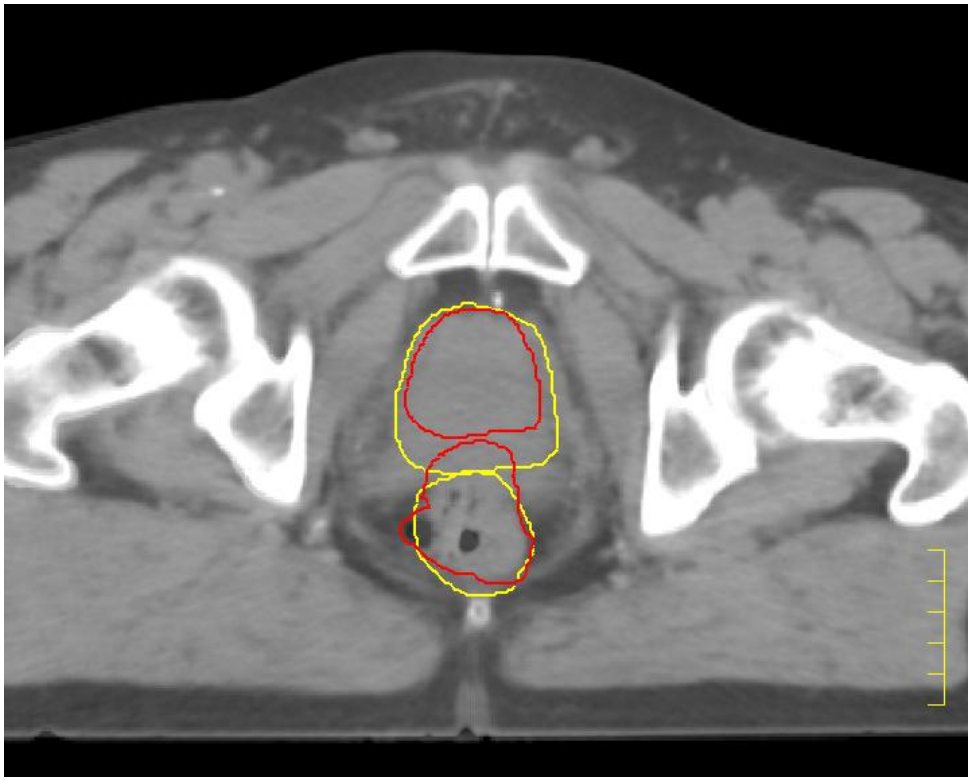

***Figure 14*: An example of the prostate's variability near the rectum interface for bony-aligned data. The planning contours for the prostate and rectum are shown in red while the yellow lines are the physician drawn contours on a treatment day. On this day, the rectum seems to be pushing the prostate against the pubic symphysis.**

This VCT represents a straightforward and simple approach to applying statistical modeling to the clinical process. The only criterion used to create the PTV was the 95%

probability of encompassing the prostate. Stroom and van Herk both used dose to the prostate as their final endpoint. It is possible that the margins could be further reduced if the dose falloff is taken into consideration. The work of Gordon *et al.* showed that the van Herk formula overestimated the necessary margin[73] and that this was due to the formula's assumption of a perfectly conformal target dose.[74] The validity of the PCA margin developed in this work similarly suffers from not accounting for the dose falloff.

In this VCT, information from the PCA model on the motion of the bladder and rectum was ignored. A similar method of thresholding the prostate occupancy diagram could be extended to the OARs to create a planning organ at risk volume (PRV). Due to the large amounts of deformation in the bladder and rectum, the 95% occupancy diagram will potentially create large PRVs, which could be unwieldy in the planning process. Further research must be done to determine a sufficient thresholding percentage. Planning objectives may also have to be updated to account for the larger planning volumes.

4.5. Conclusion

For two different modes of IGRT daily online setup, the VCT framework was used to compare the dosimetric differences between a PTV computed from a statistical model and a PTV commonly used in current clinical practice. For bony-aligned setup, there was no clear better method between the PCA- and van Herk-based plans for the 19 patients. For centroid-aligned setup, the PCA plan provided proper dose coverage to the prostate while reducing the dose to the bladder and rectum in most patients when compared with a semi-uniform margin of 5 mm (3 mm posteriorly).

5. Conclusion

5.1. Patient-specific PCA modeling

Chapter 2 outlined the use of the PCA technique in modeling the patient-specific random errors of patients undergoing fractionated definitive radiation therapy. By using the SICLE DIR algorithm, deformations over the entire image volume were modeled. Previously, only the shapes of select organs (prostate, bladder, and rectum) had been modeled. Use of PCA technique allows the patient's random error to be represented by a linear combination of eigenmodes and expansion coefficients. These expansion coefficients are statistically independent of one another, meaning the probability of a given random error is the same as the probability of selecting the associated set of expansion coefficients. To compute the expansion coefficient PDFs, KDE was used with a Gaussian kernel. The PDFs allow for the sampling of synthetic random error DVFs. To validate the model for all voxels lying within the three organs of interest, the distributions of vector displacements derived from the original sequence of training DVFs were compared to those derived from a much larger set of synthetic DVFs randomly sampled from the patient-specific PCA model. This was done for all patients, and no significant differences between the vector distributions were found in any voxel. Patient-specific modeling has potential applications in VCTs, allowing researchers to create a full fractionation scheme of realistic daily anatomies from a smaller dataset. An example of this model's use in probabilistic planning was also given.[63]

5.2. Population PCA modeling

In Chapter 3, the PCA technique was extended from patient-specific modeling to population modeling of the male pelvis. To do this, a common reference coordinate system was needed. In this thesis, I present one solution to the difficult problem of patient-to-patient registration, enabling the patient-specific systematic and random errors to be mapped to the common reference coordinate system. Due to the difficulty of interpatient DIR, the systematic and random errors were mapped separately for each organ (prostate, bladder, and rectum) and stitched together in the reference coordinate system. The inverse consistency error introduced by mapping patient's systematic and random errors to and from the reference coordinate system was determined to be ≤ 0.1 mm for most voxels within the three organs. The well-known parameters of Σ and σ, which are measurements of the systematic and random error distributions, were expanded to the 3D volume covering the entirety of the prostate, bladder, and rectum. These parameters were calculated for each organ voxel and for both bony-aligned and prostate centroid-aligned patient setups. The centroid-aligned setup showed smaller (~2.5x) systematic and random errors within the prostate when compared to bony alignment. The two setup approaches each had unique distributions of errors. Each setup showed smaller systematic and random errors near the alignment points (bony anatomy and prostate centroids).

PCA was used to successfully model the systematic and random errors in a population of prostate cancer patients. A population systematic and random model used data from a population of patients to describe the magnitude and likelihood of a given deformation. Separate models were created using the bony-aligned and prostate

centroid-aligned data. For all models, the PCA reconstruction error was calculated as the error introduced by using a limited number of eigenmodes (eigenmodes representing ≥ 95% of the overall variance). In the voxels within the prostate, the mean systematic and random errors were all near zero with standard deviations of ≤ 0.56 mm in all directions. In order to test the model's ability to represent systematic and random errors not included in the PCA training data, a leave-one-out study was performed. Each patient's systematic and random errors were reconstructed using a PCA model constructed from data exclusively from other patients. However, the standard deviation of the voxel differences between the PCA representations of the "left out" patient and the original systematic DVF was over 2 mm in the bladder anterior-posterior and left-right directions. These standard deviations were smaller for random errors, yet still over a millimeter in some directions. The larger errors in the systematic error leave-one-out study indicate that a larger dataset may be necessary to model all modes of systematic tissue motion. This work is the first time that both systematic and random tissue displacements have been modeled for the prostate patient population.

5.3. Clinical application of the population model

In Chapter 4, I used the population models described in Chapter 3 to create anisotropic PTV margins and tested their efficacy relative to conventional PTV margin recipes via a VCT framework. For both bony- and centroid-aligned setups, synthetic systematic and random prostate DVFs were sampled from their respective PCA models. These DVFs were then summed to create a synthetic random instance of deformed central pelvic anatomy. The interpatient registrations were used to transport each synthetic prostate DVF to the planning image of the patient and to deform the physician-

drawn planning contours. By averaging the set of bitmaps representing the synthetically deformed prostate contours, an organ occupancy map was eventually created. For each patient, a PCA-based PTV was created by thresholding the occupancy map at the 95% level. IMRT treatment plans using the PCA-based PTV were then compared to plans created using clinically used PTVs. For a bony-aligned setup, the clinically used PTV was created using the van Herk margin formula found in equation (14). For centroid-aligned setup, the clinically used PTV was created using a 5 mm (3 mm posterior) expansion. In bony-aligned setup, the PCA-based PTVs were found to give a mean 15.7% (range 10.3-23.2%) reduction in volume when compared with the van Herk margin PTV. For centroid-aligned setup, the mean volume reduction was 27.1% (range 20.8-37.4%). Plans were applied to a synthetically generated treatment course (using methods outlined in Chapter 1) for each of the 19 patients in the dataset. In the bony-aligned setup, the PCA- and van Herk-based margin plans each successfully delivered, on average, the prescription dose to at least 97% the target. The PCA margin plans exhibited significant decreases (0.8 - 2.7 Gy) in D_{50}, D_{30}, D_{20}, and D_5 to the bladder and the D_{50} to the rectum, while giving a significantly higher dose to the rectum D_{20} and D_5 (2.6 and 2.3 Gy, respectively). In the centroid-aligned setup, each plan, on average, delivered the prescription dose to at least 97% of the target while significantly decreasing (1.8 – 6.8 Gy) all DVH endpoints investigated for the bladder and rectum, with the exception of the rectum's D_5, where no significant difference was observed. No loss in target dose coverage was seen for any PTVs used in the VCT, implying that all were overly generous. This is believed to be caused by extended dose falloff in areas surrounding the CTV.

5.4. Summary

In summation, in this thesis, I outlined and validated a method for statistically modeling the organ motion of patients undergoing definitive radiation therapy. The modeling was performed on an individual basis and then expanded to model the organ motion of the patient population. A straightforward method was developed to apply the population modeling in radiation treatment planning to illustrate the clinical utility of population as wells as individual patient statistical PCA models. Using the VCT framework, mixed results were found comparing the dosimetric effects of the model based treatment planning compared to traditional treatment planning for patients aligned on bony anatomy. For the subtrial comparing clinically used and PCA-based PTVs for a simulated prostate centroid alignment, the dosimetric benefit of the PCA-based PTV margin was more pronounced.

References

[1.] Z. Su, L. S. Zhang, M. Murphy and J. Williamson,"Analysis of Prostate Patient Setup and Tracking Data: Potential Intervention Strategies," Int J Radiat Oncol **81** (3), 880-887 (2011).

[2.] K. R. Britton, Y. Takai, M. Mitsuya, K. Nemoto, Y. Ogawa and S. Yamada,"Evaluation of inter- and intrafraction organ motion during intensity modulated radiation therapy (IMRT) for localized prostate cancer measured by a newly developed on-board image-guided system," Radiat Med **23** (1), 14-24 (2005).

[3.] N. H. Haripotepornkul, S. K. Nath, D. Scanderbeg, C. Saenz and C. M. Yashar,"Evaluation of intra- and inter-fraction movement of the cervix during intensity modulated radiation therapy," Radiotherapy and Oncology **98** (3), 347-351 (2011).

[4.] J. L. Barker, A. S. Garden, K. K. Ang, J. C. O'Daniel, H. Wang, L. E. Court, W. H. Morrison, D. I. Rosenthal, K. S. C. Chao, S. L. Tucker, R. Mohan and L. Dong,"Quantification of volumetric and geometric changes occurring during fractionated radiotherapy for head-and-neck cancer using an integrated CT/linear accelerator system," Int J Radiat Oncol **59** (4), 960-970 (2004).

[5.] J. L. Robar, A. Day, J. Clancey, R. Kelly, M. Yewondwossen, H. Hollenhorst, M. Rajaraman and D. Wilke,"Spatial and dosimetric variability of organs at risk in head-and-neck intensity-modulated radiotherapy," Int J Radiat Oncol **68** (4), 1121-1130 (2007).

[6.] Q. W. Wu, Y. W. Chi, P. Y. Chen, D. J. Krauss, D. Yan and A. Martinez,"Adaptive Replanning Strategies Accounting for Shrinkage in Head and Neck Imrt," Int J Radiat Oncol **75** (3), 924-932 (2009).

[7.] P. H. Ahn, C. C. Chen, A. I. Ahn, L. Hong, P. G. Scripes, J. Shen, C. C. Lee, E. Miller, S. Kalnicki and M. K. Garg,"Adaptive Planning in Intensity-Modulated Radiation Therapy for Head and Neck Cancers: Single-Institution Experience and Clinical Implications," Int J Radiat Oncol **80** (3), 677-685 (2011).

[8.] M. Ghilezan, D. Yan, J. Liang, D. Jaffray, J. Wong and A. Martinez,"Online image-guided intensity-modulated radiotherapy for prostate cancer: How much improvement can we expect? A theoretical assessment of clinical benefits and potential dose escalation by improving precision and accuracy of radiation delivery," Int J Radiat Oncol Biol Phys **60** (5), 1602-1610 (2004).

[9.] Y. Lei and Q. W. Wu,"A hybrid strategy of offline adaptive planning and online image guidance for prostate cancer radiotherapy," Physics in Medicine and Biology **55** (8), 2221-2234 (2010).

[10.] H. Liu and Q. W. Wu,"Dosimetric and geometric evaluation of a hybrid strategy of offline adaptive planning and online image guidance for prostate cancer radiotherapy," Physics in Medicine and Biology **56** (15), 5045-5062 (2011).

[11.] Q. J. Wu, D. Thongphiew, Z. Wang, B. Mathayomchan, V. Chankong, S. Yoo, W. R. Lee and F. F. Yin,"On-line re-optimization of prostate IMRT plans for adaptive radiation therapy," Physics in Medicine and Biology **53** (3), 673-691 (2008).

[12.] T. G. Purdie, J. P. Bissonnette, K. Franks, A. Bezjak, D. Payne, F. Sie, M. B. Sharpe and D. A. Jaffray,"Cone-beam computed tomography for on-line image guidance of lung

stereotactic radiotherapy: Localization, verification, and intrafraction tumor position," Int J Radiat Oncol **68** (1), 243-252 (2007).
[13] J. R. Wong, L. Grimm, M. Uematsu, R. Oren, C. W. Cheng, S. Merrick and P. Schiff,"Image-guided radiotherapy for prostate cancer by CT-linear accelerator combination: Prostate movements and dosimetric considerations," Int J Radiat Oncol **61** (2), 561-569 (2005).
[14] D. Schulze, J. Liang, D. Yana and T. Z. Zhang,"Comparison of various online IGRT strategies: The benefits of online treatment plan re-optimization," Radiotherapy and Oncology **90** (3), 367-376 (2009).
[15] *ICRU Report 50. Prescribing, Recording and Reporting Photon Beam Therapy.* (International Commission on Radiation Units and Measurements, Bethesda, MD, 1993).
[16] A. R. Padhani, V. S. Khoo, J. Suckling, J. E. Husband, M. O. Leach and D. P. Dearnaley,"Evaluating the effect of rectal distension and rectal movement on prostate gland position using cine MRI," Int J Radiat Oncol **44** (3), 525-533 (1999).
[17] J. C. Roeske, J. D. Forman, C. F. Mesina, T. He, C. A. Pelizzari, E. Fontenla, S. Vijayakumar and G. T. Y. Chen,"Evaluation of changes in the size and location of the prostate, seminal vesicles, bladder, and rectum during a course of external beam radiation therapy," Int J Radiat Oncol **33** (5), 1321-1329 (1995).
[18] NCCN,"Prostate Cancer,"http://www.nccn.org/professionals/physician_gls/pdf/prostate.pdf, Accessed on June 13, 2014
[19] A. L. Zietman, K. Bae, J. D. Slater, W. U. Shipley, J. A. Efstathiou, J. J. Coen, D. A. Bush, M. Lunt, D. Y. Spiegel, R. Skowronski, B. R. Jabola and C. J. Rossi,"Randomized Trial Comparing Conventional-Dose With High-Dose Conformal Radiation Therapy in Early-Stage Adenocarcinoma of the Prostate: Long-Term Results From Proton Radiation Oncology Group/American College of Radiology 95-09," J Clin Oncol **28** (7), 1106-1111 (2010).
[20] D. E. Spratt, X. Pei, J. Yamada, M. A. Kollmeier, B. Cox and M. J. Zelefsky,"Long-term Survival and Toxicity in Patients Treated With High-Dose Intensity Modulated Radiation Therapy for Localized Prostate Cancer," Int J Radiat Oncol **85** (3), 686-692 (2013).
[21] A. V. D'Amico, R. Whittington, S. B. Malkowicz, D. Schultz, K. Blank, G. A. Broderick, J. E. Tomaszewski, A. A. Renshaw, I. Kaplan, C. J. Beard and A. Wein,"Biochemical outcome after radical prostatectomy, external beam radiation therapy, or interstitial radiation therapy for clinically localized prostate cancer," Jama-J Am Med Assoc **280** (11), 969-974 (1998).
[22] M. J. Zelefsky, Y. Yamada, X. Pei, M. Hunt, G. Cohen, Z. G. Zhang and M. Zaider,"Comparison of Tumor Control and Toxicity Outcomes of High-dose Intensity-modulated Radiotherapy and Brachytherapy for Patients With Favorable Risk Prostate Cancer," Urology **77** (4), 986-990 (2011).
[23] W. J. Morris, M. Keyes, I. Spadinger, W. Kwan, M. Liu, M. McKenzie, H. Pai, T. Pickles and S. Tyldesley,"Population-based 10-year oncologic outcomes after low-dose-rate brachytherapy for low-risk and intermediate-risk prostate cancer," Cancer **119** (8), 1537-1546 (2013).
[24] J. B. Malcolm, M. D. Fabrizio, B. B. Barone, R. W. Given, R. S. Lance, D. F. Lynch, J. W. Davis, M. E. Shaves and P. F. Schellhammer,"Quality of life after open or robotic prostatectomy, cryoablation or brachytherapy for localized prostate cancer," J Urol **183** (5), 1822-1828 (2010).
[25] M. G. Sanda, R. L. Dunn, J. Michalski, H. M. Sandler, L. Northouse, L. Hembroff, X. H. Lin, T. K. Greenfield, M. S. Litwin, C. S. Saigal, A. Mahadevan, E. Klein, A. Kibel, L. L. Pisters, D. Kuban, I. Kaplan, D. Wood, J. Ciezki, N. Shah and J. T. Wei,"Quality of life and satisfaction with outcome among prostate-cancer survivors," New Engl J Med **358** (12), 1250-1261 (2008).

[26] M. S. Litwin, J. L. Gore, L. Kwan, J. M. Brandeis, S. P. Lee, H. R. Withers and R. E. Reiter,"Quality of life after surgery, external beam irradiation, or brachytherapy for early-stage prostate cancer," Cancer **109** (11), 2239-2247 (2007).
[27] A. Pollack, G. K. Zagars, G. Starkschall, J. A. Antolak, J. J. Lee, E. Huang, A. C. von Eschenbach, D. A. Kuban and I. Rosen,"Prostate cancer radiation dose response: Results of the M. D. Anderson phase III randomized trial," Int J Radiat Oncol **53** (5), 1097-1105 (2002).
[28] J. Staffurth and R. D. Board,"A Review of the Clinical Evidence for Intensity-modulated Radiotherapy," Clin Oncol-Uk **22** (8), 643-657 (2010).
[29] J. Hanley, M. A. Lumley, G. S. Mageras, J. Sun, M. J. Zelefsky, S. A. Leibel, Z. Fuks and G. J. Kutcher,"Measurement of patient positioning errors in three-dimensional conformal radiotherapy of the prostate," Int J Radiat Oncol **37** (2), 435-444 (1997).
[30] J. Wu, T. Haycocks, H. Alasti, G. Ottewell, N. Middlemiss, M. Abdolell, P. Warde, A. Toi and C. Catton,"Positioning errors and prostate motion during conformal prostate radiotherapy using on-line isocentre set-up verification and implanted prostate markers," Radiotherapy and Oncology **61** (2), 127-133 (2001).
[31] A. J. Nederveen, H. Dehnad, U. A. van der Heide, R. J. A. van Moorselaar, P. Hofman and J. J. W. Lagendijk,"Comparison of megavoltage position verification for prostate irradiation based on bony anatomy and implanted fiducials," Radiotherapy and Oncology **68** (1), 81-88 (2003).
[32] J. M. Schallenkamp, M. G. Herman, J. J. Kruse and T. M. Pisansky,"Prostate position relative to pelvic bony anatomy based on intraprostatic gold markers and electronic portal imaging," Int J Radiat Oncol **63** (3), 800-811 (2005).
[33] M. M. Poggi, D. A. Gant, W. Sewchand and W. B. Warlick,"Marker seed migration in prostate localization," Int J Radiat Oncol **56** (5), 1248-1251 (2003).
[34] P. A. Kupelian, T. R. Willoughby, S. L. Meeks, A. Forbes, T. Wagner, M. Maach and K. M. Langen,"Intraprostatic fiducials for localization of the prostate gland: Monitoring intermarker distances during radiation therapy to test for marker stability," Int J Radiat Oncol **62** (5), 1291-1296 (2005).
[35] A. M. Nichol, K. K. Brock, G. A. Lockwood, D. J. Moseley, T. Rosewall, P. R. Warde, C. N. Catton and D. A. Jaffray,"A magnetic resonance imaging study of prostate deformation relative to implanted gold fiducial markers," Int J Radiat Oncol **67** (1), 48-56 (2007).
[36] G. J. van der Wielen, T. F. Mutanga, L. Incrocci, W. J. Kirkels, E. M. V. Osorio, M. S. Hoogeman, B. J. M. Heijmen and H. C. J. de Boer,"Deformation of Prostate and Seminal Vesicles Relative to Intraprostatic Fiducial Markers," Int J Radiat Oncol **72** (5), 1604-1611 (2008).
[37] T. F. Mutanga, H. C. J. de Boer, G. J. van der Wielen, M. S. Hoogeman, L. Incrocci and B. J. M. Heijmen,"Margin Evaluation in the Presence of Deformation, Rotation, and Translation in Prostate and Entire Seminal Vesicle Irradiation with Daily Marker-Based Setup Corrections," Int J Radiat Oncol **81** (4), 1160-1167 (2011).
[38] J. C. Stroom, H. C. de Boer, H. Huizenga and A. G. Visser,"Inclusion of geometrical uncertainties in radiotherapy treatment planning by means of coverage probability," Int J Radiat Oncol Biol Phys **43** (4), 905-919 (1999).
[39] M. van Herk, P. Remeijer, C. Rasch and J. V. Lebesque,"The probability of correct target dosage: dose-population histograms for deriving treatment margins in radiotherapy," Int J Radiat Oncol Biol Phys **47** (4), 1121-1135 (2000).
[40] J. Leong,"Implementation of random positioning error in computerised radiation treatment planning systems as a result of fractionation," Phys Med Biol **32** (3), 327-334 (1987).
[41] M. van Herk,"Errors and margins in radiotherapy," Seminars in Radiation Oncology **14** (1), 52-64 (2004).

[42] D. Yan, D. Lockman, D. Brabbins, L. Tyburski and A. Martinez,"An off-line strategy for constructing a patient-specific planning target volume in adaptive treatment process for prostate cancer," Int J Radiat Oncol Biol Phys **48** (1), 289-302 (2000).
[43] D. Yan, J. Wong, F. Vicini, J. Michalski, C. Pan, A. Frazier, E. Horwitz and A. Martinez,"Adaptive modification of treatment planning to minimize the deleterious effects of treatment setup errors," Int J Radiat Oncol Biol Phys **38** (1), 197-206 (1997).
[44] J. Boisvert, F. Cheriet, X. Pennec, H. Labelle and N. Ayache,"Geometric variability of the scoliotic spine using statistics on articulated shape models," IEEE Trans Med Imaging **27** (4), 557-568 (2008).
[45] L. Wang, F. Beg, T. Ratnanather, C. Ceritoglu, L. Younes, J. C. Morris, J. G. Csernansky and M. I. Miller,"Large deformation diffeomorphism and momentum based hippocampal shape discrimination in dementia of the Alzheimer type," IEEE Trans Med Imaging **26** (4), 462-470 (2007).
[46] M. Sohn, M. Birkner, D. Yan and M. Alber,"Modelling individual geometric variation based on dominant eigenmodes of organ deformation: implementation and evaluation," Phys Med Biol **50** (24), 5893-5908 (2005).
[47] Q. Zhang, A. Pevsner, A. Hertanto, Y. C. Hu, K. E. Rosenzweig, C. C. Ling and G. S. Mageras,"A patient-specific respiratory model of anatomical motion for radiation treatment planning," Med Phys **34** (12), 4772-4781 (2007).
[48] A. M. Badawi, E. Weiss, W. C. Sleeman, C. Y. Yan and G. D. Hugo,"Optimizing principal component models for representing interfraction variation in lung cancer radiotherapy," Medical Physics **37** (9), 5080-5091 (2010).
[49] E. Budiarto, M. Keijzer, P. R. Storchi, M. S. Hoogeman, L. Bondar, T. F. Mutanga, H. C. de Boer and A. W. Heemink,"A population-based model to describe geometrical uncertainties in radiotherapy: applied to prostate cases," Phys Med Biol **56** (4), 1045-1061 (2011).
[50] E. Budiarto, M. Keijzer, P. R. M. Storchi, A. W. Heemink, S. Breedveld and B. J. M. Heijmen,"Computation of mean and variance of the radiotherapy dose for PCA-modeled random shape and position variations of the target," Physics in Medicine and Biology **59** (2), 289-310 (2014).
[51] M. J. Murphy, (NIH, Virginia Commonwealth University, 2004), pp. 158-187.
[52] J. F. Williamson, (NIH, Virginia Commonwealth University, 2004), pp. 234-269.
[53] J. F. Williamson, (NIH, Virginia Commonwealth University, 2004), pp. 356-368.
[54] H. A. Mcnair, V. N. Hansen, C. C. Parker, P. M. Evans, A. Norman, E. Miles, E. J. Harris, L. Del-Acroix, E. Smith, R. Keane, V. S. Khoo, A. C. Thompson and D. P. Dearnaley,"A comparison of the use of bony anatomy and internal markers for offline verification and an evaluation of the potential benefit of online and offline verification protocols for prostate radiotherapy," Int J Radiat Oncol **71** (1), 41-50 (2008).
[55] G. Soete, M. De Cock, D. Verellen, D. Michielsen, F. Keuppens and G. Storme,"X-ray-assisted positioning of patients treated by conformal arc radiotherapy for prostate cancer: Comparison of setup accuracy using implanted markers versus bony structures," Int J Radiat Oncol **67** (3), 823-827 (2007).
[56] J. J. Gordon, N. Sayah, E. Weiss and J. V. Siebers,"Coverage optimized planning: probabilistic treatment planning based on dose coverage histogram criteria," Med Phys **37** (2), 550-563 (2010).
[57] K. E. I. Deurloo, R. J. H. M. Steenbakkers, L. J. Zijp, J. A. de Bois, P. J. C. M. Nowak, C. R. N. Rasch and M. van Herk,"Quantification of shape variation of prostate and seminal vesicles during external beam radiotherapy," Int J Radiat Oncol **61** (1), 228-238 (2005).
[58] G. E. Christensen and H. J. Johnson,"Consistent image registration," IEEE Trans Med Imaging **20** (7), 568-582 (2001).

[59] M. J. Murphy, F. J. Salguero, J. V. Siebers, D. Staub and C. Vaman,"A method to estimate the effect of deformable image registration uncertainties on daily dose mapping," Medical Physics **39** (2), 573-580 (2012).
[60] E. Parzen,"On estimation of a probability density function and mode," The Annals of Mathematical Statistics **33** (3), 1065-1076 (1962).
[61] M. Rosenblatt,"Remarks on some nonparametric estimates of a density function," The Annals of Mathematical Statistics, 832-837 (1956).
[62] B. W. Silverman, *Density estimation for statistics and data analysis*. (Chapman and Hall, London ; New York, 1986).
[63] H. Xu, D. J. Vile, M. Sharma, J. J. Gordon and J. V. Siebers,"Coverage-based treatment planning to accommodate deformable organ variations in prostate cancer treatment," Med Phys **41** (10), 101705 (2014).
[64] M. H. P. Smitsmans, J. de Bois, J. J. Sonke, A. Betgen, L. J. Zijp, D. A. Jaffray, J. V. Lebesque and M. van Herk,"Automatic prostate localization on cone-beam CT scans for high precision image-guided radiotherapy," Int J Radiat Oncol **63** (4), 975-984 (2005).
[65] M. H. P. Smitsmans, J. W. H. Wolthaus, X. Artignan, J. De Bois, D. A. Jaffray, J. V. Lebesque and M. Van Herk,"Automatic localization of the prostate for on-line or off-line image-guided radiotherapy," Int J Radiat Oncol **60** (2), 623-635 (2004).
[66] M. Sharma, E. Weiss and J. V. Siebers,"Dose deformation-invariance in adaptive prostate radiation therapy: Implication for treatment simulations," Radiotherapy and Oncology **105** (2), 207-213 (2012).
[67] N. Wen, A. Kumarasiri, T. Nurushev, J. Burmeister, L. Xing, D. Z. Liu, C. Glide-Hurst, J. Kim, H. L. Zhong, B. Movsas and I. J. Chetty,"An assessment of PTV margin based on actual accumulated dose for prostate cancer radiotherapy," Physics in Medicine and Biology **58** (21), 7733-7744 (2013).
[68] M. J. Zelefsky, Z. Fuks, M. Hunt, Y. Yamada, C. Marion, C. C. Ling, H. Amols, E. S. Venkatraman and S. A. Leibel,"High-dose intensity modulated radiation therapy for prostate cancer: Early toxicity and biochemical outcome in 772 patients," Int J Radiat Oncol **53** (5), 1111-1116 (2002).
[69] M. J. Zelefsky, Z. Fuks, T. Wolfe, G. J. Kutcher, C. Burman, C. C. Ling, E. S. Venkatraman and S. A. Leibel,"Locally advanced prostatic cancer: Long-term toxicity outcome after three-dimensional conformal radiation therapy - a dose-escalation study," Radiology **209** (1), 169-174 (1998).
[70] A. Niemierko,"A generalized concept of equivalent uniform dose (EUD)," Med Phys **26** (6), 1100 (1999).
[71] Q. W. Wu, R. Mohan, A. Niemierko and R. Schmidt-Ullrich,"Optimization of intensity-modulated radiotherapy plans based on the equivalent uniform dose," Int J Radiat Oncol **52** (1), 224-235 (2002).
[72] M. Fatyga, B. S. Zhang and W. C. Sleeman,"Designing and Implementing a Computing Framework for Image-Guided Radiation Therapy Research," Comput Sci Eng **14** (4), 57-68 (2012).
[73] J. Gordon, A. Crimaldi and J. Siebers,"Evaluation of clinical margins via simulation of patient setup errors in 27 prostate IMRT plans," Medical Physics **33** (6), 2187-2187 (2006).
[74] J. J. Gordon, A. J. Crimaldi, M. Hagan, J. Moore and J. V. Siebers,"Evaluation of clinical margins via simulation of patient setup errors in prostate IMRT treatment plans," Medical Physics **34** (1), 202-214 (2007).
[75] C. M. Bishop, *Pattern recognition and machine learning*. (Springer, New York, 2006).
[76] S. C. Erridge, Y. Seppenwoolde, S. H. Muller, M. van Herk, K. De Jaeger, J. S. A. Belderbos, L. J. Boersma and J. V. Lebesque,"Portal imaging to assess set-up errors, tumor motion and tumor shrinkage during conformal radiotherapy of non-small cell lung cancer," Radiotherapy and Oncology **66** (1), 75-85 (2003).

[77] K. E. Sixel, M. Ruschin, R. Tirona and P. C. F. Cheung,"Digital fluoroscopy to quantify lung tumor motion: Potential for patient-specific planning target volumes," Int J Radiat Oncol **57** (3), 717-723 (2003).
[78] H. H. Liu, P. Balter, T. Tutt, B. Choi, J. Zhang, C. Wang, M. Chi, D. S. Luo, T. S. Pan, S. Hunjan, G. Starkschall, I. Rosen, K. Prado, Z. X. Liao, J. Chang, R. Komaki, J. D. Cox, R. Mohan and L. Dong,"Assessing respiration-induced tumor motion and internal target volume using four-dimensional computed tomography for radiotherapy of lung cancer," Int J Radiat Oncol **68** (2), 531-540 (2007).
[79] K. M. Langen and D. T. L. Jones,"Organ motion and its management," Int J Radiat Oncol **50** (1), 265-278 (2001).
[80] S. Mori, R. Hara, T. Yanagi, G. C. Sharp, M. Kumagai, H. Asakura, R. Kishimoto, S. Yamada, S. Kandatsu and T. Kamada,"Four-dimensional measurement of intrafractional respiratory motion of pancreatic tumors using a 256 multi-slice CT scanner," Radiotherapy and Oncology **92** (2), 231-237 (2009).
[81] C. Beltran, M. G. Herman and B. J. Davis,"Planning target margin calculations for prostate radiotherapy based on intrafraction and interfraction motion using four localization methods," Int J Radiat Oncol **70** (1), 289-295 (2008).
[82] T. C. Y. Chan, T. Bortfeld and J. N. Tsitsiklis,"A robust approach to IMRT optimization," Medical Physics **33** (6), 2061-2061 (2006).
[83] J. Unkelbach and U. Oelfke,"Inclusion of organ movements in IMRT treatment planning via inverse planning based on probability distributions," Physics in Medicine and Biology **49** (17), 4005-4029 (2004).
[84] J. Unkelbach and U. Oelfke,"Incorporating organ movements in inverse planning: assessing dose uncertainties by Bayesian inference," Physics in Medicine and Biology **50** (1), 121-139 (2005).
[85] M. Sohn, B. Sobotta and M. Alber,"Dosimetric treatment course simulation based on a statistical model of deformable organ motion," Phys Med Biol **57** (12), 3693-3709 (2012).
[86] Q. Chen, R. J. Wynne, P. Goulding and D. Sandoz,"The application of principal component analysis and kernel density estimation to enhance process monitoring," Control Eng Pract **8** (5), 531-543 (2000).
[87] M. vanHerk, A. Bruce, A. P. G. Kroes, T. Shouman, A. Touw and J. V. Lebesque,"Quantification of organ motion during conformal radiotherapy of the prostate by three dimensional image registration," Int J Radiat Oncol **33** (5), 1311-1320 (1995).
[88] L. Younes, A. Q. Qiu, R. L. Winslow and M. I. Miller,"Transport of relational structures in groups of diffeomorphisms," J Math Imaging Vis **32** (1), 41-56 (2008).
[89] M. Lorenzi, N. Ayache, X. Pennec and A. D. Neuroimaging,"Schild's Ladder for the Parallel Transport of Deformations in Time Series of Images," Lect Notes Comput Sc **6801**, 463-474 (2011).

Appendix A: Principal component analysis (PCA)

PCA is a widely used technique in linear algebra that is designed to extract relevant trends and structure from large datasets. It does so by taking data of a high dimensionality, and reducing it to a smaller group that encompasses the majority of the variability in the data. This is done by performing an orthogonal transformation on the data so that the greatest variance by any projection lies along the first coordinate, the second greatest variance along the second, and so forth. There are many ways to perform this analysis, but the one used in this research will be presented here.

Input Data

The formation of the data matrix is essential for a successful implementation of PCA. Suppose we perform a single measurement of M distinct variables and place them in a data vector, $\mathbf{X}_1$ as shown below.

$$\mathbf{X}_1 = \begin{bmatrix} x_{1,1} \\ x_{1,2} \\ \vdots \\ x_{1,M} \end{bmatrix} \tag{16}$$

Now suppose that a measurement of these same variables is repeated J times, each producing a vector similar to that in equation (16). The data matrix to describe these measurements will now be defined as

$$\mathbf{X} = \begin{bmatrix} \mathbf{X}_1 & \mathbf{X}_2 & \cdots & \mathbf{X}_J \end{bmatrix} = \begin{bmatrix} x_{1,1} & x_{2,1} & \cdots & x_{J,1} \\ x_{1,2} & x_{2,2} & \cdots & x_{J,2} \\ \vdots & \vdots & \ddots & \vdots \\ x_{1,M} & x_{2,M} & \cdots & x_{J,M} \end{bmatrix} \tag{17}$$

PCA works on mean subtracted data, so the mean must be computed for each row to give the mean value matrix, $\bar{\mathbf{X}}$.

$$\bar{\mathbf{X}} = \frac{1}{J}\sum_{i=1}^{J} \mathbf{X}_i \tag{18}$$

The final data matrix operated on by the PCA is

$$\mathbf{X}_{MS} = \begin{bmatrix} \mathbf{X}_1 - \bar{\mathbf{X}} & \mathbf{X}_2 - \bar{\mathbf{X}} & \cdots & \mathbf{X}_J - \bar{\mathbf{X}} \end{bmatrix} \tag{19}$$

Covariance Matrix

The covariance between two random variables is a description of how these variables change together. For the random scalar variables x and y, the covariance, $\sigma(x,y)$, of these two is defined as

$$\sigma(x,y) = E\left[\left(x - E(x)\right)\left(y - E(y)\right)\right] \tag{20}$$

where $E(\ )$ is the expectation value. Note that when $x = y$, the covariance is equivalent to the variance. For a group of variables, like those defined in equation (19), the $M \times M$ sample covariance matrix, $\boldsymbol{\Sigma}$, is computed as follows

$$\boldsymbol{\Sigma} = \frac{1}{J-1}\mathbf{X}_{MS}\mathbf{X}_{MS}^{T} \tag{21}$$

This matrix gives the covariance between each data point in the data matrix, $\mathbf{X}_{MS}$, in the non-diagonal locations and the variances along the diagonal.

Orthogonal Transformation

PCA now requires that the covariance matrix, $\boldsymbol{\Sigma}$, undergo an eigendecomposition. Mathematically, this means that the linearly independent eigenvectors (also called eigenmodes), $\mathbf{v}$, and the eigenvalues, λ, are found that satisfy the well-known eigenvalue equation.

$$\boldsymbol{\Sigma}\mathbf{v} = \lambda\mathbf{v} \tag{22}$$

Because the covariance matrix is symmetric, the spectral theorem guarantees it to be diagonalizable, and therefore contains $J-1$ associated pairs of eigenvectors and eigenvalues.

The eigenvalues give the relative importance of each eigenvector. The fraction of the variability of the data that can be represented by the associated eigenvector is given by

$$\bar{\lambda}_i = \lambda_i \Big/ \sum_{i=1}^{J-1} \lambda_i \tag{23}$$

The eigenvalue with the largest fraction is, by definition, the most-principal component, the second largest eigenvalue with the second most-principal component, and so forth. Because of this, the eigenvectors are sorted in descending order by their associated eigenvalues. Typically, only the first L eigenvectors that are needed to account for the specified minimum percentage of the spectral variance (generally 90 to 95%) are kept. The discarded eigenvectors are likely associated with noise in the measurements and not representative of any real data trends.

Data Reconstruction

PCA can be viewed as optimally changing the basis representation of the data variability into orthogonal (statistically independent) modes of variation. However, in most cases, the data must be transformed back into the original basis. This is done with the Karhunen-Loève transform, which allows an arbitrary data vector, $\mathbf{X}_R$, to be reconstructed as a linear combination of the eigenvectors and scaling coefficients

$$\mathbf{X}_R = \sum_{i=1}^{L} c_i \mathbf{v}_i + \bar{\mathbf{X}} \tag{24}$$

The scaling coefficients are found using the dot product of the eigenvectors and the data that is to be reconstructed.

$$c_i = \left(\mathbf{X}_R - \bar{\mathbf{X}}\right) \bullet \mathbf{v}_i \tag{25}$$

This transform can be used to reconstruct the original input data or to model a separate measurement not included in the original d data. If $J - 1 = L$, the original input data can be reconstructed with no loss of information.

High Dimensional Data

The method outlined above becomes cumbersome when M becomes large, due in part to the computationally intractable task of diagonalizing a large-scale $M \times M$ covariance matrix, since M is typically the number of voxels in a 3D image (about 10^7) for this study's application. Solutions to this problem have been proposed, such as the use of singular value decomposition (SVD), which acts directly on the data matrix, $\mathbf{X}_{MS}$ and is computationally stable. However, this work uses a well-known modification of the traditional PCA method described above, which is beneficial when $J \ll M$.[75] The

details of this method are outlined below. First, equation (21) is substituted into equation (22)

$$\frac{1}{J-1}\left(\mathbf{X}_{MS}\mathbf{X}_{MS}^{T}\right)\mathbf{v}=\lambda\mathbf{v} \tag{26}$$

Now multiply both sides by $\mathbf{X}_{MS}^{T}$

$$\frac{1}{J-1}\mathbf{X}_{MS}^{T}\mathbf{X}_{MS}\left(\mathbf{X}_{MS}^{T}\mathbf{v}\right)=\lambda\left(\mathbf{X}_{MS}^{T}\mathbf{v}\right) \tag{27}$$

And define $\mathbf{u}=\mathbf{X}_{MS}^{T}\mathbf{v}$

$$\frac{1}{J-1}\mathbf{X}_{MS}^{T}\mathbf{X}_{MS}\mathbf{u}=\lambda\mathbf{u} \tag{28}$$

Here, it is easy to see that $\mathbf{X}_{MS}^{T}\mathbf{X}_{MS}$ is the much smaller $J\times J$ matrix ($J=19$ in this study), making the eigenvalue problem much simpler to solve. Now multiply both sides by $\mathbf{X}_{MS}$.

$$\frac{1}{J-1}\mathbf{X}_{MS}\mathbf{X}_{MS}^{T}\left(\mathbf{X}_{MS}\mathbf{u}\right)=\lambda\left(\mathbf{X}_{MS}\mathbf{u}\right) \tag{29}$$

Looking within the parenthesis, we see that $\mathbf{X}_{MS}\mathbf{u}$ is an eigenvector for equation (26). Thus, once the eigenvectors, $\mathbf{u}$, are found, the full 3D image eigenvectors, $\mathbf{v}$, can be found by

$$\mathbf{v}=\mathbf{X}_{MS}\mathbf{u} \tag{30}$$

It is important to note that $\mathbf{v}$ may not be properly normalized. In the instance where $\mathbf{u}$ is normalized, and extra factor of $\frac{1}{\sqrt{\lambda\left(J-1\right)}}$ is needed for proper normalization of $\mathbf{v}$.

Appendix B: Population modeling of prostate systematic and random tissue errors using a principal component analysis

Population modeling of prostate systematic and random tissue errors using a principal component analysis

Douglas J. Vile[1], Gary E. Christensen[2], John C. Ford[1], Jeffrey F. Williamson[1]

[1]Department of Radiation Oncology, Virginia Commonwealth University, Richmond, VA, 23298

[2]Department of Radiation Oncology and the Department of Electrical and Computer Engineering, The University of Iowa, Iowa City, IA, 52242

Corresponding author

Douglas J. Vile
Department of Radiation Oncology
Virginia Commonwealth University
401 College Street
PO Box 980058
Richmond, VA 23298
Phone: 804-628-4660
Fax: ___-___-____
E-mail: viledj@vcu.edu

Conflicts of interest

This work is supported in part by NIH grant P01CA116602

Abstract

Purpose: To create a statistical population-based model of systematic and random pelvic tissue motion in prostate cancer patients; extend the concepts of systematic and random error distributions (Σ and σ, respectively) to three dimensions; and demonstrate that the model predicts the magnitude, direction, and probability of systematic and random tissue displacements over a 5-7 week course of treatment.

Methods: CT images from 19 patients, each with a single planning image and 8-13 fractional images, were used in this study. Patient-specific systematic and random tissue displacements were calculated using deformable image registration (DIR) for two different patient setups, a bony aligned setup and a prostate-centroid aligned setup. These vectors were transported to a reference coordinate system using inter-patient displacement vector fields (DVFs) mapping each patient's planning image to the reference image. The error introduced by mapping to and from the reference image was quantified. With all patient data in a common coordinate system, Σ and σ were computed for each voxel within the prostate, bladder, and rectum. Principal component analysis (PCA) was used to create a statistical model of systematic and random tissue displacements. The PCA modeling error introduced by only including the principal components representing 95% of the data variance was investigated and reported. A leave one out study was performed to investigate the PCA model's ability to represent systematic and random tissue motion not included in the PCA training data. Finally, a method for sampling synthetic deformations from the PCA models was developed, and organ occupancy maps were created and compared between bony and prostrate-centroid aligned patient setups.

Results: Mapping patient-specific systematic and random tissue errors to and from the reference coordinate system introduced an error of about 0.2 mm. The magnitudes of Σ and σ at the reference image prostrate centroid were 1.6 and 1.5 mm, respectively, for prostrate-centroid aligned patient setup and 4.6 and 4.1 mm for bony aligned setup. For the PCA modeling, 11 eigenmodes were needed to describe 95% of the data variance in the systematic

motion model, while 33 were needed to describe 95% of the variance in the random motion model. Using the limited number of eigenmodes introduced modeling error in the original data of less than 1 mm. In the leave one out study, systematic errors within the prostate, bladder, and rectum not included in the PCA model were reconstructed with absolute mean errors between 1 - 2 mm. Random errors had absolute mean errors between 0.5 - 0.9 mm for each organ.

Conclusions: Systematic and random pelvic tissue positioning errors were modeled using a PCA statistical model to within an error of 1-2 mm. The authors developed, implemented and validated a PCA-based technique to determine the principal modes of systematic and random organ deformation. In the population under study, the prostate-centroid aligned technique reduced the Σ and σ in the areas of clinical interest and gave greater certainty in prostate localization compared to bony alignment.

Key words

PCA, prostate cancer, systematic errors, random errors, population model

1. Introduction

Organ motion has long since been a challenge across all anatomical sites in radiotherapy. Hereafter, "organ motion" will refer to either the displacement or deformation of the anatomy of the treatment day from the planning anatomy. The magnitudes of the motion have been extensively studied and reported for intrafraction motion, e.g. lung[76-78] and pancreas[79,80], as well as interfraction motion, e.g., pelvis[1,79,81]. Each site presents different challenges and requires different motion-management strategies.

It is often beneficial to separate interfraction organ motion into its systematic and random components. A systematic targeting error is the discrepancy between the anatomy that is planned and the patient's mean anatomy throughout their treatment. The daily residual motion after being corrected for by the systematic component is random targeting error. It has become common practice to use online image-guided radiotherapy (IGRT) in order to reduce the effect of the motion on tumor targeting. However, current deterministic corrections use only a rigid shift of the patient, which cannot account for the residual 3D aspects of the motion, such as soft tissue deformation. The current practice for prostate cancer is daily rigid alignment based on implanted fiducials. This still leaves residual systematic and random errors introduced by soft tissue deformation. In most cases, organ rotations are not taken into consideration. Organs at risk (OARs), such as the highly deformable rectum and bladder, are also not taken into account, even though their motion could cause higher toxicities than anticipated based on the planning image. In lung cancer, tracking cycle-to-cycle variations around the mean is difficult and when technically feasible, is limited to translational isocenter position corrections.

When direct measurement and incorporation of each day's organ motion into the plan of the day is not feasible, probabilistic treatment planning (PTP) may be an option. Rather than correcting for each instance of organ motion, from knowledge of the distribution of organ-motion errors, PTP endeavors to maximize the probability of achieving specified planning goals. These goals vary, as does the complexity of the planning technique. The simplest and most widely

used PTP method is the clinical target volume (CTV)-to-planning target volume (PTV) expansion margin. To determine the necessary margin, several formulas have been proposed based on varying assumptions about the dose coverage to most patients in a population, including normality of the systematic and random error spatial distributions. The most well-known formula was proposed by van Herk, who sought to deliver 95% of the prescription as the minimum dose to the CTV for 90% of all patients.[39] As input, this formula requires the distribution of systematic and random errors of the tumor centroid relative to the planning image for the patient population. This formula is limited by its underlying assumptions, as it treats the tumor as a rigid body, and does not account for the deformable nature of the tumor and completely ignores OARs (organs at risk). More advanced PTP methods have been developed to directly incorporate the probability of a given anatomical instance directly into plan optimization.[56,82-84] These methods are only as good as their input model describing the statistics of the patient's organ motion. Currently, there are few fully 3D statistical models of organ motion that compute the probability of random and systematic instances of anatomy.

The goal of this paper is to address this void and to extend the concept of systematic and random error from a single tumor centroid to every voxel within the CTV, as well as the associated OARs in the male pelvis. This avoids assumptions of the rigidity/non-rigidity of the organs. This paper applies principal component analysis (PCA) modeling to deformable image registrations (DIR) in order to statistically model these anatomical systematic and random displacements throughout a patient's treatment course. DIR produces displacement vector fields (DVFs), which quantify the inter-fractional organ motion. While others have used the PCA technique to investigate patient-specific random tissue displacements[46,85] and even random displacements across a population[49], this paper is the first to model both random and systematic error distributions for the prostate patient population.

In this paper, patient-specific systematic and random errors (as described by DVFs), are transported to a common coordinate system though inter-patient DIR. With each patient's data

in a common reference frame, PCA is used to model the principal modes of systematic and random organ motion.

2. Methods

2.1 Patient dataset

Fan beam computed tomography (CT) images of the male pelvis collected at the Netherlands Cancer Institute (NKI) from $N = 19$ patients undergoing definitive external beam radiotherapy for prostate cancer were used in this study. All images were anonymized. Each patient was imaged once before treatment and 8-13 times (median 11) throughout the course of treatment. Let $\Omega \subset \mathbb{R}^3$ denote the domain of a CT image. Denote $I_{i,k}: \Omega \to \mathbb{R}$ as the CT image of the ith patient and the kth fractional image were $1 \le i \le N$ and $0 \le i \le P_i$. By convention, $k = 0$ denotes the pretreatment CT image and P_i denotes the number of fraction images of the ith patient. There were 210 fractional images in this dataset., The 3D prostate, bladder, and rectum were contoured by a single experienced radiation oncologist on each of these images. The cutoff for the superior boundary of the rectum was the inferior edge of the iliosacral joints. Protocols for data acquisition were previously reported by Deurloo.[57]

For each patient, two different patient setups were investigated. The first approach aligned all fractional images to the planning image by matching a set of bony landmarks. The second approach aligned all fractional images to the planning image by aligning the prostate centroid in the fractional images to the prostate centroid in the planning image. The prostrate centroid was calculated from physician-drawn contours of each image. No rotations were considered in the initial patient alignment.

2.2 Deformable image registration

2.2.1 Intra-patient DIR

Define $\mathbf{h}_{(i,k)\to(i,0)} : \Omega \to \Omega$ as the Eulerian transformation that maps the k[th] fractional image of the i[th] patient $I_{i,k}$ to the reference image $I_{i,0}$. Denote $\mathbf{u}_{(i,k)\to(i,0)} : \Omega \to \Omega$ as the displacement vector field (DVF) associated with $\mathbf{h}_{(i,k)\to(i,0)}$ where

$$\mathbf{h}_{(i,k)\to(i,0)}\left(\mathbf{x}\right) = \mathbf{x} + \mathbf{u}_{(i,k)\to(i,0)}\left(\mathbf{x}\right) \text{ for } \mathbf{x} \in \Omega \quad (1)$$

Deformable image registration (DIR) was used to determine the transformation. This was done using the SICLE algorithm (small deformation, inverse consistent, linear elastic) using both grayscale and contour matching for the bladder, prostate, and rectum.[58] SICLE's objective function contains intensity matching, inverse consistency, and regularizing terms. The intensity matching is done using a sum of squares differences using both CT intensities and contour information. Contours were incorporated into the algorithm by converting each contour into a binary mask image. The algorithm simultaneously searches for both forward and inverse DVFs relating the two input images and their associated contour masks. The objective function contains terms penalizing inverse inconsistent registrations. A linear elastic regularizing term is also included in the objective function. The transformation is parameterized using a Fourier basis. The weighting coefficients of the Fourier bases are the output parameters of SICLE. The algorithm utilizes a multi-resolution approach, starting off minimizing the objective function on a coarse grid of the images and iteratively refining the parameters on a finer grid. The resultant DVFs spanned the whole image with voxel sizes of approximately 1.8x1.8x0.3mm. The images were initially rigidly aligned using the bony anatomy. The physician-drawn contours were used to validate this algorithm. The output DVFs were used to deform the contours and the Dice similarity metric was used to compare the deformed contours with the physician drawn ground truth. This was done for every transformation deforming a fractional to the planning image. Over all fractions and all patients, resultant Dice similarity indices for the prostate, bladder, and rectum were (mean±SD) 0.92±0.02, 0.95±0.03, and 0.89±0.03 respectively.

2.2.2 Inter-patient deformable registration and construction of a reference image

Pooling data across patients to create a statistical model of DVF variability in a population of patients requires a common coordinate system. This was achieved by deforming each patient's reference image $I_{i,0}$ to a population reference image I_{ref}. In principle, the resulting inter-patient transformation $\mathbf{h}_{(i,k)\to ref}$ can be used to transport intra-patient DVFs $\mathbf{u}_{(i,k)\to(i,0)}\left(\mathbf{x}_{i,0}\right)$ derived from different patients onto the coordinate system of I_{ref} where they can be indexed and compared to one another in a common coordinate system.

Inter-patient registration of the pelvic anatomy is extremely challenging for most DIR algorithms. This is due to many reasons including differences in anatomy, abutting organs in the source image may be separated in the target image or vice versa, and organs may slide against one another from one image to the next. The SICLE image registration algorithm assumes that two images can be registered using a continuous transformation parameterized by the 3D Fourier series. As a result, the SICLE algorithm performs poorly in regions where abutting organs separate or slide against one another. In these instances, registrations using all organ segmentations simultaneously failed. Consequently, we performed separate single-organ deformable registrations for the three central pelvic organs (bladder, prostate, and rectum) to allow for the most accurate registration for each organ.

To derive I_{ref} (with support limited to the three central pelvic structures), SICLE contour driven registration was performed to register each patient's planning contours to the corresponding contours of a preselected patient. This preselected patient was chosen for its lack of abnormal anatomy (i.e. minimal bowel gas, average prostate size) upon visual inspection. The organ-specific DVFs that map voxels from the preselected $I_{p,0}$ to every other $I_{i,0}, i \neq p$ were then averaged to calculate the mean organ-specific DVF. The mean DVFs were then used to deformably map the central organs from $I_{p,0}$ into I_{ref}, creating a stitched average

simulation image, consisting of binary images of the bladder, rectum, and prostate. We then deformably registered each of the 19 patient's central pelvic organs as contoured on planning images, one at a time, to the corresponding structures on I_{ref}. This yielded the transformations $\mathbf{h}^{bladder}_{(i,0)\to ref}$, $\mathbf{h}^{prostate}_{(i,0)\to ref}$, and $\mathbf{h}^{rectum}_{(i,0)\to ref}$, along with the inverse mappings $\mathbf{g}^{bladder}_{(i,0)\to ref}$, $\mathbf{g}^{prostate}_{(i,0)\to ref}$, and $\mathbf{g}^{rectum}_{(i,0)\to ref}$. These transformations were subsequently used to transfer systematic and random statistical information to and from the average reference patient, where the data can be pooled and compared.

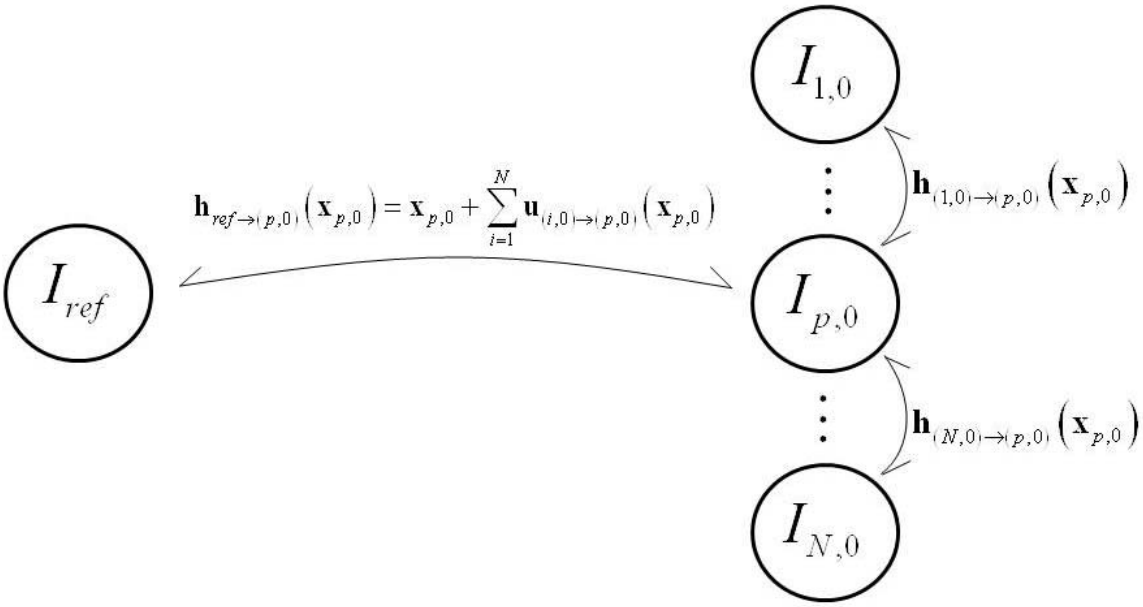

Figure 1. The creation of the reference image. Patient planning images are first registered to a single patient's planning image, from which the reference image is then created using the mean deformation.

2.3 Development of a statistical model of deformed anatomies

2.3.1 Systematic and random anatomical deformations

We assume that each patient's DVF describing the mapping of a fractional anatomy to its planning anatomy, $\mathbf{u}_{(i,k)\to(i,0)}(\mathbf{x}_{i,0})$, is the sum of systematic and random components, $\bar{\mathbf{u}}_i(\mathbf{x}_{i,0})$ and $\Delta\mathbf{u}_{(i,k)\to(i,0)}(\mathbf{x}_{i,0})$, respectively. The systematic component is defined as the DVF which

maps each voxel from its planning image, $I_{i,0}$ to its location, averaged over its positions in each daily treatment image, $I_{i,k}$.

$$\bar{\mathbf{u}}_i\left(\mathbf{x}_{i,0}\right)=\frac{1}{P_i}\sum_{k=1}^{P_i}\mathbf{u}_{(i,k)\to(i,0)}\left(\mathbf{x}_{i,0}\right) \tag{2}$$

Each patient has a single $\bar{\mathbf{u}}_i\left(\mathbf{x}_{i,0}\right)$. The day-to-day fluctuations of anatomical deformations about $\bar{\mathbf{u}}_i\left(\mathbf{x}_{i,0}\right)$ are represented by $\Delta\mathbf{u}_{(i,k)\to(i,0)}\left(\mathbf{x}_{i,0}\right)$, which describes the k-th fraction offset of each voxel $\mathbf{x}_{i,0}$ from the planning image in treatment fraction k from its mean location, $\bar{\mathbf{u}}_i\left(\mathbf{x}_{i,0}\right)$, during the treatment course.

$$\Delta\mathbf{u}_{(i,k)\to(i,0)}\left(\mathbf{x}_{i,0}\right)=\mathbf{u}_{(i,k)\to(i,0)}\left(\mathbf{x}_{i,0}\right)-\bar{\mathbf{u}}_i\left(\mathbf{x}_{i,0}\right) \tag{3}$$

For brevity, $\bar{\mathbf{u}}_i\left(\mathbf{x}_{i,0}\right)$ and $\Delta\mathbf{u}_{(i,k)\to(i,0)}\left(\mathbf{x}_{i,0}\right)$, are hence referred to as "systematic DVF component" and "random DVF component," respectively. These quantities are 3D generalizations of the systematic and random setup error concepts utilized in the margin formula by van Herk.[39]

2.3.2 Transport of patient-specific vector fields into reference coordinate system

The systematic and random DVF components, $\bar{\mathbf{u}}_i\left(\mathbf{x}_{i,0}\right)$ and $\Delta\mathbf{u}_{(i,k)\to(i,0)}\left(\mathbf{x}_{i,0}\right)$, which are functions of the patient-specific simulation-image coordinate systems, are transported organ-by-organ to the reference coordinate system, $\mathbf{x}_{ref}$, using the inter-patient DVFs, $\mathbf{u}^{bladder}_{(i,0)\to ref}\left(\mathbf{x}_{ref}\right)$, $\mathbf{u}^{prostate}_{(i,0)\to ref}\left(\mathbf{x}_{ref}\right)$, and $\mathbf{u}^{rectum}_{(i,0)\to ref}\left(\mathbf{x}_{ref}\right)$. This is done by treating the systematic and random components as vector-valued images and deforming their vector fields with the inter-patient DVF.

$$\bar{\mathbf{u}}_i^{ref,\,prostate}\left(\mathbf{x}_{ref}\right)=\bar{\mathbf{u}}_i\left(\mathbf{x}_{ref}+\mathbf{u}^{prostate}_{(i,0)\to ref}\left(\mathbf{x}_{ref}\right)\right) \tag{4}$$

This is done for all organs and for the systematic and random components.

As described below, the resultant components were “stitched” together in the reference coordinate system to form a single systematic or random error, with support limited to the three pelvic structures. The single-organ systematic or random error’s support was taken to be any voxels within the associated organ, plus a 1 cm margin around the organ. The margin was necessary to avoid interpolation errors at the organ surfaces introduced when deforming the reference contours. The stitching for the systematic and random errors is given mathematically below.

$$\bar{\mathbf{u}}_i^{union,ref}\left(\mathbf{x}_{ref}\right)=\begin{cases}\bar{\mathbf{u}}_i^{rectum,ref}\left(\mathbf{x}_{ref}\right) & \text{if } \mathbf{x}_{ref}\in \text{Rectum+1cm}\\ \bar{\mathbf{u}}_i^{bladder,ref}\left(\mathbf{x}_{ref}\right) & \text{if } \mathbf{x}_{ref}\in \text{Bladder+1cm}\\ \bar{\mathbf{u}}_i^{prostate,ref}\left(\mathbf{x}_{ref}\right) & \text{if } \mathbf{x}_{ref}\in \text{Prostate+1cm}\end{cases} \quad (5)$$

and

$$\Delta\mathbf{u}_{i,j}^{union,ref}\left(\mathbf{x}_{ref}\right)=\begin{cases}\Delta\mathbf{u}_{i,j}^{rectum,ref}\left(\mathbf{x}_{ref}\right) & \text{if } \mathbf{x}_{ref}\in \text{Rectum+1cm}\\ \Delta\mathbf{u}_{i,j}^{bladder,ref}\left(\mathbf{x}_{ref}\right) & \text{if } \mathbf{x}_{ref}\in \text{Bladder+1cm}\\ \Delta\mathbf{u}_{i,j}^{prostate,ref}\left(\mathbf{x}_{ref}\right) & \text{if } \mathbf{x}_{ref}\in \text{Prostate+1cm}\end{cases} \quad (6)$$

Volumes where these margins overlapped were handled using a prioritization. The prostate took first priority, the bladder second, and the rectum third. In all, there are N different systematic errors and $\sum_{i=1}^{N} P_i = 210$ random errors, all in the reference coordinate system.

2.4 Inverse consistency

In order for a population model to have value, information extracted from it in the reference coordinate system (e.g. randomly sampled DVFs or summary statistics) must be mapped back to a patient’s local coordinate system. The process of mapping the systematic and random components to and from the reference coordinate system introduces error, due to the DVF stitching and the fact that inter-patient transformations are not exactly inverse consistent. The

impact of these two factors was tested as a whole, and will be referred to subsequently as the "inverse consistency error".

In order to quantify inverse consistency error, the systematic and random errors were mapped to the reference frame, then immediately mapped back to the local patient's frame, where they were compared with original.

$$\bar{\boldsymbol{\delta}}^{o}_{i,IC}\left(\mathbf{x}_{i,0}\right)=\mathbf{g}^{o}_{(i,0)\to ref}\left(\bar{\mathbf{u}}^{o,ref}_{i}\left(\mathbf{x}_{ref}\right)\right)-\bar{\mathbf{u}}^{o,patient}_{i}\left(\mathbf{x}_{i,0}\right)$$

$$\text{for each } \mathbf{x}_{i,0}\text{, find corresponding } \mathbf{x}_{ref}=\mathbf{u}^{o}_{ref\to(i,0)}(\mathbf{x}_{i,0})+\mathbf{x}_{i,0} \tag{7}$$

$$\bar{\boldsymbol{\delta}}^{o}_{i,IC}\left(\mathbf{x}_{i,0}\right)=\bar{\mathbf{u}}^{o,ref}_{i}\left(\mathbf{u}^{o}_{ref\to(i,0)}(\mathbf{x}_{i,0})+\mathbf{x}_{i,0}\right)-\bar{\mathbf{u}}^{o,patient}_{i}\left(\mathbf{x}_{i,0}\right)$$

$\bar{\mathbf{u}}^{o,l}_{i}$ where o = prostate, bladder, rectum, or union and l= patient or ref coordinate system

where "organ" is a placeholder for the prostate, bladder, and rectum, as each organ is done separately. To quantify inverse consistency error, the mean and standard deviation of $\bar{\boldsymbol{\delta}}^{o}_{i,IC}\left(\mathbf{x}_{i,0}\right)$ was averaged over all voxels within the organ for each patient separately, and over the population of patients.

2.5 Quantifying the statistics of systematic and random voxel displacements

The systematic and random error components of the tissue displacement must be transported to the reference coordinate system in order to get a statistical characterization of the entire patient population. The characterization is done by generalizing the well known concepts of group mean, systematic error (Σ), and random error (σ), introduced by van Herk to model statistical fluctuations of setup error, to three dimensions.

The group mean, $\mathbf{M}\left(\mathbf{x}_{ref}\right)$, is defined as

$$\mathbf{M}\left(\mathbf{x}_{ref}\right)=\frac{1}{N}\sum_{i=1}^{N}\bar{\mathbf{u}}^{union,ref}_{i}\left(\mathbf{x}_{ref}\right) \tag{8}$$

Generalizing the classical definition of van Herk, which was limited to the GTV centroid, we define the systematic tissue displacement error, $\boldsymbol{\Sigma}\left(\mathbf{x}_{ref}\right)$, as a function of location, $\mathbf{x}_{ref}$, in the reference image, by

$$\boldsymbol{\Sigma}\left(\mathbf{x}_{ref}\right)=\sqrt{\frac{1}{N-1}\sum_{i=1}^{N}\left(\bar{\mathbf{u}}_{i}^{union,ref}\left(\mathbf{x}_{ref}\right)-\mathbf{M}\left(\mathbf{x}_{ref}\right)\right)^{2}} \tag{9}$$

Similarly, the random error, $\boldsymbol{\sigma}\left(\mathbf{x}_{ref}\right)$, is calculated as the root mean square over all patients of the standard deviation of each patient's daily tissue displacements. Mathematically, it is defined as

$$\boldsymbol{\sigma}\left(\mathbf{x}_{ref}\right)=\sqrt{\frac{1}{N}\sum_{i=1}^{N}\frac{1}{P-1_{i}}\sum_{k=1}^{P_{i}}\left(\Delta\mathbf{u}_{i,k}^{union,ref}\left(\mathbf{x}_{ref}\right)\right)^{2}} \tag{10}$$

2.6 PCA for constructing probability density functions (PDFs) of deformed anatomies

The goal of this statistical model is to quantify the amount of uncertainty in tissue displacements across a population of patients. This knowledge is potentially useful when designing a plan resistant to such uncertainties for a patient whose individual tissue displacements are unknown *a priori*. Equations (8)-(10), above, assume that each voxel moves independently of its neighbors. Obviously, voxels within an organ move coherently, giving rise to significant voxel-to-voxel correlations. The Fourier transformation parameterization and linear elastic regularization present in the DIR used in this work guarantee this correlation. To incorporate these correlations, the statistics of systematic and random errors were modeled using the PCA technique in the reference coordinate system. Supposing there are *L* voxels in the image, we can define the $3L\times N$ matrix of population mean-subtracted systematic data matrices are calculated as

$$\mathbf{D}^{sys} \equiv \mathbf{D}^{sys}_{\mathbf{x}_{ref},i} = \left[\boldsymbol{\Delta}_1(\mathbf{x}),\cdots,\boldsymbol{\Delta}_i(\mathbf{x}),\cdots,\boldsymbol{\Delta}_N(\mathbf{x})\right] = \begin{bmatrix} \boldsymbol{\Delta}_1(x_1) & \cdots & \boldsymbol{\Delta}_N(x_1) \\ \vdots & & \vdots \\ \boldsymbol{\Delta}_1(x_L) & \cdots & \boldsymbol{\Delta}_N(x_L) \end{bmatrix} \tag{11}$$

where $\boldsymbol{\Delta}_1(\mathbf{x}) = \overline{\mathbf{u}}_1^{union,ref}\left(\mathbf{x}\right) - \mathbf{M}\left(\mathbf{x}_{ref}\right)$. The columns of $\mathbf{D}^{sys}$ are the group-mean subtracted patient-specific systematic displacements, while the rows are mean-subtracted systematic displacements of a specific voxel. The same is done to create the random data matrix, $\mathbf{D}^{rand}$. From these, their respective covariance matrices are calculated. The covariance matrix is a measure of each voxel's correlation to the others, and is calculated by

$$\mathbf{C}^{sys} = \frac{1}{N-1}\mathbf{D}^{sys}\left(\mathbf{D}^{sys}\right)^T \tag{12}$$

Similarly, we can define the $3\left(\sum_{i=1}^{N} P_i\right)\times L$ matrix $\mathbf{D}^{rand} = \left[\boldsymbol{\Delta}\mathbf{u}_{i,j}\left(\mathbf{x}_{ref}\right)\left(j=1,\cdots,P_i, i=1,\cdots,N\right)\right]$ and the corresponding covariance matrix

$$\mathbf{C}^{rand} = \frac{1}{\sum_{i=1}^{N} P_i}\mathbf{D}^{rand}\left(\mathbf{D}^{rand}\right)^T \tag{13}$$

PCA is an orthogonal transformation, or eigendecomposition, of the covariance matrix, which seeks to diagonalize the matrix.

$$\begin{aligned} \mathbf{C}^{sys}\mathbf{v}_l^{sys} &= \lambda_l^{sys}\mathbf{v}_l^{sys} \\ \mathbf{C}^{rand}\mathbf{v}_l^{rand} &= \lambda_l^{rand}\mathbf{v}_l^{rand} \end{aligned} \tag{14}$$

λ_l^{sys} and $\mathbf{v}_l^{sys}$ denote the l^{th} of N nonzero eigenvalues and eigenvectors, respectively. In practice, the $3L\times 3L$ matrices are too large to invert. Hence equations (12) and (13) are multiplied by $\left(D^{sys}\right)^T$ or $\left(D^{rand}\right)^T$ transforming the covariance matrix to easily invertible 19x19 or 212x212 matrices and with $3\times L$ eigenvector matrices.[75] The result of each decomposition is an orthonormal set of basis eigenvectors, $\mathbf{v}_l^{sys}$ and $\mathbf{v}_l^{rand}$, that satisfy the eigenvector equation (14).

In principle, any random or systematic deformed instance of 3D anatomy, $\bar{\mathbf{u}}\left(\mathbf{x}_{ref}\right)$, can be expressed as a linear combination of these eigenvectors and scalar expansion coefficients, c_l .

$$\bar{\mathbf{u}}\left(\mathbf{x}_{ref}\right) = \frac{1}{N}\sum_{l=1}^{L_{sys}} c_l \, \mathbf{v}_l^{sys} + \mathbf{M}\left(\mathbf{x}_{ref}\right) \tag{15}$$

In equation (15), L_{sys} represents the number of eigenmodes necessary to account for 95% of the variance in the data. Typically, $L_{sys} < N$, reducing the dimensionality of the problem. The eigenvectors (or eigenmodes) are ordered so that the first principal component, with the largest λ_l accounts for the most variance possible in the data. The second mode is the orthogonal vector that accounts for the next largest contribution to variance, and so forth.

2.7 PCA modeling error

By using a limited number of eigenmodes, some amount of error is introduced when reconstructing the original set of systematic and random spatial distributions. To quantify this error, equation (15) and its random counterpart was used to reconstruct each systematic and random DVF using L_{sys} or L_{rand} eigenmodes. In the $\mathbf{x}_{ref}$ coordinate system, each reconstructed displacement field was compared to the original DVF, and the arithmetic mean and standard deviation of the voxel-by-voxel differences calculated for each organ. For each patient, the discrepancies were further averaged over the 8-13 random component DVFs associated with each patient.

2.8 Leave one out study

For the PCA model to be useful clinically, it must be able to accurately describe systematic and random displacement distributions from patients that were not part of the training set. Nineteen different systematic and random DVF PCA models were built, each using data from 18 patients by excluding each patient in turn. The scaling expansion coefficients required to approximate the patient's systematic and random errors in equation (15) were calculated by

$$c_l = \mathbf{v}_l^{sys} \cdot \left(\bar{\mathbf{u}} \left(\mathbf{x}_{ref} \right) - \mathbf{M}\left(\mathbf{x}_{ref} \right) \right) \quad (16)$$

Then, the systematic DVFs for the omitted patient were estimated using equation (15), with the random DVFs estimated similarly. This process was repeated for the other patients, creating 19 different models in total, each created using data from the other patients. Differences between the DVFs for the 19 omitted patients as reconstructed by PCA and directly calculated by SICLE were evaluated separately for each organ in each patient. The mean and standard deviation of the errors were reported.

2.9 Randomly sampling PCA PDFs and organ occupancy maps

A useful application of the PCA statistical models is the creation of organ occupancy maps. These maps show the probability of an organ of interest occupying each voxel in a patient's simulation image, taking into account both random and systematic anatomy deformation. To create these occupancy maps, samples of systematic and random DVFs must be randomly drawn from the PCA model and then added together in order to create a synthetic deformation. This is done by creating and sampling from a probability density function (PDF) of the expansion coefficients, c_l, associated with each eigenvector in both the systematic and random displacement models. The PDF is created from the histogram of eigenvalues (19 and 210 values for systematic and random DVFs, respectively, for each eigenmode) by the well-known method of kernel density estimation.[60,61] Practically, this is done by using equation (16) to compute the expansion coefficients, $c_l^i, i = 1, \cdots, N$ for each of the *N* DVFs in the training set. All of the coefficients associated with a given eigenvector are grouped together and each is represented by a Gaussian kernel:

$$p_l(c) \approx \frac{1}{N\sqrt{2\pi b^2}} \sum_{i=1}^{N} \exp\left(\frac{-\left(c - c_l^i\right)^2}{2b^2} \right) \quad (17)$$

where *b* is an adjustable bandwidth parameter set according to the recommendations in Silverman.[62] A typical example is shown in Figure 2. This is a well known technique for estimation of the underlying PDF when used in conjunction with PCA.[86] This technique has been previously applied in the estimation of DIR uncertainties.[59]

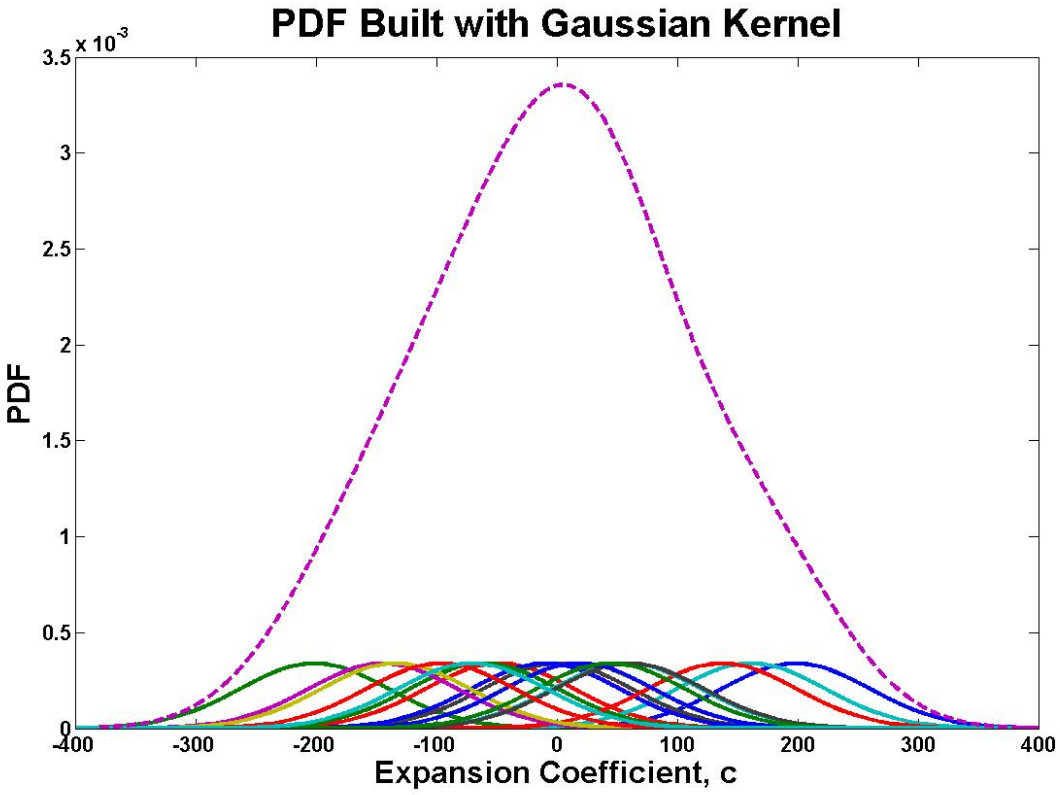

Figure 2. An example of a PDF built through kernel density estimation (KDE). The final PDF (dashed purple) is created through superposition of many Gaussian kernels taken from the training data coefficients. This PDF corresponds to the first eigenmode associated with the prostrate-centroid aligned systematic displacements.

It is simple and efficient to sample expansion coefficients to use in equation (15) for creating synthetic systematic and random tissue DVFs, which when added together, form a synthetic deformation of the anatomy. This deformation is then used to deform the reference anatomy, yielding a possible anatomical instance. This process is repeated 1000 times, and the deformed anatomies are then averaged for each voxel, giving the probability of a given organ occupying that voxel on a given treatment day. This is done for both bony and prostrate-centroid aligned setups, and the resultant occupancy maps were compared.

3. Results

3.1 Inverse consistency

The results of the inverse consistency on the systematic error are shown for each patient in Figure 3. This shows the mean inverse consistency error, $\overline{\boldsymbol{\delta}}_{i,IC}^{organ}\left(\mathbf{x}_{i,0}\right)$ of the inter-patient transformations for transporting patient specific systematic error DVFs. Table 1 gives the mean and standard deviations of the errors across all patients. In all patients, the mean error is 0.2 mm or less resulting in submillimeter discrepancies with standard deviations of 0.1 – 0.3 mm when averaged over patients. This suggests that the lower limit of meaningful DVF error modeling is about 0.2 mm with the SICLE code.

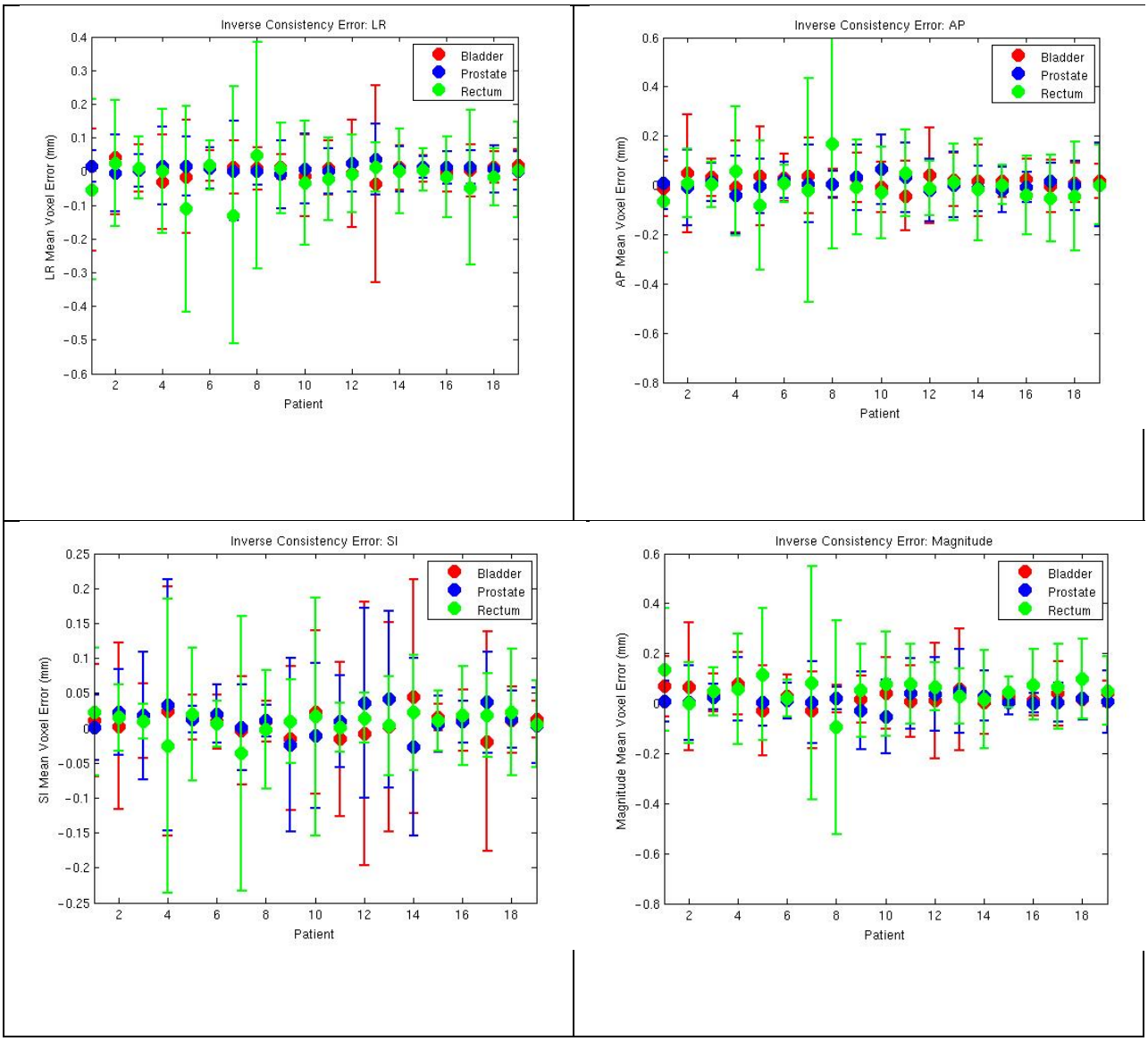

Figure 3. The inverse consistency error for the systematic error in the prostate (blue), bladder (red), and rectum (green) of each patient in the left-right (LR), anterior-posterior (AP), superior-inferior (SI) directions as well as the error magnitude. The dot represents the voxel-by-voxel mean error within the organ with the error bars representing one standard deviation.

Table 1. Mean and standard deviation of the inverse consistency results for the population modeling of both systematic and random deformations in the left-right (LR), anterior-posterior (AP), and superior-inferior (SI) directions.

		LR (mm)	AP (mm)	SI (mm)
Systematic	**Prostate**	0.01±0.08	0.00±0.12	0.01±0.09
	Bladder	0.01±0.12	0.02±0.13	0.01±0.11
	Rectum	-0.02±0.19	0.00±0.22	0.01±0.10
Random	**Prostate**	0.00±0.01	0.00±0.07	0.00±0.09
	Bladder	0.00±0.03	0.00±0.11	0.00±0.16
	Rectum	0.00±0.04	0.00±0.11	0.00±0.10

375

3.2 Spatial distribution of systematic and random dispersion parameters

The single-voxel group mean, $\mathbf{M}$, and standard deviations, $\boldsymbol{\Sigma}$ and $\boldsymbol{\sigma}$ of the population distribution of systematic and random voxel displacements as a function of error maps are shown in Figure 4 when the prostate centroids on each day-of-treatment image set is assumed
380 aligned with the simulation centroid. At the prostate centroid, the magnitudes of the group mean, systematic error, and random errors are 0.4, 1.6, and 1.5 mm respectively. One would expect these quantities to be approximately zero. However, this work aligns on the prostate centroid, and due to asymmetric deformation of the prostate, one can expect that DIR will not necessarily map the day-of-treatment centroids onto the simulation image centroid. These
385 errors increase with increasing distance from the point of alignment, with standard deviations as large as 10 mm in the bladder base and near the rectal-sigmoid colon junction due to variations in bladder and rectal filling.

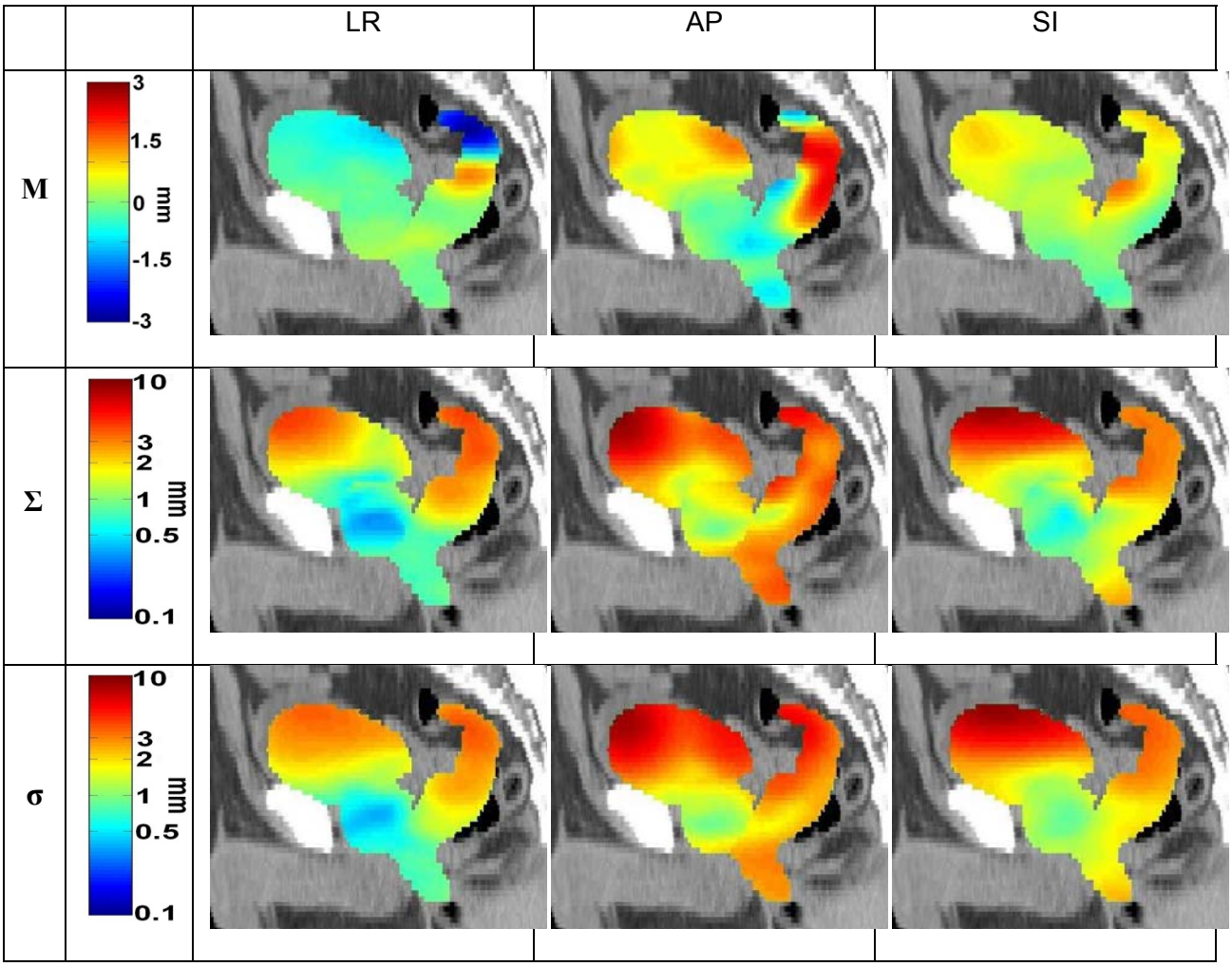

Figure 4. Sagittal views of the population mean, $\mathbf{M}$, systematic error standard deviation, $\boldsymbol{\Sigma}$, and random error standard deviation, $\boldsymbol{\sigma}$, in mm for the left-right (LR), anterior-posterior (AP), and superior-inferior (SI) directions. The values shown here are for daily patient alignment of the prostate centroid. The characterization maps are in the reference coordinate system, but overlaid on a sample patient anatomy to give a sense of location within the pelvis.

The results for the bony alignment setup are given in Figure 5. At the prostate centroid, the group mean, systematic error standard deviation, and random error standard deviation magnitudes are 1.7, 4.6, and 4.1 mm respectively. These are, as expected, larger than the corresponding values for the prostate centroid setup case. Figure 5 shows a modest trend towards reduced tissue deformation near adjacent bony structures, although some large errors are evident, e.g., AP random tissue displacement in bladder neck near the pubic symphysis, indicating that distances between bladder and rectal surfaces proximal to bones varies

400 significantly. For the prostate, the largest uncertainty is the AP location of the prostate base, which has a Σ of about 8 mm.

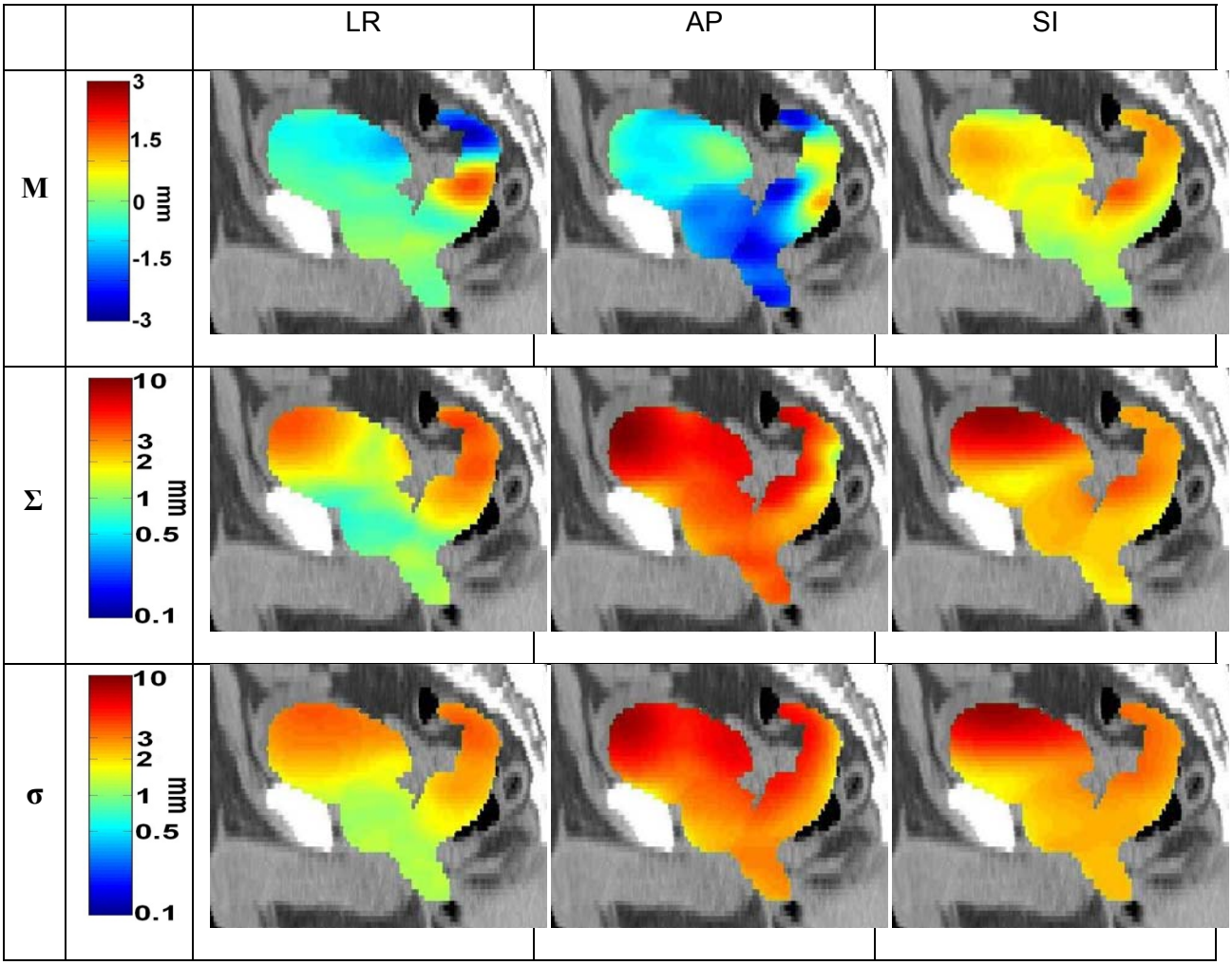

Figure 5. Sagittal views of the group mean, $\mathbf{M}$ systematic error, $\mathbf{\Sigma}$, and random error, $\boldsymbol{\sigma}$, standard deviations in mm for the left-right (LR), anterior-posterior (AP), and superior-inferior (SI) directions. The values shown here are for daily online bony alignment. These quantities are mapped in the reference coordinate system, but overlaid on a
405 sample patient anatomy to give a sense of location within the pelvis.

3.3 PCA modeling error

The PCA modeling error is shown (see Figure 6 and Table 2) for only the online prostrate-centroid alignment case. In order to account for 95% of the variance in the data, $L_{sys} = 11$ and
410 $L_{rand} = 33$ eigenmodes were needed. Over all patients, the mean and standard deviations of the PCA reconstruction error for systematic and random displacements is given in Table 2. The

mean PCA reconstruction errors were all near zero with standard deviations of approximately 0.5 mm and exceed 1 mm only for a very small number (3.8% for systematic) voxels. In general, PCA modeling errors are larger than inverse-consistency errors.

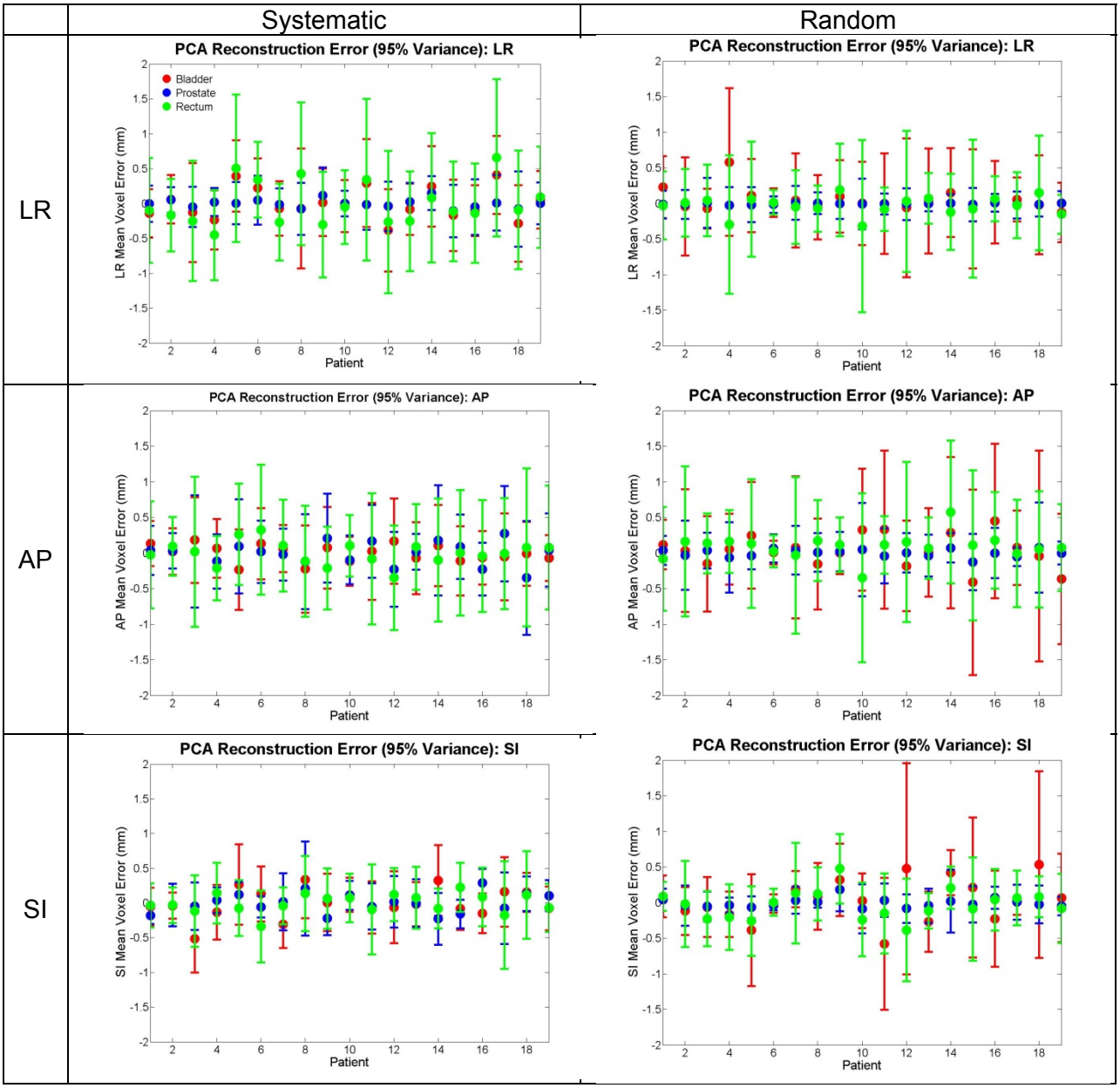

415 Figure 6: Mean difference between PCA reconstructions and original systematic component DVF along each axis. For each patient, the dots represent the mean error and the error bars show the standard deviation. The data shown here is for prostrate-centroid aligned data.

Table 2. Mean and standard deviation of the PCA reconstruction error for both the systematic and random deformations in the left-right (LR), anterior-posterior (AP), and superior-inferior (SI) directions, averaged over patients as well as voxels and daily treatment images for the case of prostrate-centroid alignment.

		LR (mm)	AP (mm)	SI (mm)
Systematic	**Prostate**	0.00±0.33	0.00±0.54	0.00±0.33
	Bladder	0.00±0.51	0.00±0.50	0.00±0.40
	Rectum	0.00±0.82	0.00±0.78	0.00±0.46
Random	**Prostate**	-0.01±0.21	0.00±0.36	-0.01±0.23
	Bladder	0.04±0.63	0.04±0.85	0.03±0.68
	Rectum	-0.03±0.65	0.09±0.79	-0.03±0.48

3.4 Leave one out study

In order to reconstruct the systematic displacements, 19 PCA models were created for the leave one out study. As with the PCA modeling error results, only the online prostrate-centroid alignment case is presented here, as results were similar for the bony alignment case. For most PCA models, either 10-11 or 32-33 principal components, respectively, were necessary to account for 95% of the variance in the systematic and random displacement input data. The average error is quite small, but with significant patient-to-patient variability. The largest mean errors (about 2 mm) are bladder and rectal systematic errors. Leave one out errors are much smaller for the random displacements than those for the systematic, implying that a larger dataset might be necessary to fully describe the systematic variability in the pelvis.

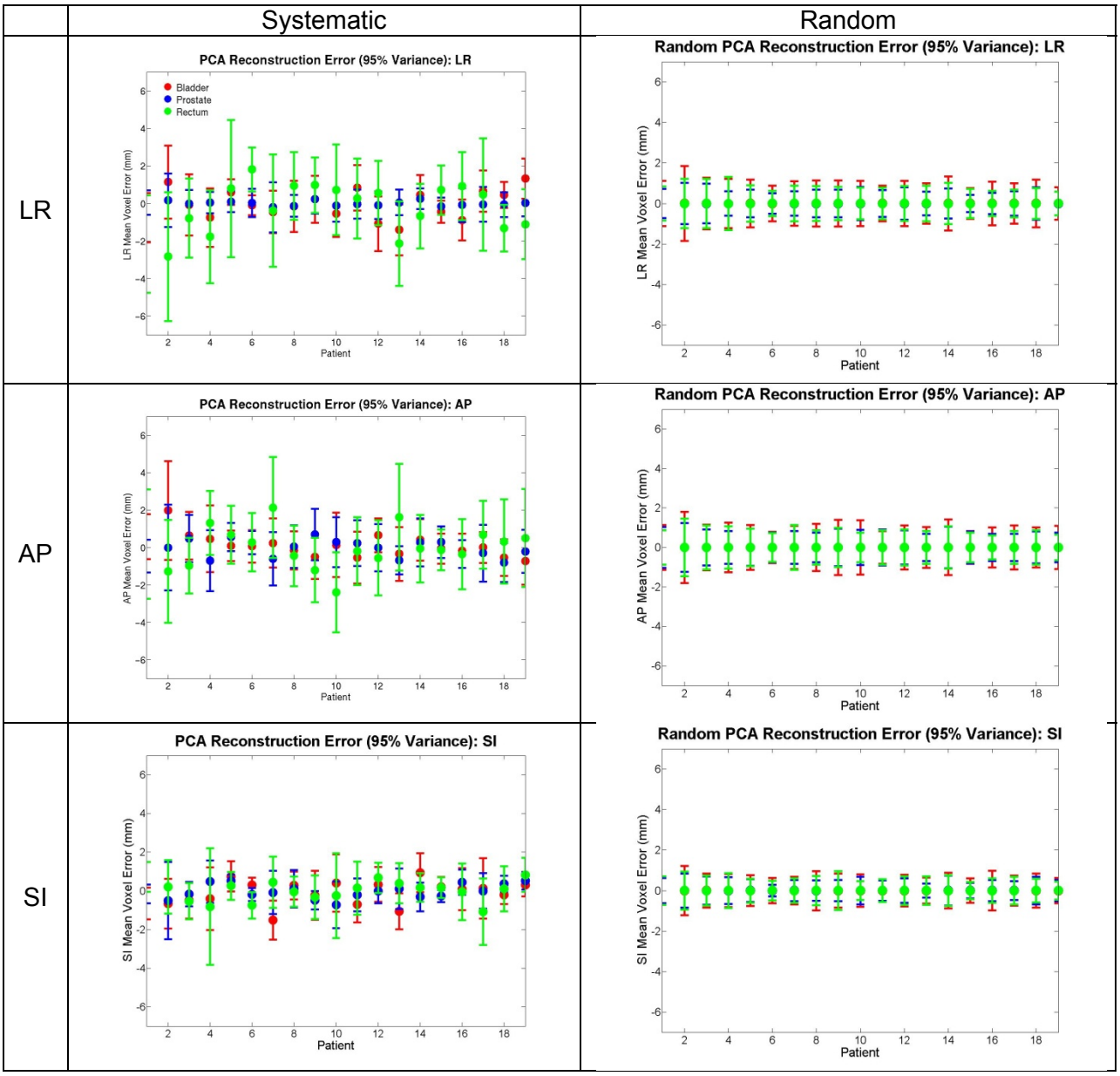

Figure 7: Results of the leave one out study for both systematic and random displacements in the case of the online prostrate-centroid alignment case, for each of the "left-out" patients. The arithmetic means and standard deviations over organ voxels between the actual DVF and that inferred from equations (16) and (15) are shown.

Table 3. Mean and standard deviations of the PCA modeling errors evaluated over the 19 "left out" patients in the leave one out study for the online prostrate-centroid alignment protocol. The mean absolute error is given below the grand mean and standard deviations.

		LR (mm)	AP (mm)	SI (mm)
Systematic	**Prostate**	0.01±0.81 0.84	-0.05±1.25 1.42	-0.03±0.87 1.00
	Bladder	-0.26±2.27 1.19	0.01±2.08 1.18	0.01±1.33 0.97
	Rectum	-0.05±1.22 2.11	0.12±1.31 1.83	-0.11±1.02 1.31
Random	**Prostate**	0.00±0.71 0.55	0.00±0.87 0.76	0.00±0.58 0.54
	Bladder	0.00±1.14 0.67	0.00±1.17 0.72	0.00±0.80 0.52
	Rectum	0.00±0.89 0.87	0.00±0.94 0.91	0.00±0.68 0.62

3.5 Organ occupancy maps

The organ occupancy maps were calculated for both the prostrate-centroid and bony aligned setup are presented in Figure 8. Using prostrate-centroid alignment, the prostate's position is known with much greater certainty. The bony alignment shows variable uncertainty in the prostate's position over 2 cm in the anterior and posterior directions, compared to 7 mm in the prostrate-centroid aligned patient. For the bladder and rectum in the prostrate-centroid aligned setup, the organ can be located with greater certainty in regions bordering the prostate, while the bony aligned setup has greater certainty in their location near bony anatomy.

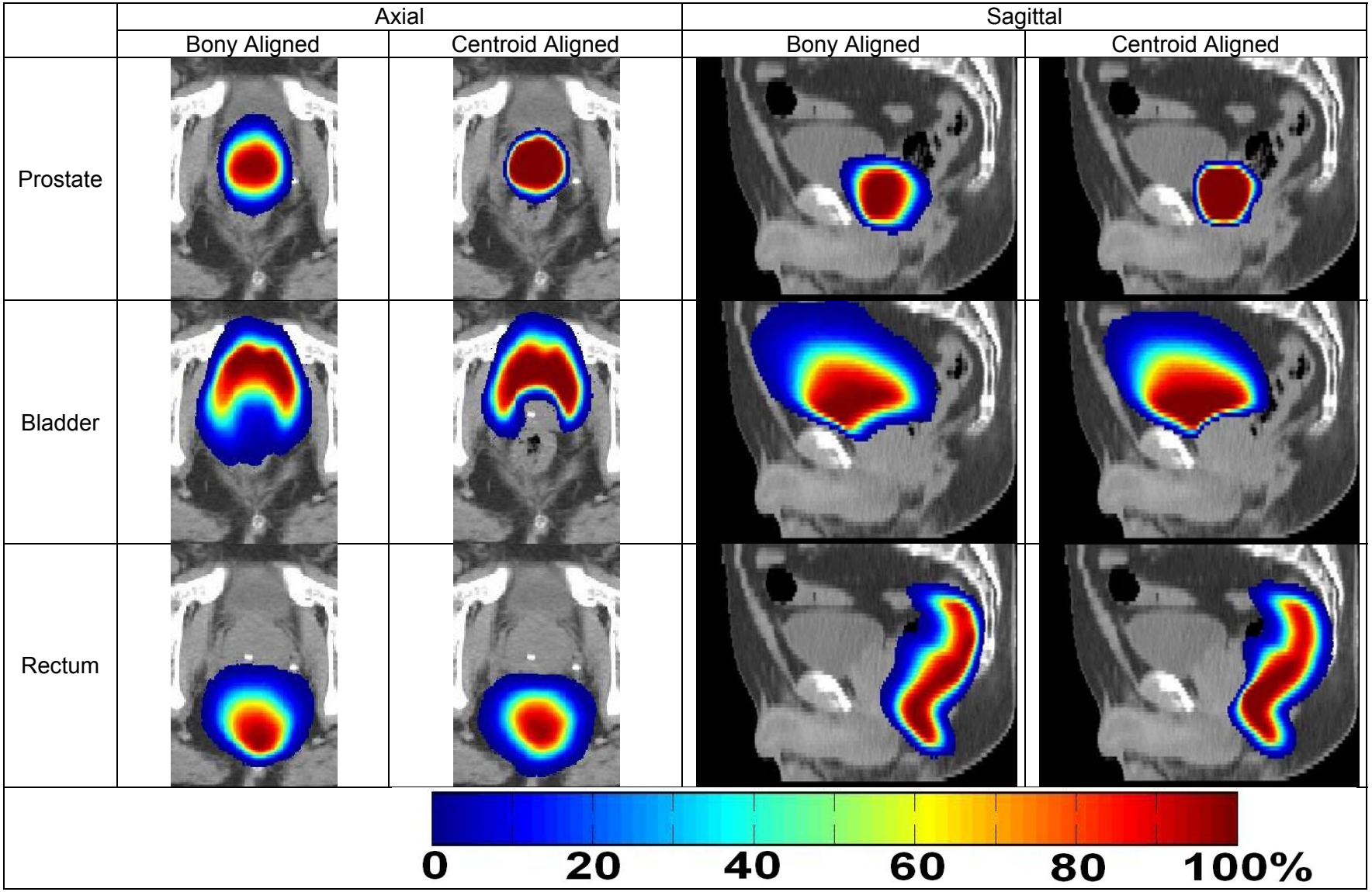

Figure 8: Organ occupancy maps for the prostate, bladder, and rectum for both bony and prostrate-centroid aligned setup. The colormap corresponds to the probability of a given voxel containing the organ on a given day. These are in the reference coordinate system and are overlaid on a sample patient for ease of viewing

4. Discussion

This paper generalizes the concept of systematic and random displacement errors to three-dimensional space by calculating them on a voxel by voxel basis. Previously, clinical practice was limited to calculating these displacements and their statistical distributions at a single point, generally the prostate centroid or an implanted marker. The assumption is that the prostate moves as a rigid body. This assumption completely ignores tissue deformation. This work shows general agreement with the literature on the values of Σ and σ at the prostate centroid, as shown in Table 4 for a bony aligned setup. However, our 3D calculation shows that these numbers are not consistent throughout the prostate, and can vary considerably near the prostate surface. These differences can potentially create a geometric miss to certain portions of the prostate during the course of treatment. This work also includes the motion patterns of the bladder and rectum.

Table 4. Comparison of this study's Σ and σ values at the prostate centroid with selected values previously reported in the literature. All values are in mm and are for a bony aligned setup. Abbreviations: LR – left/right, AP – anterior/posterior, SI – superior/inferior.

	Σ			σ		
Study	**LR**	**AP**	**SI**	**LR**	**AP**	**SI**
van Herk[87]	0.9	2.7	1.7	0.9	2.7	1.7
Beltran[81]	0.9	3.5	3.0	1.2	2.8	2.0
Current study	0.9	4.0	2.4	1.2	2.5	3.3

While this study included 210 sets of random tissue displacements, only 19 systematic tissue displacements were available for this paper. Obviously, our statistical model is limited by this input data in the types of deformations that it can represent. A leave one out study was conducted to try to quantify the ability of the PCA models to correctly describe the systematic and random organ motion of patient's not in the PCA training set. This study suggested that the systematic organ motion could be accurately described to within about 1.5 mm. This suggests that the 19 systematic error samples used in this study might be too small to fully model all

possible modes of systematic motion. The random organ motion could be modeled to a much better accuracy.

Accurate inter- and intra-patient DIRs are necessary in building the statistical model. The intra-patient registrations were done using both grayscale and contour information of the fractional images. These registrations were validated using a Dice metric. Inter-patient registrations were a much more difficult process to deal with. Using a similar process to the intra-patient registrations, some of our registrations failed to converge on a final DVF. These were due to the large anatomical differences between the patients. As the DIR algorithm used in this study cannot model DVF discontinuities due to use of Fourier series basis functions, we adopted an heuristic approach, i.e., independently registering the organs using only contour information. This approach correctly modeled individual organ shape and relative positions to one another and the bony pelvis of each patient. However, uncontoured structures, e.g., pelvic lymph nodes, vascular bundles, seminal vesicles, and pelvic bones, are not included. Nor do our registrations have the benefit of matching soft-tissue features. This makes our results dependent on the regularization (linear-elastic constitutive law) of our DIR algorithm and its ability to deform the organs in a realistic manner. For future work, a finite element based DIR would appear to be a better option, as it can produce DVFs with support limited to the organs of interest.

Inter-patient DIR is necessary in this work to transport DVFs in a patient's coordinate system to the coordinate system of the reference patient. This need to transport changes in a single patient to a reference patient or template is a current topic of study called "parallel transport".[88,89] The idea is to transport vectors along geodesics while retaining vector parallelism. In the future, these methods could produce a better method for pooling the statistics in this study.

While not directly demonstrated in this work, our statistical model has several possible clinical applications for improving treatment. PTP is perhaps the most important such

application. Conceptually, our PCA model is used to randomly select an ensemble of systematic and randomly deformed instances of a patient's anatomy, enabling the optimizer to select the MLC leaf sequence that maximizes the fraction of deformed instances of anatomy meeting the treatment goals and constraints.[56] In order to do this, some knowledge of the distribution of displacements must be known *a priori*. Our statistical model gives detailed information about this population distribution over all voxels within the three organs of interest.

A more straightforward application of this work is construction of a patient PTV that represents a more optimal tradeoff between target coverage and normal tissue dose. Currently, isotropic or pseudo-isotropic margins are used to create the PTV, many times based off of margin formulas. Also, the van Herk formula cannot be directly applied to the prostrate-centroid alignment protocol, as the Σ and σ parameters would be zero. PCA population modeling can create anisotropic margins for any patient setup that would provide more coverage in areas of larger deformation and less coverage in areas of minimal deformation. Synthetic systematic and random displacements could be sampled from our model, transferred to the patient's planning image coordinate system, and used to deform their planning contours. An organ occupancy diagram can be created for the prostate similar to those presented in this work. This diagram could be thresholded (covering, for example, 95% of all anatomical variations), and this volume could be used as the PTV.

5. Conclusion

The purpose of this work was to create a statistical population model of systematic and random tissue motion. Patient-specific systematic and random displacements were transported to a reference coordinate system. In this reference coordinate system, the traditional measures of systematic and random error distributions, Σ and σ, were calculated for the prostate, bladder, and rectum on a voxel by voxel basis for bony and prostrate-centroid aligned patient

setups. A PCA technique was implemented to determine the principal modes of systematic and random deformation.

ACKNOWLEDGEMENTS

The authors wish to thank the NKI for providing the images used in this work and Elisabeth Weiss for her work in their contouring. We also wish to thank Jeffrey Siebers for reprocessing all of the CTs used in this study. This work was supported by NIH grant P01CA116602.

Vita

Douglas Jacob Vile was born on July 17, 1986, in Somers Point, New Jersey and is an American citizen. He graduated from Lower Cape May Regional High School, Cape May, New Jersey in 2004. He received his Bachelor of Science in Physics from Salisbury University, Salisbury, Maryland, in 2008.